

國立臺灣大學理學院天文物理研究所

碩士論文

Graduate Institute of Astrophysics

College of Science

National Taiwan University

Master Thesis

原恆星系統 L1551 IRS5 及 L1551 NE 之分子雙極噴流

Bipolar Molecular Outflows in
L1551 IRS5 and L1551 NE Protostellar Systems

吳柏鋒

Wu Po-Feng

指導教授：林仁良 博士

高桑繁久 博士

賀曾樸 博士

Advisor: Jeremy Lim, Ph.D.

Shigehisa Takakuwa, Ph.D.

Paul T. P. Ho, Ph.D.

中華民國 98 年 7 月

July, 2009

致謝

這篇碩士論文主要在中研院的林仁良博士(Dr. Jeremy Lim)與高桑繁久博士(Dr. Takakuwa Shigehisa)指導下完成。

首先要感謝 Jermey，你是一個好老師。這兩年我沒有花太多的時間迷航，是你帶領我往正確的大方向前進，並教導我如何用宏觀的角度思考科學問題。謝謝 Shige，我用掉了你很多時間。多少個下午，我們在你的辦公室討論各種問題，從你那我得到了許多實用的意見。謝謝中研院天文所賀曾樸主任，從我的論文出發，你提醒了我什麼才是探索這個宇宙的正確態度。而這份研究的背後還有一個強大的顧問團支持—所有中研院天文所的研究員們。對於任何層次的科學問題或技術上的麻煩，你們總是能提供有用的支援。

謝謝 820 的住戶們，有你們在的辦公室總是充滿笑聲，踏進辦公室成為一件開心的事。因為如此，我才能持續工作一天，一天，又一天。也謝謝所有中研院天文所的研究助理和學生，我喜歡每一次與你們的互動。無論是科學上的討論，日常閒聊，亦或是關起門來偷偷說三道四，每一件小事都令人開心。而我的大學同學們，你們也是不可或缺的一部分。每次見面的笑靨都是最有用的補給品。知道大家都過得很好，各自在人生的道路上努力，讓我能開心地接下一次又一次的全新挑戰。

最後，最重要的是我的家人。即使你們完全搞不清楚我究竟在做什麼研究，也不同意我的選擇，你們仍然放手讓我走自己的路，並且無條件地給予我一切所需的援助。如果我有任何小小的成就，那不屬於我，一切都屬於你們。

Acknowledgment

This thesis work is finished under the supervision of Dr. Jeremy Lim and Dr. Takakuwa Shigehisa. I would like to thank Jeremy, who helps me with developing my ability to do research, teaches me how to think as a scientist and leads me go through the process from playing with the data to publishing a paper. Thanks to Shige for taking care of my detail problems. I spent a lot of your time, sitting in your office and asking any kinds of questions and receiving practical opinions from you. I also would like to thank Dr. Pual Ho, who gives me crucial comments on my work and reminds me of the right attitude for doing science. This work is also supported by a strong consultant group – all IAA researchers. You always kindly provide your helps at all levels, give me your precious opinions on science questions and technical problems.

Thanks to the residents of room 820. You fill this office with happiness. Because of you, stepping into this office and working whole day becomes a pleasure. Also for all IAA students and RAs, I really delight in our interactions, including academic or non-academic, sharing our science, chatting or gossiping. For my undergraduate classmates in physics department, even you are not directly related to the thesis work, I still want you to know that you are also an important part of it. Your laughter always energizes me for taking the coming challenges.

A special thank is for my family. Even you have no ideal on what I am doing and disagree the road I choose, you still allow me go my way and unconditionally provide your supports. All my achievements belong to you.

摘要

L1551 分子雲為一低質量恆星形成區域，且為距太陽系最近的恆星形成區域之一。觀測上顯示，此區域中存在許多不同演化階段的原恆星系統，意味著長時間以來，此區域皆為一活躍的恆星形成區域。我們使用次毫米微波陣列(Submillimeter Array, SMA)觀測 L1551 分子雲中兩個原恆星系統—L1551 IRS5 及 L1551 NE—周圍區域的一氧化碳分子譜線，以探測該原恆星分子雙極噴流的物理性質。

L1551 IRS5 是 L1551 分子雲中輻射熱光度最強的多重原恆星系統，且擁有巨大的分子雙極噴流。其大尺度分子雙極噴流呈東北(紅移端)—西南(藍移端)方向，各自向外延伸約 1.5 秒差距。我們藉由角分辨率約 4 角秒(約 560 天文單位)的 CO(2—1)分子譜線影像探測此噴流之中心約 4000 天文單位的區域。在此中心區域，我們分辨出三個不同噴流結構：(1) X 形結構，自中心向外延伸約 20 角秒，其方位角與大尺度噴流相近，且有相同之紅藍移方向。此 X 形結構為中央高速噴流所開之錐狀空腔之臨邊增亮現象。(2) S 形結構，自中心向外延伸約 10 角秒，其方位角與大尺度噴流相近，但紅藍移方向相反。此 S 形結構為新發現的分子雙極噴流。S 形結構以及視線方向速度的變化顯示此噴流正在進動。此噴流可能是被此系統中一新發現的原恆星所驅使，且其環星盤與鄰近的原恆星有強烈潮汐作用而使環星盤進動。(3) 中央緊密結構，自中心向外延伸約 1.4 角秒，其方位角與大尺度噴流相近，且有相同之紅藍移方向。此結構為原恆星系統中心近期受中央高速噴流所驅使的分子氣體。

L1551 NE 是 L1551 分子雲中輻射熱光度次強的多重原恆星系統，位於 L1551 IRS5 東北方 2.5 角分處，為 L1551 IRS5 的巨大分子雙極噴流影響。L1551 NE 所驅使的分子雙極噴流尚未被確認。我們利用角分辨率約 0.8 角秒(約 110 天文單位)的 CO(3—2)分子譜線影像探測此系統周圍較溫暖之氣體，首次成功拍攝下此系統分子雙極噴流的電波波段影像。此分子雙極噴流自中心延伸僅約 8 角秒，且其動力學年齡極短，顯示此為一年輕的原恆星系統，但其質量明顯小於其他位於同樣演化階段的分子雙極噴流。此現象指出，L1551 NE 鄰近區域的氣體分子已被 L1551 IRS5 的強烈噴流掃除。另外，我們的一氧化碳分子譜線影像與紅外光觀測中之扇形反射星雲吻合，但卻未發現在紅外光波段同樣出現的束狀噴流。此現象暗示 L1551 NE 系統中的兩原恆星處在不同演化階段，驅使扇形反射星雲的原恆星較早演化或演化較快，其噴流將鄰近區域之分子氣體掃除。較晚演化的原恆星之束狀噴流驅使之分子噴流密度因此較低而無法觀測。

Abstract

L1551 molecular cloud is located at a distance of ~ 140 pc, in the constellation of Taurus, and is one of the nearest active low-mass star formation region. We used the Submillimeter Array (SMA) to image the CO molecular outflows from two multiple protostellar systems in L1551 region, L1551 IRS5 and L1551 NE, at an arcsecond angular resolution. We observed the CO(2–1) line emission in L1551 IRS5 system. First, we imaged the base of the outflow cavity and found signatures for multiple outflow events. We also found newly entrained gas in the cavity, indicating that the ambient gas is still falling into the cavity. Second, we discovered a precessing outflow, which has an opposite inclination to it of L1551 IRS5 large-scale outflow. This newly-found component is likely driven by the recently proposed candidate third protostar in L1551 IRS5 system. For the L1551 NE binary system, we shows a clear bipolar structure of its molecular outflow at the first time. We saw a cavity-like structure corresponding to the reflection nebula at infrared wavelength, but no jet-like structure, which is also seen at infrared. It is likely that, one of the binary launched the outflow first and cleaned ambient gas away, thus the outflow from another protostar entrained less gas and is unable to be detected. The mass of L1551 NE outflow and the dusty envelope are both by orders of magnitude smaller than those of other Class 0 protostars, suggesting the ambient gas has been swept up by the strong outflow from L1551 IRS5.

Contents

List of Figures	ii
List of Tables	v
1 Star Formation	1
1.1 Star Formation Environment	1
1.2 Star Formation Processes	2
1.3 Classification of Protostars	4
1.4 Molecular Outflows in Protostellar Systems	5
1.4.1 Outflow Launching Mechanisms	6
1.4.2 Models for Molecular outflows	7
1.4.3 Physical Properties of CO Outflow	13
2 INTRODUCTION TO L1551 STAR-FORMING REGION	18
2.1 L1551 Dark Cloud	18
2.2 L1551 IRS5 Protostellar System	19
2.3 L1551 NE Protostellar system	24
3 Observation of L1551 IRS5 Protostellar System	32
3.1 Abstract	32
3.2 Multiple Bipolar Molecular Outflow from the L1551 IRS5 Protostellar System	34

3.3	Mechanism of Jet Bending	35
4	Bipolar Molecular Outflow from the L1551 NE Protostellar System	38
4.1	Introduction	38
4.2	Observations and Data Reduction	39
4.3	0.8 mm Continuum Emission	42
4.4	CO(3-2) Line emission	47
4.5	Discussion	54
4.5.1	Impact from IRS5 outflow	54
4.5.2	Different Age of the Binary Protostars	55
5	Future Work	58
5.1	L1551 IRS5	58
5.2	L1551 NE	61
	Bibliography	64
A	Missing Flux Resulted form the Visibility Coverage	70

List of Figures

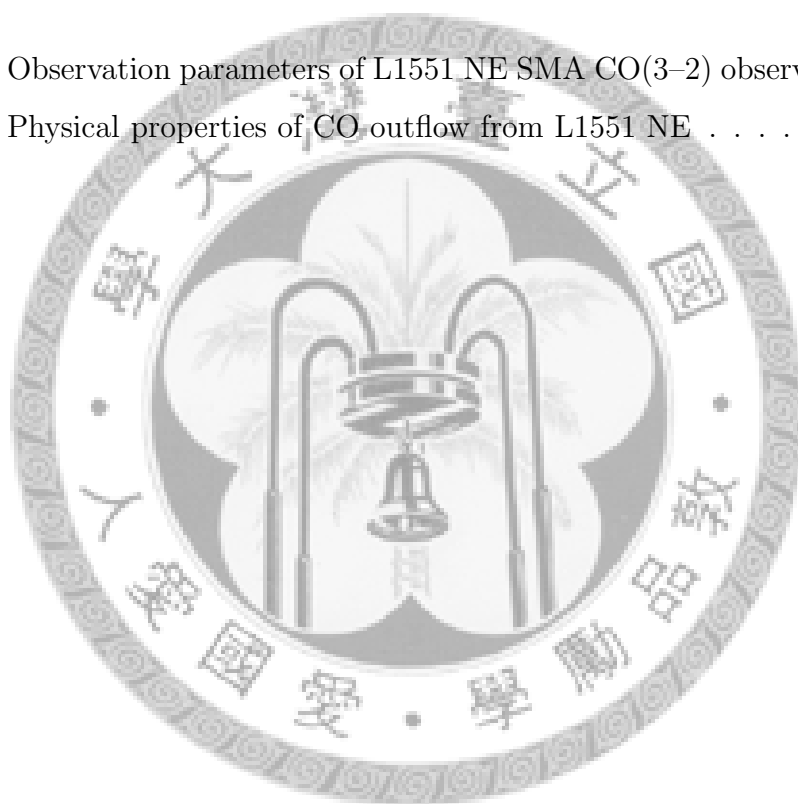
1.1	Star-formation processes for single low-mass stars	3
1.2	Spectral energy distributions (SED) of protostars in different classes	5
1.3	Wind-driven model	8
1.4	Position-Velocity diagram of VLA 05487 outflow	9
1.5	Bow-shock model	11
1.6	Molecular outflow of HH 211	12
1.7	Evolution of outflow opening-angles	15
1.8	Precessing outflow from Cep E	16
2.1	L1551 star-forming region	20
2.2	Spectral energy distribution of L1551 IRS5	21
2.3	CO outflow of L1551 IRS5	22
2.4	Gas envelope, circumbinary disk and circumstellar disks of L1551 IRS5	24
2.5	Duplicity of L1551 IRS5	25
2.6	Near infrared image of L1551 NE system	27
2.7	Multiplicity of L1551 NE	28
2.8	JCMT image of CO gas surrounding L1551 NE	30
2.9	Single-dish and interferometry CS images of L1551 NE system	31

3.1	Bent jet model	37
4.1	0.8 mm continuum image of L1551 NE	43
4.2	Model fitting of L1551 NE 0.8 mm image, one disk plus one Gaussian	45
4.3	Model fitting of L1551 NE 0.8 mm image, one disk plus two Gaussians	46
4.4	CO(3–2) channel maps of L1551 NE	48
4.4	Continue	49
4.5	CO(3–2) integrated intensity map of L1551 NE	50
4.6	CO(3–2) spectra of L1551 NE from JCMT and SMA	52
4.7	Mass of dusty envelopes of Class 0 and Class I protostars	56



List of Tables

4.1	Observation parameters of L1551 NE SMA CO(3-2) observation	41
4.2	Physical properties of CO outflow from L1551 NE	53



Chapter 1

Star Formation

Stars are the building rocks of the visible sky. The process by which stars form is thus one of the basic questions of Astronomy. Stars are self-gravitating gaseous balls whose central temperatures are high enough for nucleus fusion reactions. Their masses can be as high as several tens of, maybe over 100 solar masses, or only a few tenths of solar mass, just at the margin that hydrogen fusion can occur.

1.1 Star Formation Environment

Molecular clouds are the principle sites of star formation. Typically clouds have sizes of several tens of parsecs, and contain masses of 10^5 to $3 \times 10^6 M_{\odot}$. These giant clouds have complex substructures named “clumps”. Clumps have relatively higher densities of $n_{H_2} \sim 10^{2.5} \text{ cm}^{-3}$, sizes of a few parsecs, and contain $10^3 \sim 10^4 M_{\odot}$. Subregions in clumps, called —cores—, have even higher densities of $n_{H_2} > 10^4 \text{ cm}^{-3}$. These sites are believed to be the birthplaces of stars, because they are tightly associated with known T Tauri stars and infrared sources (Beichman et al., 1986).

1.2 Star Formation Processes

Star formation processes have proposed a generally accepted framework for low-mass stars from Shu et al. (1987). During the early stages, a dense core in the molecular cloud contracts slowly instead of collapsing violently (see Figure 1.1*a*).

The magnetic force resists the self-gravity of the core. Here the electrons and ions are species which sense the magnetic field and couple with magnetic field lines, while neutrals sense gravity and drift across magnetic field lines. The neutrals move relative to charged particles and the frictional drag force prevents the neutrals directly fall into the center, slows down the contraction speed. At some point, as the core gradually loses its magnetic support, the central concentration will cause a gravitational collapse. The gas in the molecular cloud with sufficiently large specific angular momentum first lands on the equatorial plane, forms a disk, then transfer to the central star. This is the main accretion phase of a protostar.

During the accretion, material is also ejected out from the star-disk system. It is now generally agreed that the outflowing material is launched centrifugally along magnetic field lines, although the precise mechanism is still under debate. Material is ejected out in the direction of the rotational axis, leads to bipolar outflows (see Figure 1.1*c*).

As time proceeds, the outflow opens a wider angle and sweeps up the outside envelope, ceases the mass accretion. The system in this stage remains a central star and a disk but not the envelope (see Figure 1.1*d*). This is observed as a T Tauri star. Finally, the disk becomes the material reservoir for planet formation or disperses into space. The system goes into a pre-main-sequence stage.

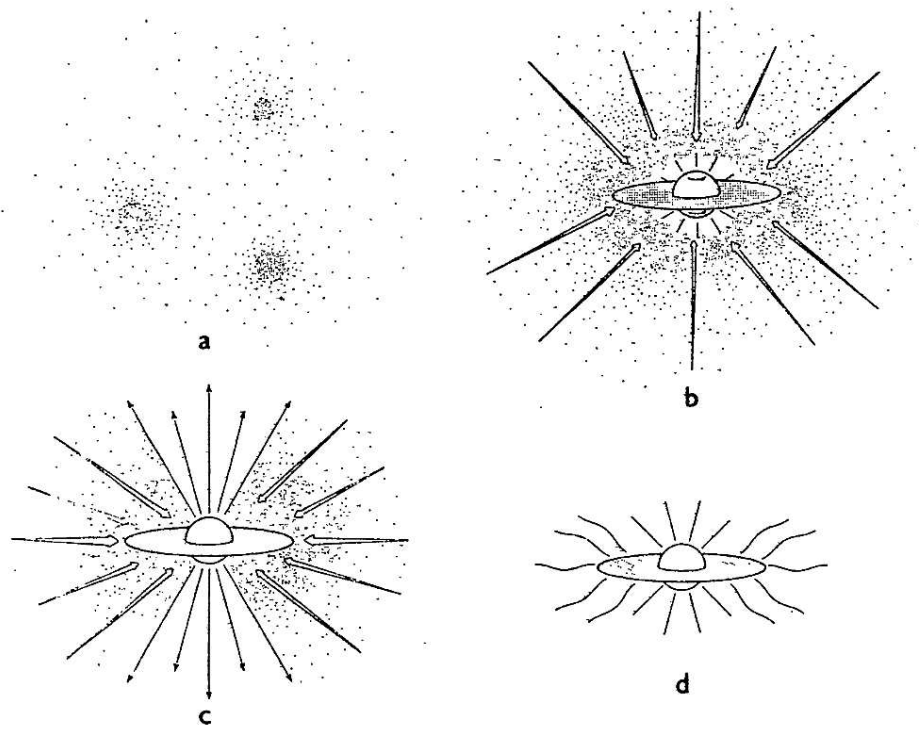


Figure 1.1: Four stages of star formation for single low-mass stars. (a) Magnetic supported cores within molecular clouds slowly contract. (b) A protostar with a surrounding disk collapses rapidly. This is the main accretion phase. (c) An outflow emerges, creates bipolar outflow, sweeps up ambient materials. (d) Accretion stops. The system remains a newly formed star with a circumstellar disk. (Shu et al., 1987).

1.3 Classification of Protostars

Young stellar objects are observed to exhibit excess radiation at infrared wavelengths, that is, more flux than blackbody spectrum. This infrared excess radiation is due to circumstellar material, which absorbs stellar photons and reemits at infrared wavelengths. The spectral index α_{IR} of the radiation is defined as

$$\alpha_{IR} \equiv \frac{d \log(\lambda F_\lambda)}{d \log \lambda} \quad (1.1)$$

It is conventional to evaluate the α_{IR} by differencing the flux between $2.2\mu\text{m}$ and $10\mu\text{m}$. By varying the properties of stars and those of the circumstellar material, theoretical models can successfully reproduce the infrared excess in many observed sources (Adams et al., 1987). Therefore, the spectral index reflects the basic properties of the protostellar system and is used to categorize protostars into different classes, which are associated with different evolutionary stages.

The typical spectral energy distribution at different evolution stages are shown in Figure 1.2. Class I sources are characterized by $\alpha_{IR} > 0$. They have only remnant infalling envelopes, and have accumulated a large fraction of their final stellar mass (André & Montmerle, 1994; André, 1995). Class II protostars, or classical T Tauri stars, have infrared spectral index $-1.5 < \alpha_{IR} < 0$. They are at a more evolved stage, contain circumstellar disks, but no infalling envelopes. Those whose spectral index $\alpha < -1.5$ are Class III protostars, or weak-lined T Tauri stars, which have very weak or no disks. Later a new class, Class 0, is proposed. Class 0 sources are the youngest protostars, still highly self-embedded in surrounding molecular clouds, and in their main accretion phase. Observationally, Class 0 protostars do not have emission at wavelength longer than $10\mu\text{m}$, but high submillimeter luminosity

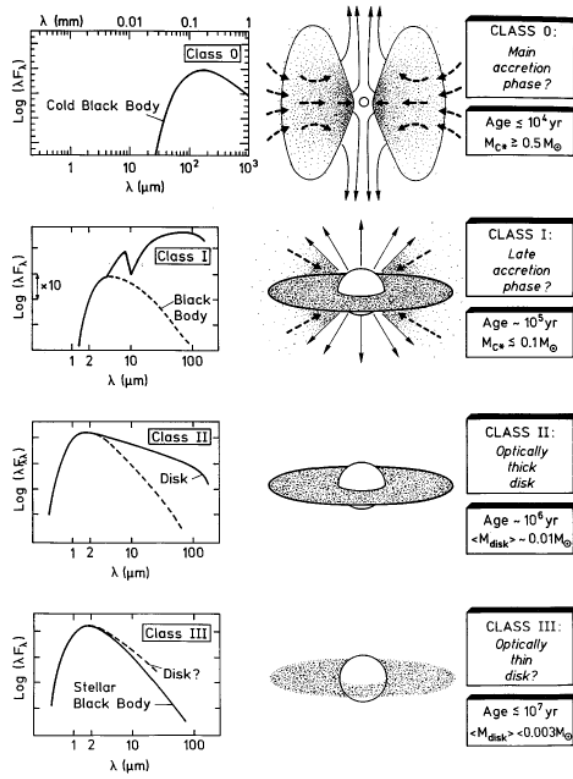


Figure 1.2: Spectral energy distribution (SED) and schematic figures for young stellar objects in different classes. Different SEDs are resulted from the structures of systems.

(André et al., 1993).

1.4 Molecular Outflows in Protostellar Systems

Bipolar outflows is a common and essential ingredient in the star formation processes. The outflowing material is observable over a wide range of wavelengths. The first signature of outflow activities are Herbig–Haro

(HH) objects, which are small knots with optical line emission. HH objects were later recognized as hot, ionized gas, heated up by the collision between high speed outflowing material and ambient material (Schwartz, 1975). Subsequent proper motion measurement and detection of collimated wind confirmed that the wind emanates from the vicinity of young stellar objects (Cudworth & Herbig, 1979; Mundt & Fried, 1983). Signatures at other wavelengths including centimeter free-free continuum of ionized gas, infrared continuum of warm gas and emission lines. When the collimated outflow interacts with ambient molecular cloud, it sets the gas into motion, gives rise to the molecular outflow.

1.4.1 Outflow Launching Mechanisms

Outflow is regarded as one of the key processes during the early evolutionary stage which carries away excess angular momentum of the inner region of the system thus allowing accretion. However, the detail launching mechanisms are still poorly understood. So far, two most promising models are X-wind model and disk-wind model.

The X-wind model suggests that material is accelerated outwards from the zone where the stellar magnetosphere co-rotates with the disk. This region lies typically a few stellar radii from the sources, and is called the X-point (Shu et al., 1988, 1994). The disk-wind model proposed that winds are launched from the rotating, magnetized disks. It was first suggested as the origin of jets from accretion disks around black holes and soon proposed as the mechanism for protostellar jets (Pudritz & Norman, 1983, 1986).

1.4.2 Models for Molecular outflows

Molecular outflow is believed to be entrained by the ejected matter to velocities higher than those of the cloud. Several models are proposed to explain how the ambient is entrained. Two most successful models in explaining observed molecular characteristics are: (1) wide-angle magnetized winds, (2) jet-driven bow shocks.

Wide-angle Magnetized winds

The first hypothesis asserts that the bipolar molecular outflows are swept up by the wide-angle magnetized wind, as illustrated in Figure 1.3. The ambient gas is set into motion by acquiring momentum from the wind. If the wind has an axial density gradient, the wind can appear as a collimated jet (Shu et al., 1991, 1995). The wide-angle wind model can produce a molecular outflow with wide-opening angle and performs well in explaining the kinematics in several outflow systems (Lee et al., 2000). For example, Figure 1.4 shows the comparison between observation and model calculation of the kinematics and spatial structure of the protostellar system VLA 05487. Both the PV cut along the jet axis and the total integrated intensity map in gray scale show the V-shaped structure. Contours from model calculations can reproduce the overall structure.

Jet Driven Bow Shocks

The other proposed mechanism of molecular outflows is that they are the shocked gas when high-velocity jets propagate into the ambient gas. When a supersonic jet emanates toward the surrounding envelope, large amount of gas is trapped in the working surface, then flows sideways. This gas interacts with external unperturbed medium, forms the bow-shock surface,

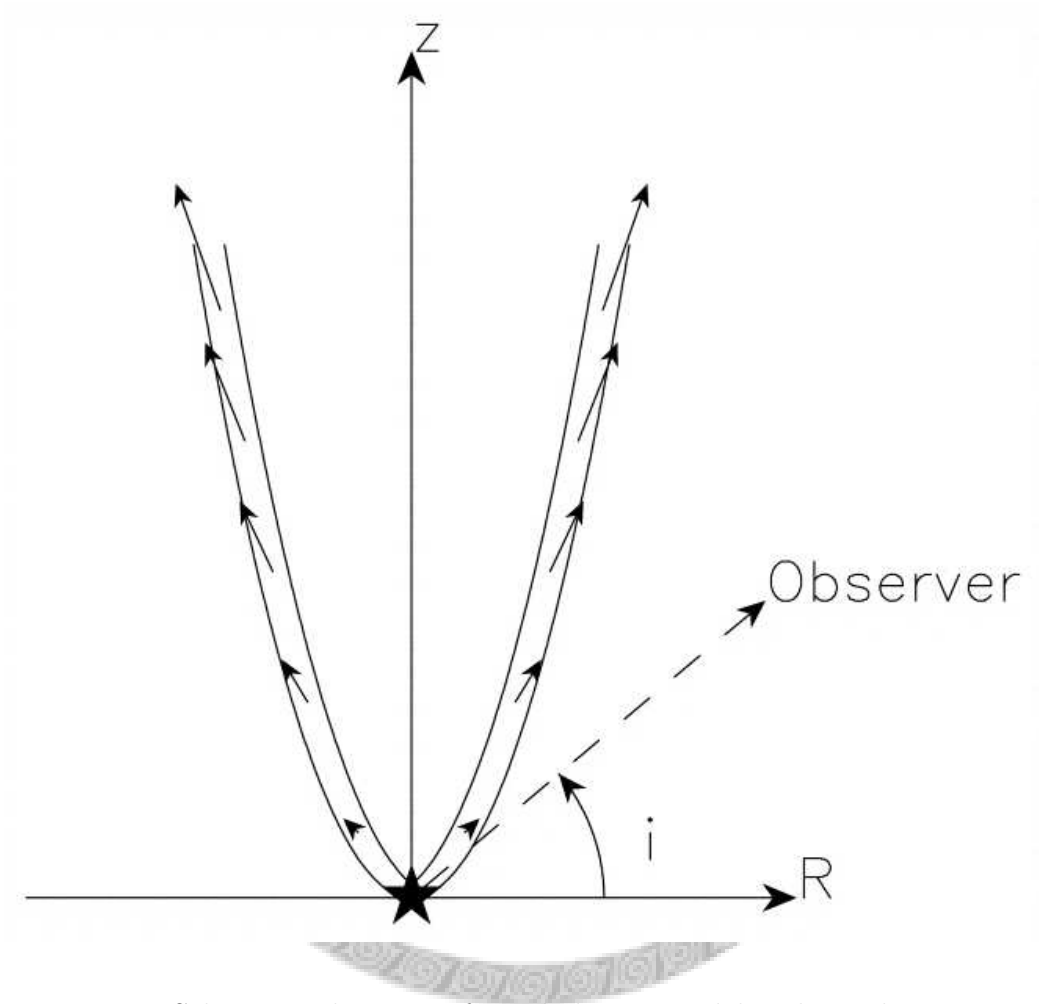


Figure 1.3: Schematic diagram of wind-driven model. The inclination i is the angle between observer. In the scenario, the magnetized wind transfer its momentum to ambient gas, which is observed as bipolar molecular outflows.

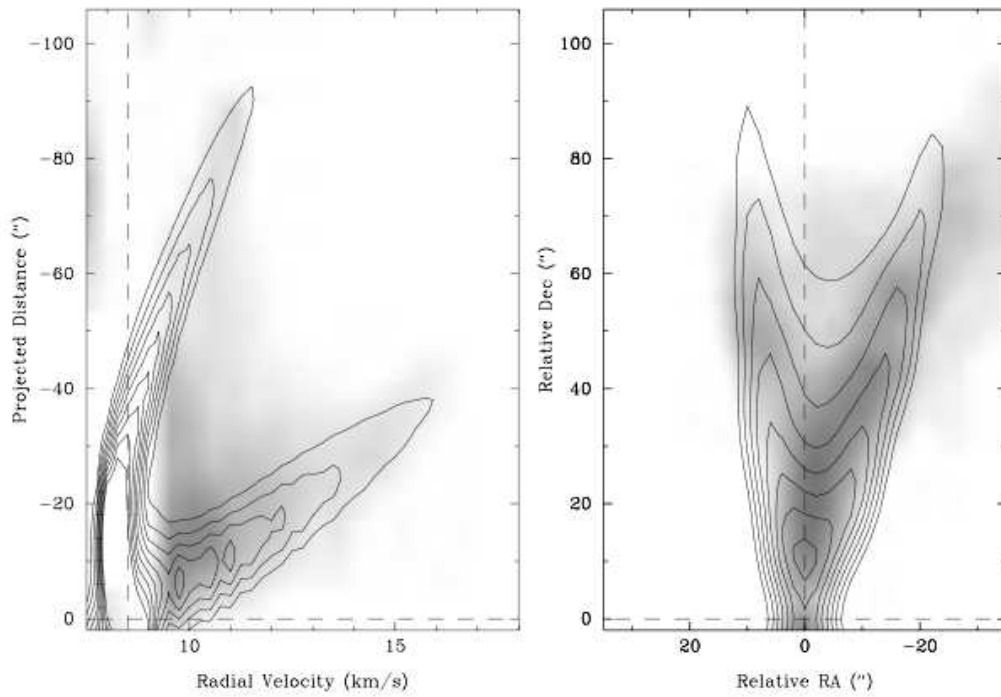
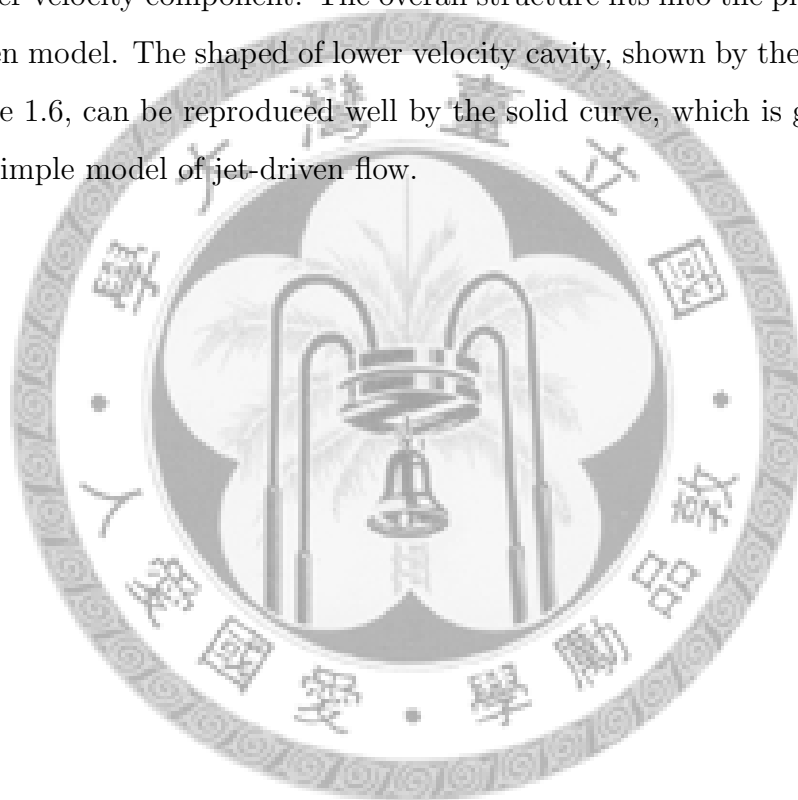


Figure 1.4: Comparison between wind-driven model and observation for VLA 05487. The gray-scale images are the observations and the contours are from the calculations for wind-driven model. The left panel shows the PV diagram cut along the jet axis. The right panel shows the integrated intensity map (Lee et al., 2000).

flow backwards in the reference frame of the jet, as illustrated in Figure 1.5. The bow-shocked layer reexpands after the working surface passes by, which appears as the molecular outflow we see (Raga & Cabrit, 1993). The bow-shock model is appealing because it explains several observed properties of some molecular outflows. For example, the CO outflow of a Class 0 protostar, HH 211, exhibits a collimated, higher velocity component and a wider cavity-like, lower velocity component. The overall structure fits into the picture of a jet-driven model. The shaped of lower velocity cavity, shown by the contours in Figure 1.6, can be reproduced well by the solid curve, which is generated from a simple model of jet-driven flow.



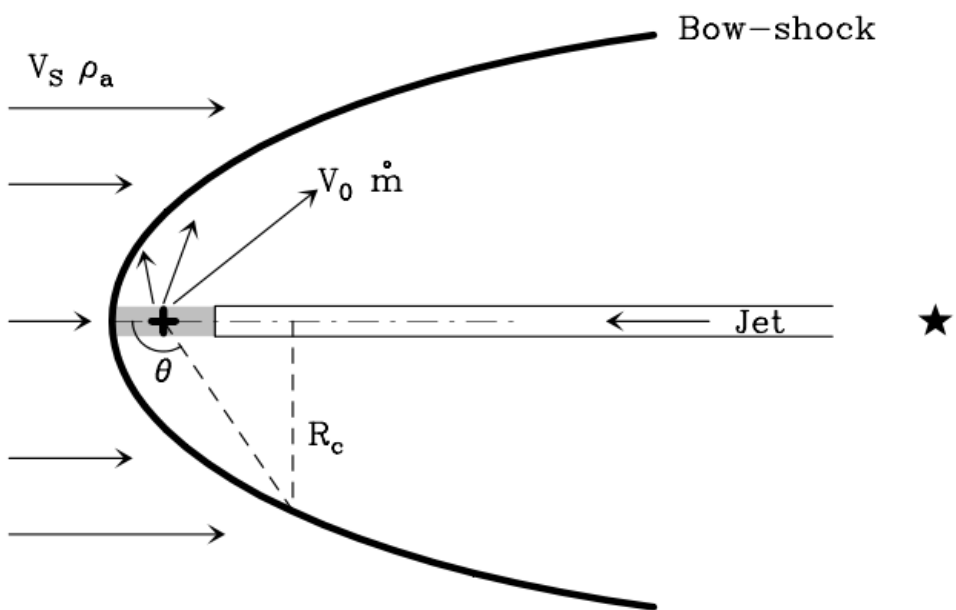


Figure 1.5: Sketch of the structure of the bow-shock. The velocities are in the reference frame of shock. A dense, collimated jet is ejected into the ambient medium, creates a bow-shock (Gueth & Guilloteau, 1999).

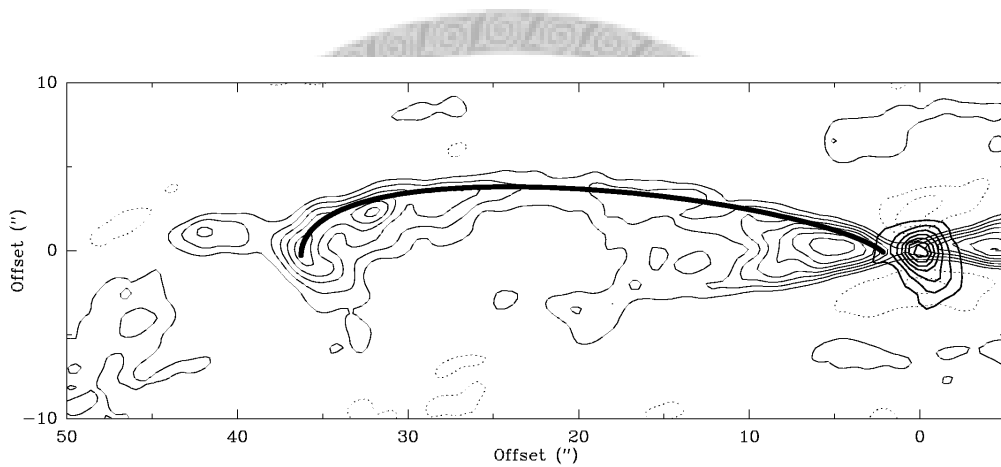


Figure 1.6: Comparison between bow-shock model and observation of HH 211. The contours are 230 GHz continuum emission (centered at (0,0)) and low velocity CO(2-1) emission. Thick line is the model calculation of the cavity (Gueth & Guilloteau, 1999).

1.4.3 Physical Properties of CO Outflow

CO is the second abundant molecule among interstellar gas species, only next to molecular hydrogen. It has simple line structure, thus simple rotational energy levels, that can be easily observed in millimeter and sub-millimeter wavelengths. Outflow properties can be obtained by converting observed CO lines into physical gas parameters. Measuring the line ratio between two rotational lines is often used to derive the gas kinetic temperature. As for the optical depth, measurements of lines from different isotopes can give a good estimate. Having both excitation temperature and optical depth, it is possible to derive the CO gas column density by using equations of radiative transfer. The mass of outflowing gas can be calculated by assuming a CO abundance. Moreover, the momentum and energy of outflowing gas can also be estimated from obtaining the mass distribution and line-of-sight velocity.

Molecular outflows driven by low-mass protostars ($< 1M_{\odot}$) have been extensively studied and show some basic common features. The most characteristic property of outflows is their bipolarity. Two separated lobes of gas, one redshifted and the other blueshifted, lie next to each other, with a young stellar object in between. The length of outflows is typically 0.1 to a few pc, with a wide range of collimation. The collimation factor is defined by major radius divided by minor radius. Typical values obtained from single-dish observations are 3–20, while interferometric maps tend to give higher numbers, that is more collimated, due to its better angular resolution. The mass of molecular outflows also ranges over a few orders of magnitudes, from $\sim 10^{-2} M_{\odot}$ to as high as $> 10 M_{\odot}$. The momentum supply rate is about 10^{-5} – $10^{-4} M_{\odot} \text{ km s}^{-1} \text{ yr}^{-1}$ (Bontemps et al., 1996; Arce et al., 2005a).

Outflow Opening Angle

The outflow opening angle is often considered as a signature of the age of the driving source. Arce & Sargent (2006) showed a clear trend that the outflow opening angle becomes larger as the central star evolves, based on their survey of molecular outflow within $\lesssim 10^4$ AU of nine protostellar systems in different evolutionary stages, together with previous observations. Figure 1.7 plots the outflow opening angles versus source ages. Data are from Arce & Sargent (2006) and literatures therein (see Table 9 of Arce & Sargent, 2006, for the reference list). Data points populate in the upper-right and lower-left parts of the diagram, mean that older protostars posses outflows with larger opening angle. Class 0 protostars exhibit relatively collimated jet-like outflow or cone-shaped lobes with opening angles $< 55^\circ$, where as Class I protostars have outflow lobes with wider opening angles of $> 75^\circ$ (with $\sim 125^\circ$ the largest opening angle seen).

Outflow Precession

Observations with higher angular resolution revealed bending or winding structures or misalignment between two lobes of the outflow, for example, Cep E in Figure 1.8 (Eisloffel et al., 1996), and L1557 (Gueth et al., 1996). The bending structure indicates the ejection direction changes over time. However, the reason for the changing ejection direction has not been well established yet.

Multiple Outflow

Several outflow systems have quadropolar morphology, that is, four lobes are observed and seem to be driven by the same condensation. The quadropolar outflows are an indication for the multiplicity of the central protostellar sys-

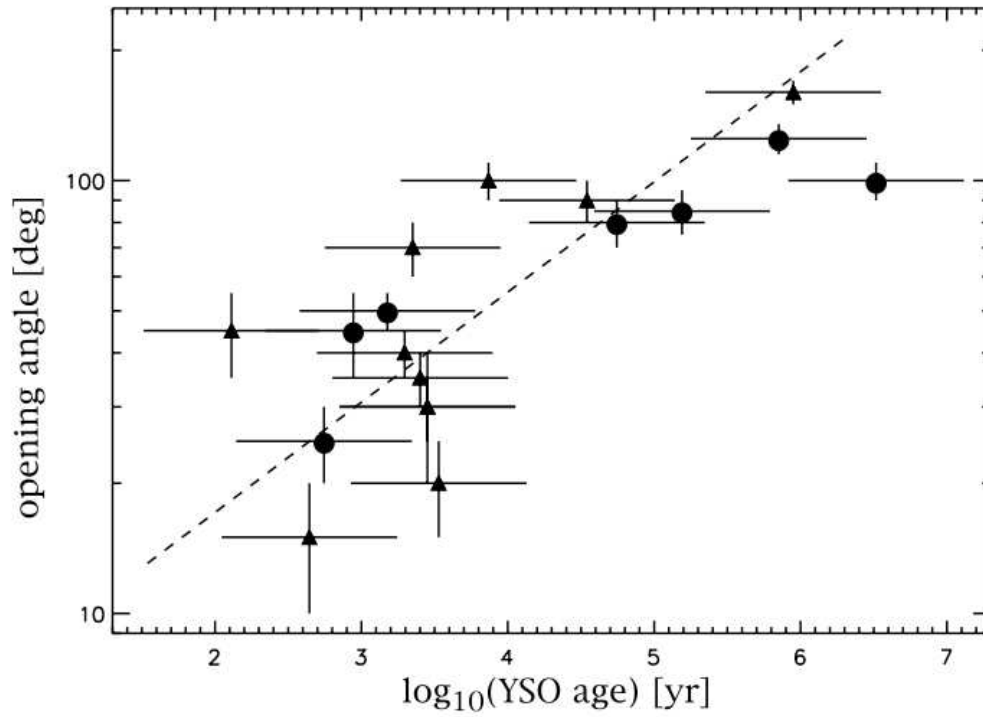


Figure 1.7: Outflow opening angle versus source age (Arce & Sargent, 2006). The ages are estimated from bolometric temperatures. Circles are from observations in Arce & Sargent (2006), triangles are from literatures therein. In average, the outflow opening angles of older sources are larger than those of younger sources.

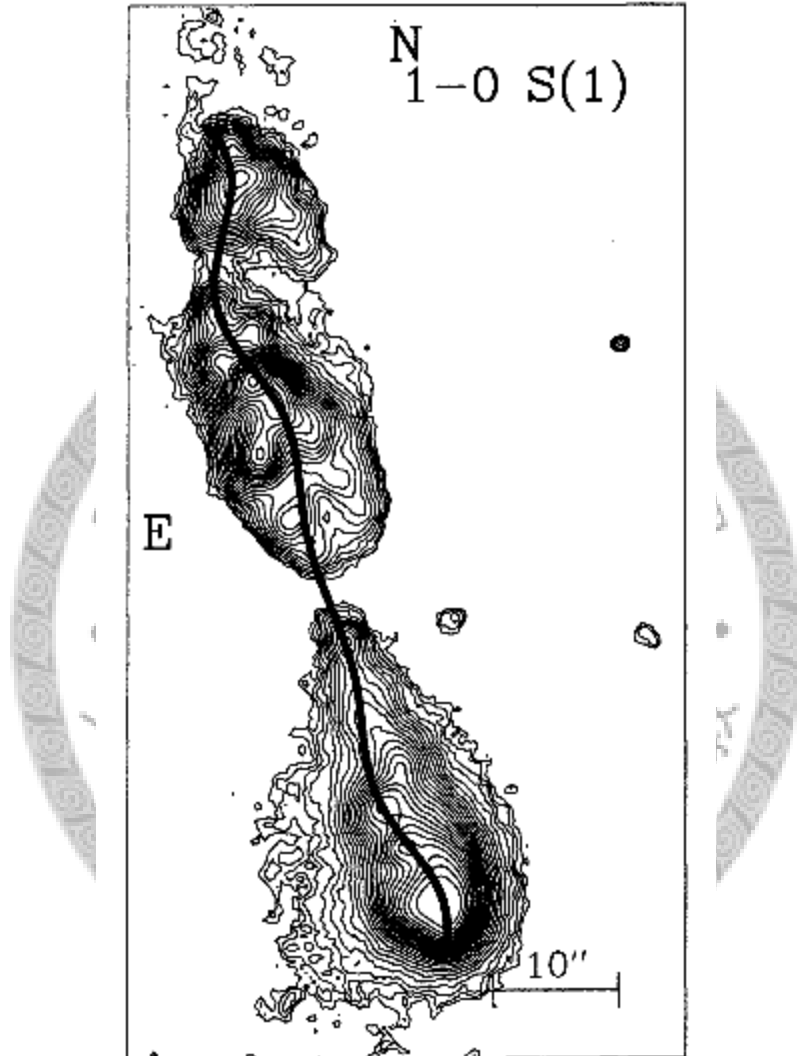


Figure 1.8: Precession model (black curve) superposed on molecular hydrogen $1-0\ S(1)$ line emission of Cep E. (Eisloffel et al., 1996). In this case, the outflow precesses at 4° .

tem, without directly resolving the driving sources (see Gueth et al., 2001; Lee et al., 2002, for examples).



Chapter 2

INTRODUCTION TO L1551 STAR-FORMING REGION

2.1 L1551 Dark Cloud

The L1551 dark cloud (Lynds, 1962) is one of the nearest and therefore best studied regions of low-mass star formation. It lies in the constellation Taurus at a distance has been measured to be 140 ± 10 pc (Kenyon et al., 1994), and has diameter of $\sim 20'$ (~ 1 pc). Surveys at different wavelengths have found numerous signatures of star-formation: infrared sources (Storm et al., 1976; Gálfalk et al., 2004), Herbig-Haro (HH) objects (Garnavich et al., 1992; Devine et al., 1999), young T Tauri stars (Briceño et al., 1998), infrared reflection nebula (Hayashi & Pyo, 2008, Figure 2.1), and bipolar molecular outflows (Pound & Bally, 1991; Moriarty-Schieven & Wannier, 1991). Observations in different CO lines have revealed the overall morphology and kinematics of outflows in the L1551 region on parsec scales and nearly all outflows have been identified with their driving sources. Several star-formation sites have been identified, such as L1551 IRS5, L1551 NE, HH 30, HL Tau,

XZ Tau that concentrate in the densest parts of the cloud, and more than 30 classical and weak T Tauri stars are distributed in the cloud (Gålfalk et al., 2004). Both younger (Class 0 and Class I) objects, such as L1551 NE and L1551 IRS5, and more evolved classical and weak-line T Tauri stars (Class II and Class III) are present, indicating that star formation activities has lasted at least for a few million years (Moriarty-Schieven et al., 2006).

2.2 L1551 IRS5 Protostellar System

L1551 IRS5 was first detected as an infrared survey in the L1551 cloud (Storm et al., 1976), it exhibits a luminosity of $\sim 32L_{\odot}$, obtained by summing up luminosities measured from $1.2 \mu\text{m}$ to $160 \mu\text{m}$ (Cohen et al., 1984), and is the brightest source in L1551 star-forming region.

Although L1551 IRS5 is prominent at infrared wavelength, it is invisible in optical. Modeling of its infrared spectral energy distribution (SED), shown in Figure 2.2 suggests it belongs to Class I evolutionary stage (Adams et al., 1987).

L1551 IRS5 is the first protostar from which a molecular bipolar outflow, detected in $^{12}\text{CO}(2-1)$, was first recognized (Snell et al., 1980). A more recent $^{12}\text{CO}(1-0)$ image is shown in Figure 2.3, taken by Stojimirović et al. (2006) with James Clerk Maxwell Telescope (JCMT). Its outflow extends ~ 1.5 pc towards the NE (redshifted lobe) and SW (blueshifted lobe) directions at a position angle of $\sim 50^{\circ}$. Each outflow lobe has a U-shaped structure, together with knotty components having distinct velocities, suggestive of multiple ejection events (interpretation of Bachillar et al., 1994).

Apart from the large-scale bipolar molecular outflow, L1551 IRS5 is surrounded by a compact molecular condensation. This condensation is elon-

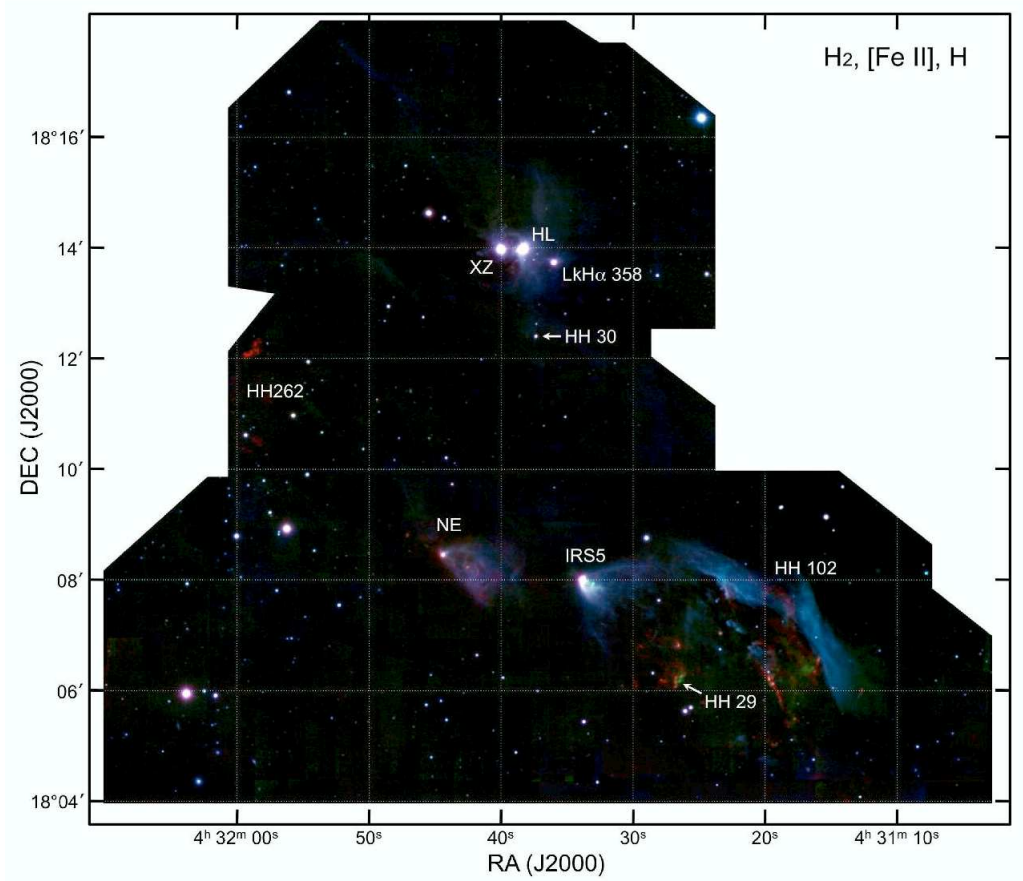


Figure 2.1: Composite color image of L1551 star-forming region taken by Subaru. The blue, green and red colors are assigned to the broad-band filter H , narrow-band filter $[\text{Fe II}] \lambda 1.644 \mu\text{m}$ and narrow-band filter H_2 , respectively. (Hayashi & Pyo, 2008)

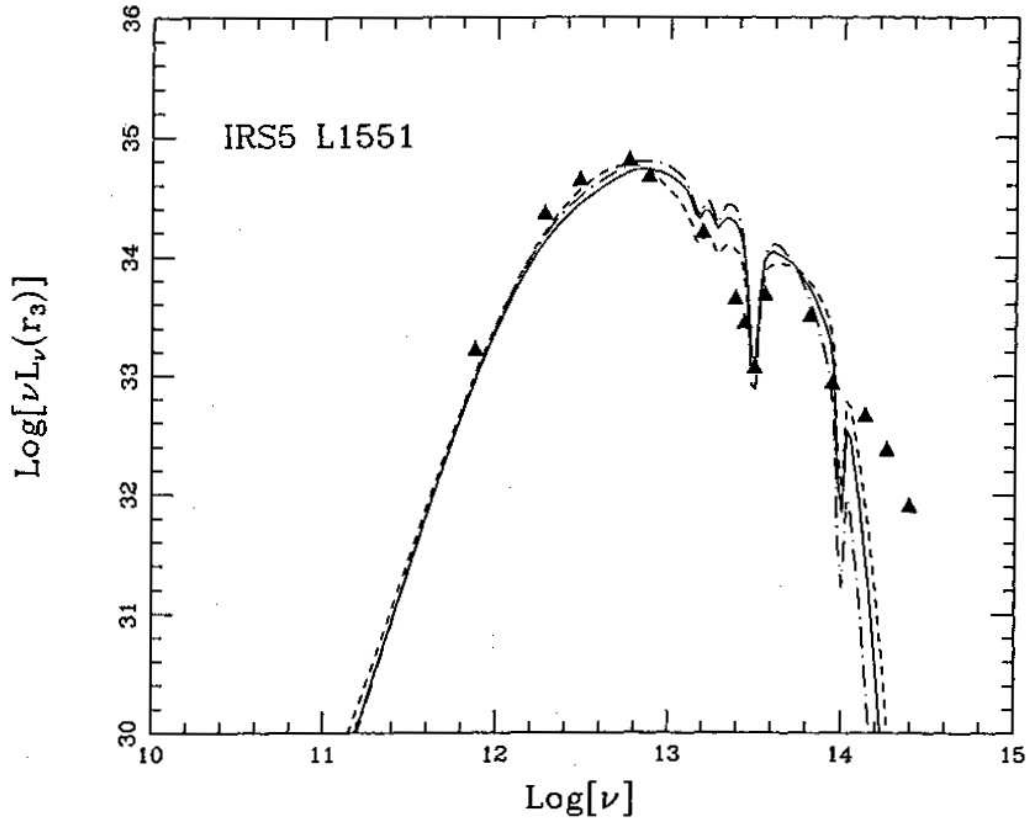


Figure 2.2: Spectral energy distribution (SED) of L1551 IRS5, Figure 1g in Adams et al. (1987). This plot shows $\log(\nu L_\nu)$ vs. $\log(\nu)$ in cgs units. Solid and dashed curves are theoretical models used in Adams et al. (1987).

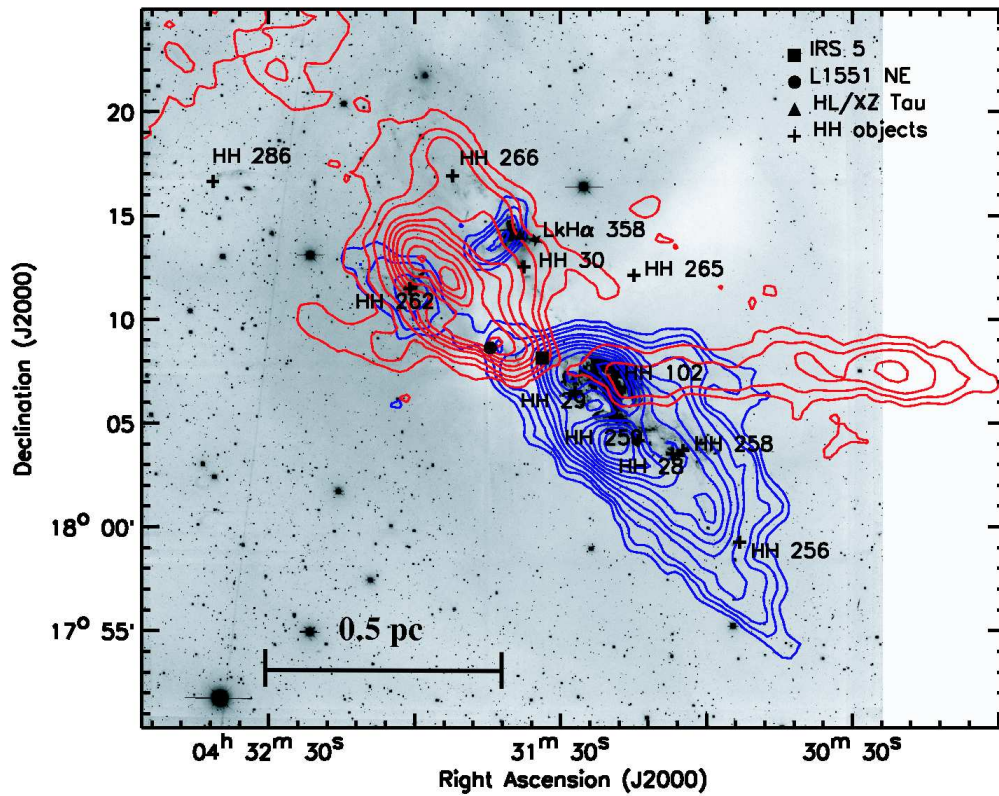


Figure 2.3: CO(1-0) integrated intensity map overlaid on H α data, (Stojimirović et al., 2006). The outflow associated with L1551 IRS5 is in NE(red)–SW(blue) direction. Another redshifted red lobe extends to the west, which its driving source is still unclear.

gated in the NW–SE direction, perpendicular to the major axis of the large-scale bipolar molecular outflow. Figure 2.4a shows the C¹⁸O image of the condensation taken by Momose et al. (1998). It has a linear size of ~ 2400 AU in the direction of major axis. The kinematics of the condensation indicates it is a flattened envelope which is contracting and rotating (Ohashi et al., 1996; Saito et al., 1996; Momose et al., 1998). In the inner, warmer region of the envelope, traced by high rotational transition lines of CS, rotation dominates over infalling motion (Takakuwa et al., 2004, see Figure 2.4b).

The first indication of its duplicity came from Bieging & Cohen (1985), who discovered two sources in L1551 IRS5, separated by $\sim 0.3''$ (~ 42 AU) at 2 cm in north-south direction (Figure 2.5a). Looney et al. (1997) showed observations in the 2.7 mm continuum that L1551 IRS5 contains two circumstellar dust disks surrounded by a possible circumbinary dust disk and/or extended envelope. Rodríguez et al. (1998) spatially resolved the two circumstellar dust disks for the first time at 7 mm. These two protostellar components were shown to have the same proper motion through space except for a much smaller component of motion attributed to their orbital motion about each other (Rodríguez et al., 2003a), and each drives a protostellar jet (Rodríguez et al., 2003b). Lim & Takakuwa (2006) spatially resolved the two circumstellar disk along both major and minor axes, and showed that these disks are aligned with each other as well their surrounding rotating and flattened pseudodisk. The major axis of each disk is perpendicular to the ionize jet. They also showed that the two disks orbit each other in the same direction as the rotation of the pseudodisk. This feature may indicated the two disks form through a fragmentation of parent rotating cloud. Finally, a candidate third protostellar component is detected, located near the northern protostellar component (Figure 2.4c). The circumstellar disk of this third

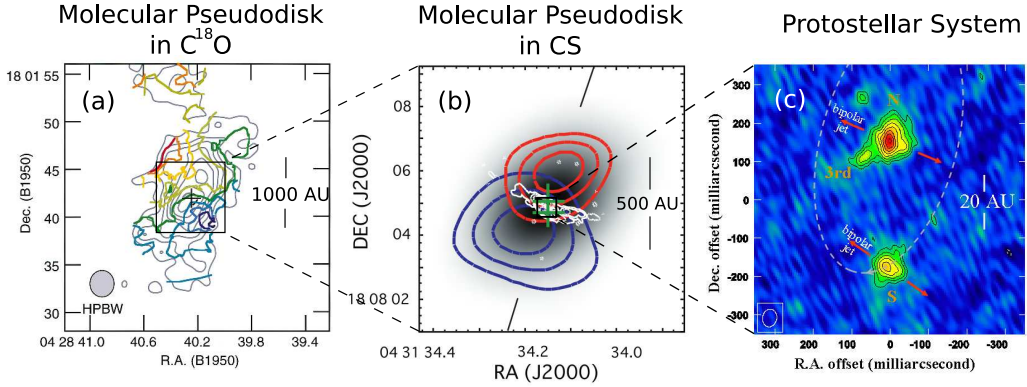


Figure 2.4: (a) Intensity-weighted mean velocity map of L1551 IRS5 obtained from the $C^{18}O$ emission, adapted from Momose et al. (1998). The $C^{18}O$ emission is elongated in the direction perpendicular to the outflow axis, indicating it comprises a flattened circumstellar envelope around L1551 IRS5. The velocity pattern suggests both infall and rotation appears in the central part. (b) CS(7–6) emission (blue and red contours) superposed on the 343 GHz continuum emission (gray scale) and VLA 3.5 cm radio jet image (white contours). The CS(7–6) line traces the warmer and denser gas in the inner part of the envelope. The NW-SE velocity gradient is perpendicular to the jet axis, suggests rotation dominates in the inner envelope. (c) 7 mm image of L1551 IRS5, adapted from Lim & Takakuwa (2006). The two main protostars orbit with each other clockwise, same direction as that of the inner gas envelope. These features may indicate that the two main protostars forms from a disk fragmentation process. In addition, a smaller third condensation is resolve in this map.

component is misaligned relative to the circumstellar disks of the two main components as well as their surrounding pseudodisk.

2.3 L1551 NE Protostellar system

L1551 NE was discovered by Emerson et al. (1984) from *IRAS* data, and it is the second brightest embedded source in L1551 cloud ($L_{bol} \sim 6L_{\odot}$) and sits only $\sim 2.5'$ northeast to L1551 IRS5 (Figure 2.1). It is classified as a

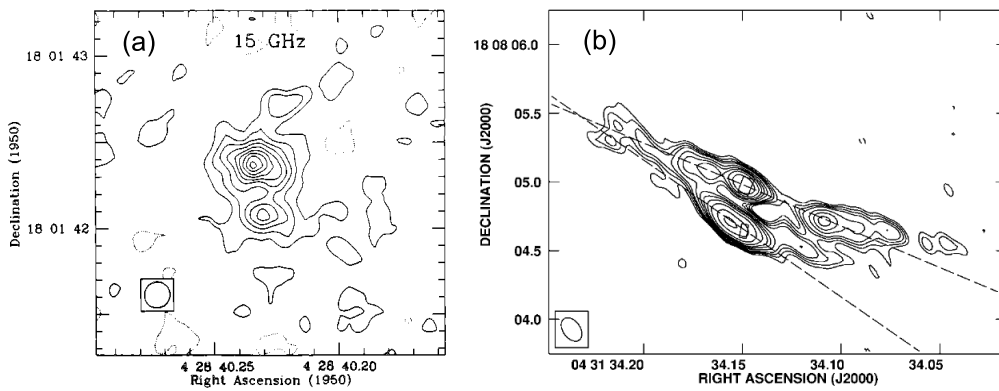


Figure 2.5: (a) L1551 IRS5 2 cm continuum image. The two sources are located in north-south direction, with a separation of 42 AU (Bieging & Cohen, 1985). (b) The binary jet of L1551 IRS5 imaged at 3.5 cm. Each jet is approximately centered on the 7 mm protoplanetary disks. This confirmed that L1551 IRS5 is a binary system where each star is surrounded by a disk and powers a collimated jet (Rodríguez et al., 2003b).

Class 0 source, mainly because of its shallower density distribution of its circumstellar envelope, which is also observed in other Class 0 protostars (Barsony & Chandler, 1993).

Optical and infrared observation suggests that L1551 NE drives a high-speed protostellar jet. A recent infrared image is shown in Figure 2.6. HH objects and a collimated [Fe II] jet have been attributed to L1551 NE (Hodapp & Ladd, 1995; Devine et al., 1999; Reipurth et al., 2000; Hayashi & Pyo, 2008). A reflection nebula, whose apex is at the position of L1551 NE, is also seen in optical and infrared (Draper et al., 1985; Reipurth et al., 2000; Hayashi & Pyo, 2008). Closely examining of the infrared emission indicates that, the collimated [Fe II] jet does not pass through the brightest point of the reflection nebular. The brightest point of the reflection nebular offsets $0''.2$ northwest from the jet axis.

The binarity of L1551 NE is first shown by Rodríguez et al. (1995), who discovered two sources at 3.5 cm , separate by $0.5''$ in east-west direction. Later observation with better angular resolution and high signal-to-noise ratio at the same wavelength confirmed that it is indeed a binary (Reipurth et al., 2002), as shown in Figure 2.7a. At this wavelength, the eastern component NE A is 1.4 times brighter than the western component NE B. The NW-SE orientation of the binary system gives a good explanation to the offset of the jet axis and the brightest point of the reflection nebular. The eastern source drives the [Fe II] jet, while the western source is associated with the reflection nebular. Finally, as shown in Figure 2.7b, Moriarty-Schieven et al. (2000) detected a continuum source at 1.3 mm located at $1.4''$ southeast to the binary and interpreted it as the third protostar of L1551 NE system. But this peak was undetected in 3.5 cm .

The molecular outflow, one of the common features of protostellar sys-

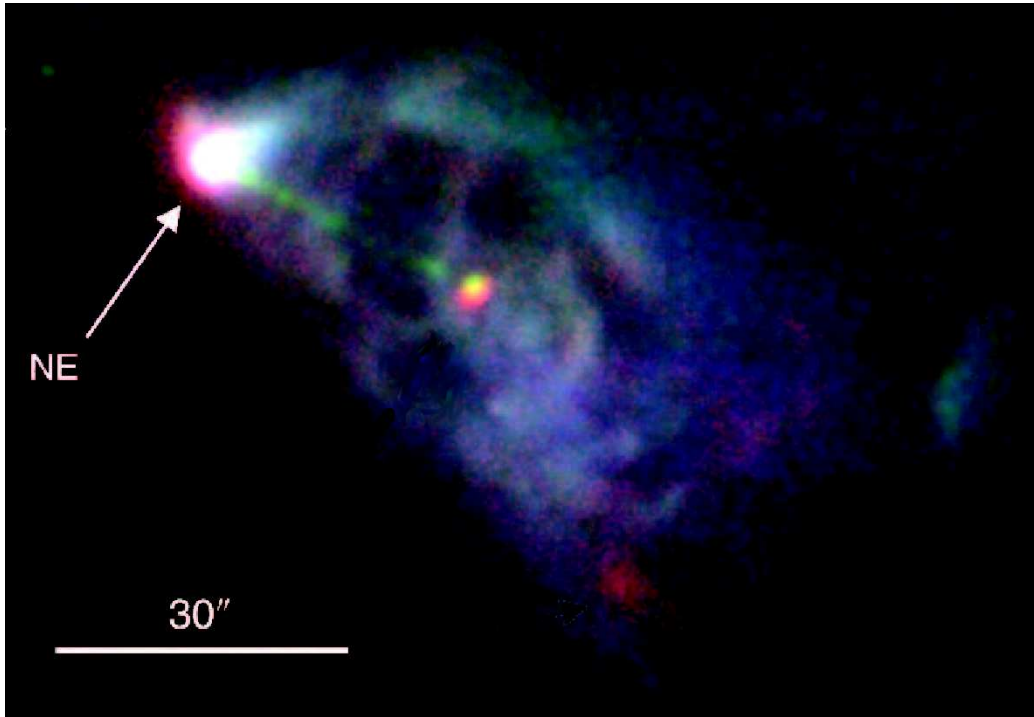


Figure 2.6: Composite color image of L1551 NE, adapted from Hayashi & Pyo (2008). The blue, green and red colors are assigned to the broad-band filter H , narrow-band filter $[\text{Fe II}] \lambda 1.644 \mu\text{m}$ and narrow-band filter H_2 , respectively. The reflection nebula extends southwestward, with its brightest point at L1551 NE. A collimated $[\text{Fe II}]$ jet with $\sim 30'$ length and a position angle of 244° is emanated.

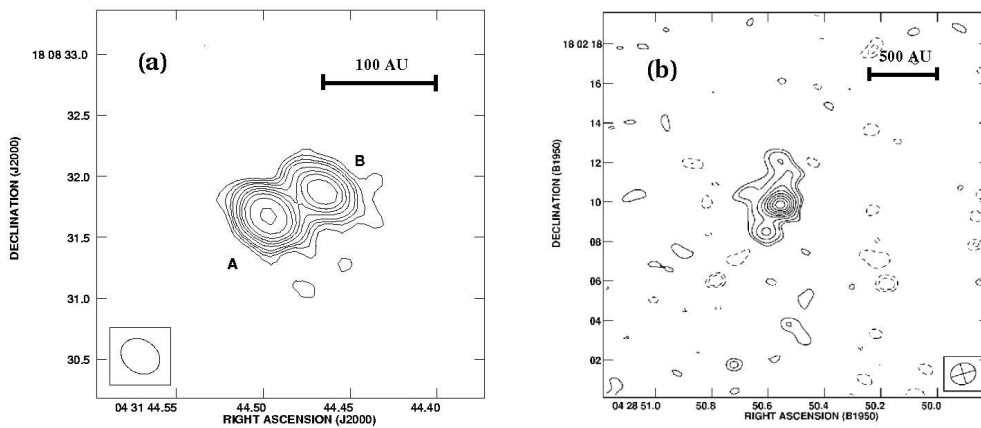


Figure 2.7: (a) 3.6 cm continuum of L1551 NE. Two sources are located in east-west direction with $0.5''$ separation. The western source (labeled A) is brighter than the eastern source (labeled B). (b) 1.3 mm continuum. The stronger central peak is the position of two 3.6 cm continuum source. Another peak is located $1.4''$ southeast of the central peak, proposed as a candidate protostar. The diffuse north-south elongation is interpreted as a circumbinary disk.

tems, has not been confirmed in the L1551 NE system. Moriarty-Schieven et al. (1995) detected blueshifted emission extending westward from L1551 NE with Jans Clerk Maxwell Telescope (JCMT), coincided with the optical/infrared reflection nebula (Figure 2.8) and inferred that the blueshifted emission is the molecular outflow. But the redshifted emission distributes in the surrounding of L1551 NE, not only in the eastern region, thus its bipolarity is still unclear. One reason makes it difficult to detect the molecular outflow is that, L1551 NE is located in the prominent outflow powered by L1551 IRS5, as shown in Figure 2.3. The redshifted lobe extends ~ 1 pc to the northeast of L1551 IRS5 and passes through the L1551 NE region.

In Figure 2.9 Yokogawa et al. (2003) showed an arc-shaped structure of CS emission westward of L1551 NE, with a velocity gradient along the outflow axis of L1551 IRS5. They were interpreted as the swept-up gas from L1551 IRS5 has collided with L1551 NE envelope, forming the bow-shock-like structure and the deceleration. The L1551 NE region is severely disturbed by the L1551 IRS5 outflow.

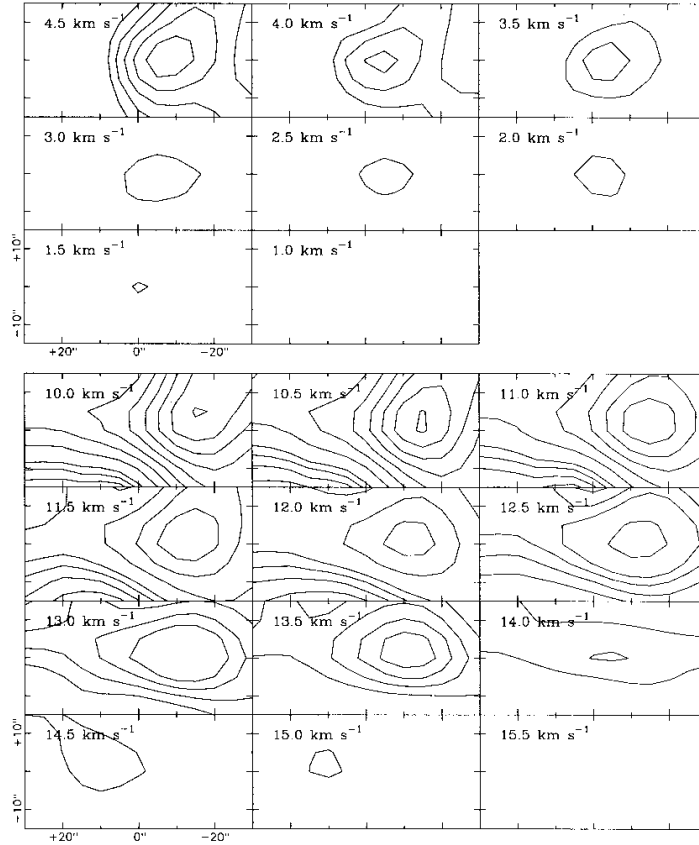


Figure 2.8: CO(3-2) emission around L1551 NE, obtained by Moriarty-Schieven et al. (1995) using James Clerk Maxwell Telescope (JCMT) with $\sim 14''$ beam size. L1551 NE is located at (0,0). Blueshifted emission (above) places westwards, coincident with infrared reflection nebula, but redshifted peaks (below) are not located eastward to L1551 NE. Channels with velocity between 4.5 km s^{-1} and 10 km s^{-1} were omitted because of confusion due to self-absorption and probable contamination from L1551 IRS5 outflow.

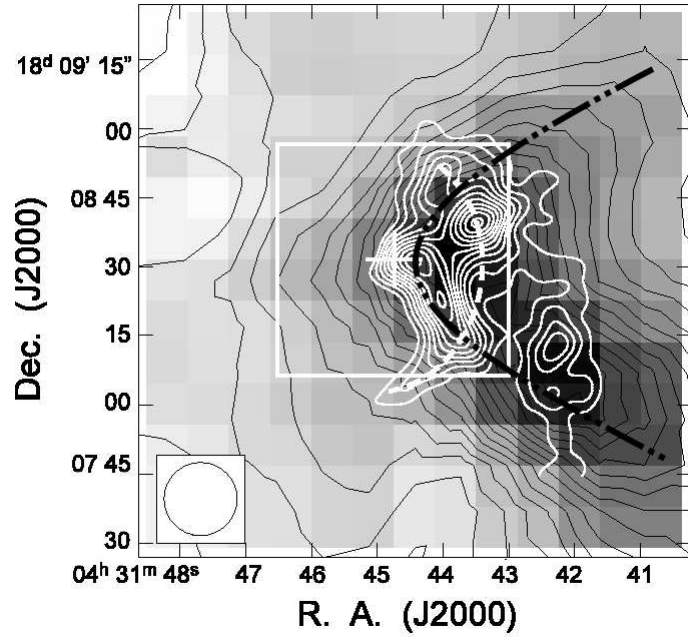


Figure 2.9: CS(2-1) maps taken by Nobeyama 45m telescope (the black contours) and Nobeyama Millimeter array (the white contours). The large-scale CS distribution mapped by Nobeyama 45m telescope shows an arc-shaped structure opens toward L1551 IRS5 (indicated by the black dash-dot line). This is resulted from the collision between the L1551 IRS5 outflow and L1551 NE envelope. A small-scale CS arc-shaped structure opens toward L1551 NE (the white dash) and has a velocity gradient to the direction of L1551 IRS5. This feature is due to the jet from L1551 NE is decelerated by the outside envelope (Yokogawa et al., 2003).

Chapter 3

Observation of L1551 IRS5 Protostellar System

3.1 Abstract

We studied the outflow of L1551 IRS5 within ~ 4000 AU of its driving source. Our SMA CO(2-1) observation provided the first high-angular resolution toward the vicinity of L1551 IRS5. Under an angular resolution of $\sim 4''$, we indentified three distinct components. The most prominent component is an X-shaped structure spanning $\sim 20''$ from the center. Its redshifted emission is located in the northeast side and blueshifted emission in the southwest side, which is similar to the large-scale outflow. The second prominent structure is an S-shaped structure spanning $\sim 10''$ from center. It has the similar symmetry axis to the large-scale outflow, but an opposite velocity pattern. The outer portion of this feature appears to twist north on the NE side and twist south on the SW side, creating an S-shape. The thrid component is a compact central component spanning $1''.4$ from center, with the same velocity pattern and similar symmetry axis to the large-scale outflow. This

component has a small linear extension, but the highest velocity among three components.

The X-shaped component likely comprises the limb-brightened walls of a cone-shaped cavity evacuated by the outflow from two main protostellar components. One of the cavity arms shows multiple kinematic components, which is also seen in single-dish telescope. The multiple kinematic components may be resulted from multiple outflow events. The compact central component likely comprises material within this cavity newly entrained by one or both outflow from the two main protostellar components. The S-shaped likely comprises a precession outflow, with its symmetry axis inclined to the opposite side of plane of the sky than the other two components. The morphology and kinematics of the S-shaped component can be described by a jet with a constant velocity and precesses at a constant angular velocity. This outflow may be driven by a recently reported candidate protostellar component in the L1551 IRS5 system, whose circumstellar disk is misaligned to the two main protostellar components. The tidal interaction between this circumstellar disk and the more massive northern component may cause the circumstellar disk to precess, thus the outflow of this component also precesses.

This work has been published in *The Astrophysical Journal* (Wu et al., 2009) and is presented in section 3.2. Section 3.3 is a supplement to Wu et al. (2009).

3.2 Multiple Bipolar Molecular Outflow from the L1551 IRS5 Protostellar System



MULTIPLE BIPOLAR MOLECULAR OUTFLOWS FROM THE L1551 IRS5 PROTOSTELLAR SYSTEM

PO-FENG WU^{1,2}, SHIGEHISA TAKAKUWA², AND JEREMY LIM²

¹ Institute of Astrophysics, National Taiwan University, No. 1, Section 4, Roosevelt Road, Taipei 106, Taiwan

² Academia Sinica Institute of Astronomy and Astrophysics, P.O. Box 23-141, Taipei, 106, Taiwan

Received 2008 December 4; accepted 2009 March 30; published 2009 May 19

ABSTRACT

The multiple protostellar system L1551 IRS5 exhibits a large-scale bipolar molecular outflow that spans ~ 1.5 pc on both the northeast (redshifted) and southwest (blueshifted) sides of the system. We have studied this outflow within ~ 4000 AU of its driving source(s) with the Submillimeter Array. Our CO(2–1) image at $\sim 4''$ (~ 560 AU) resolution reveals three distinct components: (1) an X-shaped structure spanning $\sim 20''$ from center with a similar symmetry axis and velocity pattern as the large-scale outflow; (2) an S-shaped structure spanning $\sim 10''$ from center also with a similar symmetry axis but opposite velocity pattern to the large-scale outflow; and (3) a compact central component spanning $\sim 1''$ from center again with a similar symmetry axis and velocity pattern as the large-scale outflow. The X-shaped component likely comprises the limb-brightened walls of a cone-shaped cavity excavated by the outflows from the two main protostellar components. The compact central component likely comprises material within this cavity newly entrained by one or both outflows from the two main protostellar components. The S-shaped component mostly likely comprises a precessing outflow with its symmetry axis inclined in the opposite sense to the plane of the sky than the other two components, taking the S-shaped component out of the cone-shaped cavity along most, if not all, of its entire length. This outflow may be driven by a recently reported candidate third protostellar component in L1551 IRS5, whose circumstellar disk is misaligned relative to the two main protostellar components. Gravitational interactions between this protostellar component and its more massive northern (and perhaps also southern) neighbor(s) may be causing the circumstellar disk and hence outflow of this component to precess.

Key words: ISM: jets and outflows – stars: formation – stars: individual (L1551 IRS5) – stars: low-mass, brown dwarfs – stars: pre-main sequence

Online-only material: color figure

1. INTRODUCTION

Most near-solar-mass stars are born as members of binary or multiple systems (Duquennoy & Mayor 1991; Mathieu 1994). The formation of such systems, although the preferred mode of star formation at least for near-solar-mass stars, is poorly understood. The main competing theoretical models are fragmentation of dense molecular condensations to form systems comprising multiple protostars, or capture of originally single protostars still embedded in their individual condensations to form multiple systems (e.g., review by Tohline 2002).

The most direct way of distinguishing between these two possibilities is to compare for a given system the properties of its individual protostars (i.e., orientation of their circumstellar disks and their orbital motion) with the properties of its surrounding molecular condensation (i.e., orientation and rotation). Such a study of the low-mass protostellar system L1551 IRS5 provides the most direct evidence yet that its two main protostellar components formed via the fragmentation of their surrounding parent molecular condensation (Lim & Takakuwa 2006). For many systems (especially those with closely separated components), however, the properties of their individual protostellar components are difficult to measure until the Extended Very Large Array (EVLA) or Atacama Large Millimeter and Submillimeter Array (ALMA) is completed. Indeed, at the present time, even the number of protostellar components present in a given system is not always clear.

Bipolar molecular outflows, found ubiquitously around protostars, are more easily accessible, and can be used to indirectly probe the properties of multiple protostellar systems. For example, such outflows can reveal the presence of currently

undetected or spatially unresolved protostellar components through their individual outflows. Outflows that wind in space with a helical pattern may have driving sources whose circumstellar disks and therefore jets are precessing due to gravitational interactions with closely separated protostellar companions. The degree of collimation and/or dynamical age of the outflow, as well as the opening angle of the outflow cavity at its base, can provide a guide to the evolutionary stage of the driving source.

Here, we study the bipolar molecular outflow associated with L1551 IRS5 at a high angular resolution with an interferometric array. This system was first found as an infrared source by Strom et al. (1976) in the nearby (distance ~ 140 pc) L1551 molecular cloud located in the constellation Taurus. L1551 IRS5 was the first protostellar source from which a bipolar molecular outflow, detected in single-dish observations of the CO(1–0) and CO(2–1) lines, was recognized (Snell et al. 1980). Subsequent single-dish observations in CO(1–0), CO(2–1), and CO(3–2) at higher angular resolutions have revealed the overall morphology and kinematics of this and a number of other outflows in the L1551 star-forming region on parsec scales (Uchida et al. 1987; Bachiller et al. 1994; Moriarty-Schieven et al. 1987; Moriarty-Schieven & Snell 1988; Moriarty-Schieven et al. 2006; Stojimirović et al. 2006). The most prominent of these outflows is centered on L1551 IRS5 and extends ~ 1.5 pc toward the northeast (NE) (redshifted lobe) and southwest (SW) (blueshifted lobe) directions at a position angle of $\sim 50^\circ$. Each outflow lobe has a U-shaped structure, together with knotty components having distinct velocities. The other outflows detected in the L1551 cloud have been associated with other driving sources except for a collimated redshifted outflow with one end near L1551 IRS5 and extending ~ 2 pc to the west, the origin of which is not known.

Apart from the large-scale bipolar molecular outflow, L1551 IRS5 is surrounded by a relatively compact molecular condensation (radius of ~ 1200 AU in C^{18}O) that has been best studied by Momose et al. (1998). This condensation is elongated in the northwest (NW)–southeast (SE) direction, perpendicular to the major axis of the large-scale bipolar molecular outflow. The measured kinematics indicate a flattened envelope that is rotating and contracting, also suggested in earlier observations by Ohashi et al. (1996) and Saito et al. (1996). This condensation has been observed in CS (7–6), which traces warmer and denser gas closer to the central protostellar system, by Takakuwa et al. (2004). In the inner region of the envelope, the kinematics is dominated by rotation.

The first indication that L1551 IRS5 may be a binary system was reported by Bieging & Cohen (1985), who showed that this system comprised two sources separated by ~ 0.3 (~ 42 AU) in the north-south direction at a wavelength of 2 cm. Subsequent studies resolved these two sources into twin ionized jets closely aligned with the large-scale bipolar molecular outflow (Rodríguez et al. 2003b). Looney, Mundy & Welch (1997) showed from high angular-resolution (~ 0.5) observations in the 2.7 mm continuum that L1551 IRS5 contains two circumstellar dust disks surrounded by a circumbinary dust disk and/or extended envelope. Rodríguez et al. (1998) spatially resolved the two circumstellar dust disks (along their major axes) for the first time at 7 mm, and showed that they are centered on the abovementioned twin ionized jets. Rodríguez et al. (2003a) showed that these two protostellar components were (likely) orbiting each other in a clockwise direction. Lim & Takakuwa (2006) spatially resolved the two circumstellar disks along both their major and minor axes, and showed that these disks are aligned with each other as well their surrounding rotating and flattened molecular condensation (pseudodisk). They also showed that the two components were orbiting each other in the same direction as the rotation of the pseudodisk. All these properties are consistent with the notion that the two protostellar components formed as a result of fragmentation in the central region of their surrounding pseudodisk. Finally, Lim & Takakuwa (2006) found a candidate third protostellar component located (in projection) near the northern protostellar component. The circumstellar disk of this third component is misaligned relative to the circumstellar disks of the two main components as well as their surrounding pseudodisk.

We report in this paper high angular resolution ($\sim 4''$) observations in CO(2–1) centered on the base of the large-scale bipolar molecular outflow from L1551 IRS5. There is, to the best of our knowledge, only one published interferometric image of this molecular outflow in CO that presented by Barsony et al. (1993) in CO(1–0), who studied relatively extended ($\gtrsim 1'$) features in the blue outflow lobe. In our study, we investigate the structure and kinematics of the outflow components detected within $\sim 30''$ of L1551 IRS5, their connection with the large-scale bipolar molecular outflow imaged with single-dish telescopes, and the likely nature of their driving sources.

Readers, interested in how the observations were conducted and data reduced, should now proceed to Section 2. Those interested only in the results of the CO(2–1) and simultaneous 1.3 mm continuum measurements can skip ahead to Section 3. In Section 4, we show that our CO(2–1) maps likely trace three separate outflow components: the limb-brightened walls of an outflow cavity, material in the cavity entrained by one or both jets from the two main protostellar components, and a candidate third precessing bipolar outflow. Readers interested only in a

Table 1
Observational Parameters

Parameter	Value
Right ascension (J2000)	04 ^h 31 ^m 34 ^s .14
Declination (J2000)	18°08' 05".1
Primary beam (FWHM)	$\sim 57''$
Synthesized beam (FWHM)	4".66 × 2".30 (P.A. = -66.7°)
Central frequencies	231.3 GHz, 241.3 GHz
Frequency (velocity) resolution	203.125 kHz (~ 0.264 km s ⁻¹)
Gain calibrators	0423-013 (9.4 Jy), 3C 120 (3.3 Jy)
Absolute flux and passband calibrator	Uranus
Rms noise level (continuum)	0.014 Jy beam ⁻¹
Rms noise level (line)	0.35 Jy beam ⁻¹ at 203.125 kHz resolution

concise summary of our results and interpretation can proceed directly to Section 5.

2. OBSERVATIONS AND DATA REDUCTION

Observations of L1551 IRS5 in CO(2–1) and 1.3 mm continuum were carried out using the SMA³ in its compact configuration on 2003 December 7. A description of the SMA can be found in Ho et al. (2004). The parameters of the observations are summarized in Table 1. Seven of the eight antennas of the SMA were available for the observations. We used the stronger quasar 0423-013, lying 19:6 from L1551 IRS5, for amplitude calibration, and the weaker quasar 3C 120, lying 12:8 from L1551 IRS5, for phase calibration. The flux density of 0423-013 was 9.4 Jy and that of 3C 120 was 3.3 Jy as measured with respect to Uranus, which served as the absolute flux calibrator.

The SMA has a double-sideband receiver in the 230 GHz (1.3 mm) band with a bandwidth of 2 GHz in each sideband. The lower sideband was tuned to a central frequency of 231.3 GHz, and the upper sideband 241.3 GHz. The signal in each sideband is fed into a correlator that distributes this signal to 24 spectral windows (“chunks” in the SMA nomenclature). Six of the chunks were divided into 512 channels, which in the CO(2–1) line results in a velocity resolution of 0.265 km s⁻¹ over a velocity range of 135 km s⁻¹. The remaining chunks were divided into 128 channels, and following calibration vector-averaged to make a single continuum channel at 1.3 mm with a total bandwidth of 4.0 GHz. The minimum projected baseline in our observation was ~ 8 k λ , allowing us to recover $\sim 30\%$ of the flux from the largest structure visible in our CO(2–1) maps of $\sim 15''$ (e.g., see Wilner & Welch 1994).

We calibrated the raw visibility data using MIR, which is an IDL-based data reduction package adopted for the SMA from the MMA software package originally developed for Owens Vally Radio Observatory (OVRO) (Scoville et al 1993). We adopted antenna-based calibration, which provides the best sensitivity as there were no significant baseline-based errors in our data. The calibrated visibility data were Fourier-transformed to produce DIRTY images, and the point-spread function of the telescope deconvolved (CLEANed) from these images using MIRIAD (Sault et al. 1995) to produce the final maps. A ROBUST parameter of 0.5 was adopted, which provided the best compromise between sensitivity and angular resolution.

To make the CO(2–1) channel maps, we first subtracted the continuum emission from the visibility data as derived from

³ The Submillimeter Array (SMA) is a joint project between the Smithsonian Astrophysical Observatory and the Academia Sinica Institute of Astronomy and Astrophysics and is funded by the Smithsonian Institution and the Academia Sinica.

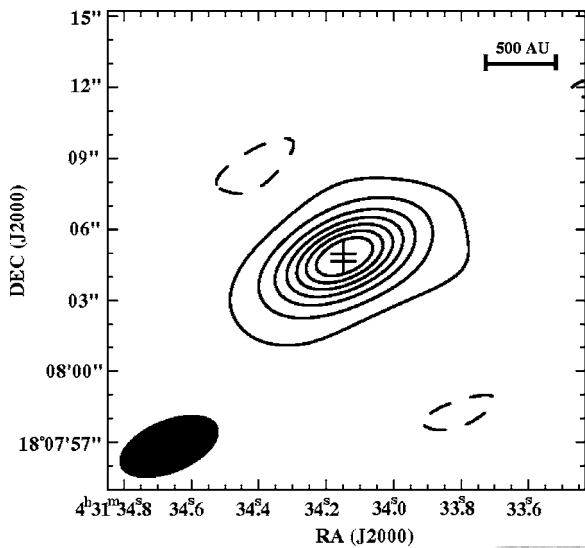


Figure 1. Continuum map of L1551 IRS5 at 1.3 mm. Contour levels are plotted at $-2, 2, 10, 20, 30, 40, 50, 60\sigma$, where the rms uncertainty $\sigma = 0.014 \text{ Jy beam}^{-1}$. Crosses indicate the position of the two main protostellar components at 7 mm as measured by Lim & Takakuwa (2006). The synthesized beam is shown as a filled ellipse at the bottom left corner.

a fit to the line-free channels. Unlike in the continuum where the emission is centrally concentrated, in CO(2–1) the emission in many channels is distributed in a complex manner over an extended region resulting in complicated sidelobe patterns. To CLEAN the channel maps, we first selected (i.e., place boxes enclosing) features that we believed to be real. Through trial and error, we converged on features that changed smoothly in structure between neighboring channels, as would be expected for real features. An examination of the residual maps (i.e., after the candidate real features and their sidelobes had been removed) revealed no systematic pattern (i.e., only random noise), indicating that all the real feature had indeed been correctly recovered. Thus, we believe that any artificial components incorrectly selected for CLEANing are much weaker than the real components in our maps.

3. RESULTS

3.1. 1.3 mm Continuum

Figure 1 shows our 1.3 mm continuum map of L1551 IRS5 at an angular resolution of $4''.66 \times 2''.33$. The continuum emission peaks at the location of the protostellar system, as seen in images at comparable angular resolution at 3 mm (Looney, Mundy & Welch 1997) and 0.8 mm (Takakuwa et al. 2004). We fitted a two-dimensional Gaussian to the continuum source to derive a total flux density of $1.20 \pm 0.01 \text{ Jy}$ and a deconvolved size at full-width half-maximum (FWHM) of $(1''.5 \pm 0''.1) \times (0''.8 \pm 0''.2)$ along a position angle of $146^\circ \pm 8^\circ$. The size of the continuum source is much larger than the separation of the two main protostellar components ($\sim 0.3''$), implying that at least a part of the emission arises from the surrounding envelope. Looney, Mundy & Welch (1997) found that, at 3 mm, about half of the continuum emission arises from the circumstellar dust disks of the two main protostellar components (their observation did not have sufficient angular resolution to spatially separate the candidate third protostellar component), and about half from the surrounding dust envelope. The continuum source detected here has an orientation similar to but size much smaller than the pseudodisk traced in C^{18}O by Momose et al. (1998), suggesting

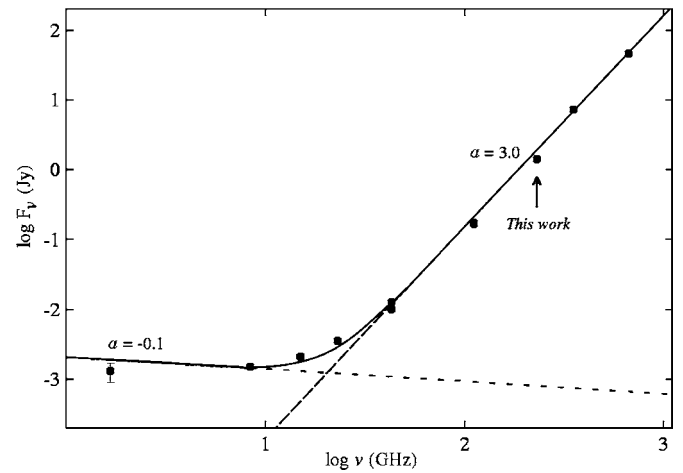


Figure 2. SED of the continuum emission from L1551 IRS5. The data points and their corresponding $\pm 1\sigma$ measurement uncertainties (where large enough to be seen) are tabulated in Table 2. The solid curve shows our best chi-squared fit assuming two power-law components with each having $F_\nu \propto \nu^\alpha$. One component has $\alpha \approx -0.1$ as indicated by the short-dashed line and dominates at low frequencies, and the other $\alpha \approx 3.0$ as indicated by the long-dashed line and dominates at high frequencies (see text).

Table 2
Continuum Flux Density of L1551 IRS5

Wavelength	Flux Density (mJy)	References ^a
18 cm	1.3 ± 0.4	1
3.6 cm	1.48 ± 0.04	1
2.0 cm	2.1 ± 0.2	1
1.3 cm	3.5 ± 0.4	1
7 mm	12.2 ± 1.0	1
7 mm	10.1 ± 0.7	2
2.7 mm	171 ± 19	3
2.7 mm	162 ± 6	4
1.3 mm	1200	This work
850 μm	7230	4
450 μm	45700	4

Note. ^a 1. Rodríguez et al. (1998); 2. Lim & Takakuwa (2006); 3. Momose et al. (1998); 4. Moriarty-Schieven et al. (2006).

that the extended part of the continuum emission traces the inner regions of the pseudodisk.

Both free-free emission from ionized jets and thermal emission from dust can contribute to the continuum emission. In L1551 IRS5, as in many protostellar systems, the ionized jets dominate the emission at centimeter wavelength, whereas dust contributes an increasingly larger fraction of the emission toward shorter wavelengths. To assess the relative contribution from each component at a given wavelength, we have collected all relevant measurements of the continuum emission for L1551 IRS5 at centimeter to submillimeter wavelength as listed in Table 2. Figure 2 shows the spectral energy distribution (SED) of the continuum emission based on the tabulated data. We modeled the SED as the sum of two power-law components with each component having $F_\nu \propto \nu^\alpha$, where F_ν is the intensity at a given frequency ν and α the power-law index. A chi-squared fit to the data gives one component with $\alpha = -0.1 \pm 0.1$ that dominates at low frequencies (the short-dashed line in Figure 2), consistent with optically thin free-free emission. The other component has $\alpha = 3.0 \pm 0.1$ that dominates at high frequencies (the long-dashed line in Figure 2), consistent with thermal emission from dust. As can be seen, the contribution from free-free emission to the continuum at 1.3 mm is only $\sim 0.1\%$.

Assuming that the dust temperature (T_d) is uniform, we can estimate the total dust mass of the continuum source from the relationship

$$M = \frac{F_\nu d^2}{B_\nu(T_d) \kappa_\nu}, \quad (1)$$

where d is the distance to the source, B_ν is the blackbody function, T_d is the dust temperature, and κ_ν is the dust mass opacity coefficient given by $\kappa_\nu = 0.1 (\nu/10^{12} \text{ Hz})^\beta \text{ cm}^2 \text{ g}^{-1}$ (Beckwith & Sargent 1991). The quantity β is related to the spectral index α of the dust continuum emission by the relationship $\alpha = 2 + \beta$. Assuming $T_d = 47 \text{ K}$ (Moriarty-Schieven et al. 1994), the dust mass inferred from Equation (1) is $0.06 \pm 0.01 M_\odot$. This value is in reasonable agreement with those derived at 2.7 mm that are sensitive to the same size scales (Ohashi et al. 1991; Momose et al. 1998).

3.2. CO (2–1)

Figure 3 shows our CO (2–1) channel maps of L1551 IRS5. For presentation purposes, none of the maps displayed in this paper have been corrected for the primary beam response of the SMA; the quantities we computed were, of course, derived from maps corrected for the primary beam response. Emission is detectable over the velocity range $0.2\text{--}10.5 \text{ km s}^{-1}$ measured with respect to the local standard of rest (V_{LSR}). We estimate, based on the symmetry of the features observed (see below), a systemic velocity of $\sim 6.5 \text{ km s}^{-1}$ for the L1551 IRS5 protostellar system, comparable to previous estimates (Fridlund et al. 2002). The absence of emission within $\sim 0.5 \text{ km s}^{-1}$ of the systemic velocity is likely caused by extended emission (mostly from the ambient molecular cloud) that is resolved by the interferometer.

3.2.1. X-Shaped Structure

Figure 4 shows the integrated CO(2–1) intensity map at blueshifted velocities spanning $0.2\text{--}5.5 \text{ km s}^{-1}$ (blue contours) and redshifted velocities spanning $7.4\text{--}10.5 \text{ km s}^{-1}$ (red contours) separately. To make this map, we first applied Hanning smoothing (a triangular function of width five channels at zero intensity) to the channel maps, and then excluded all features in the channel maps where the intensity in the corresponding smoothed maps is less than 1.5σ . The most prominent feature in this map is an X-shaped structure (as indicated by the diagonal lines) that has its blueshifted pair of arms lying west and its redshifted pair of arms lying east of the protostellar system. In the channel maps of Figure 3, the blueshifted part of this X-shaped structure can be most clearly seen at velocities spanning $2.3\text{--}5.2 \text{ km s}^{-1}$ and the redshifted part $7.6\text{--}10.5 \text{ km s}^{-1}$. Both pairs of arms have an opening angle of $\sim 90^\circ$, and extend $\sim 20''\text{--}30''$ ($\sim 3000\text{--}4000 \text{ AU}$) from center. They have a symmetry axis along the NE–SW direction at a position angle of about 70° , which is close to the orientation of the major axes of the ionized jets as well as the large-scale bipolar molecular outflow. Furthermore, the X-shaped structure exhibits the same velocity pattern (i.e., redshifted to the E and blueshifted to the W) as the large-scale bipolar molecular outflow.

In both the channel maps of Figure 3 and integrated-intensity map of Figure 4, the blueshifted NW arm can be seen to be much broader than the other three arms of the X-shaped structure. A close examination of the channel maps reveals that the NW arm comprises several distinct and relatively compact (bullet-like) spatial-kinematic components. For example, the broadest portion of the NW arm at about $10''$ from center (see Figure 4)

is dominated by a pair of comparatively high-velocity bullets that can be best seen in the channel maps (Figure 3) at velocities of $2.1\text{--}3.4 \text{ km s}^{-1}$. The tip of the NW arm is dominated by two lower-velocity bullets that can be best seen in the channel maps at $3.7\text{--}4.7 \text{ km s}^{-1}$. On the other hand, the two redshifted arms each comprise only one spatial-kinematic component (see below). In this way, the properties of the X-shaped component seem to mirror that of the large-scale bipolar molecular outflow. Several distinct spatial-kinematic components have been seen in single-dish CO(2–1) observations spaced at semi-regular intervals along the blueshifted outflow lobe of L1551 IRS5 (Bachiller et al. 1994). Curiously, no such distinct components are present in the same observations of the redshifted outflow lobe.

Figure 5 shows position-velocity (PV) diagrams along each opposing set of arms as indicated by the diagonal lines in Figure 4. The straight lines drawn in Figure 5 are not meant to guide the eye, but instead are our model fits to the PV diagrams as we shall describe in Section 4.1. The PV diagrams along the NE (Figure 5(a), the upper right quadrant) and SE (Figure 5(b), the upper right quadrant) arms look very similar, with each having a velocity at peak intensity that increases with radial distance (i.e., Hubble-like expansion) out to $\sim 20''$ from center. The SW arm (Figure 5(a), the lower left quadrant) is only weakly detected in the PV diagram, but nevertheless can be seen to have a velocity gradient comparable to the NE and SE arms. On the other hand, the PV diagram along the NW arm (Figure 5(b), the lower left quadrant), shows at least two distinct velocity components. The component labeled NW-a increases comparatively quickly in velocity with radial distance out to $\sim 10''$ from center. The component labeled NW-b increases more slowly in velocity with radial distance out to $\sim 30''$ from center. NW-a corresponds to the pair of higher-velocity bullets and NW-b to the pair of lower-velocity bullets mentioned above. Neither of these components have a velocity gradient that matches the comparable velocity gradients of the other three arms of the X-shaped component.

3.2.2. S-Shaped Structure

The next most prominent feature in the integrated-intensity map of Figure 4 is located between the blueshifted and redshifted arms of the X-shaped structure and extends to $\sim 10''$ from center. The outer portion of this feature on the NE side appears to twist north and that on the SW side twist south, creating an S-shaped structure. Its symmetry axis is oriented at a position angle of about 55° , approximately aligned with the symmetry axis of the X-shaped component as well as major axis of the large-scale bipolar molecular outflow.

The S-shaped structure exhibits blueshifted velocities NE of center, and redshifted velocities SW of center. The velocity pattern of the S-shaped structure is therefore opposite to that of both the X-shaped structure and large-scale bipolar molecular outflow. In the channel maps of Figure 3, the blueshifted part of the S-shaped structure can be seen most clearly at velocities spanning $3.4\text{--}5.5 \text{ km s}^{-1}$ and the redshifted part $7.4\text{--}8.2 \text{ km s}^{-1}$. The line-of-sight velocity of the S-shaped structure therefore does not reach velocities as high (far from V_{sys}) as the X-shaped structure. As described in Section 4.3.2, this structure exhibits an approximately sinusoidal variation in its radial velocity along its length.

3.2.3. Compact Central Component

Finally, a compact component centered on the location of L1551 IRS5 can be seen in the channel maps of Figure 3

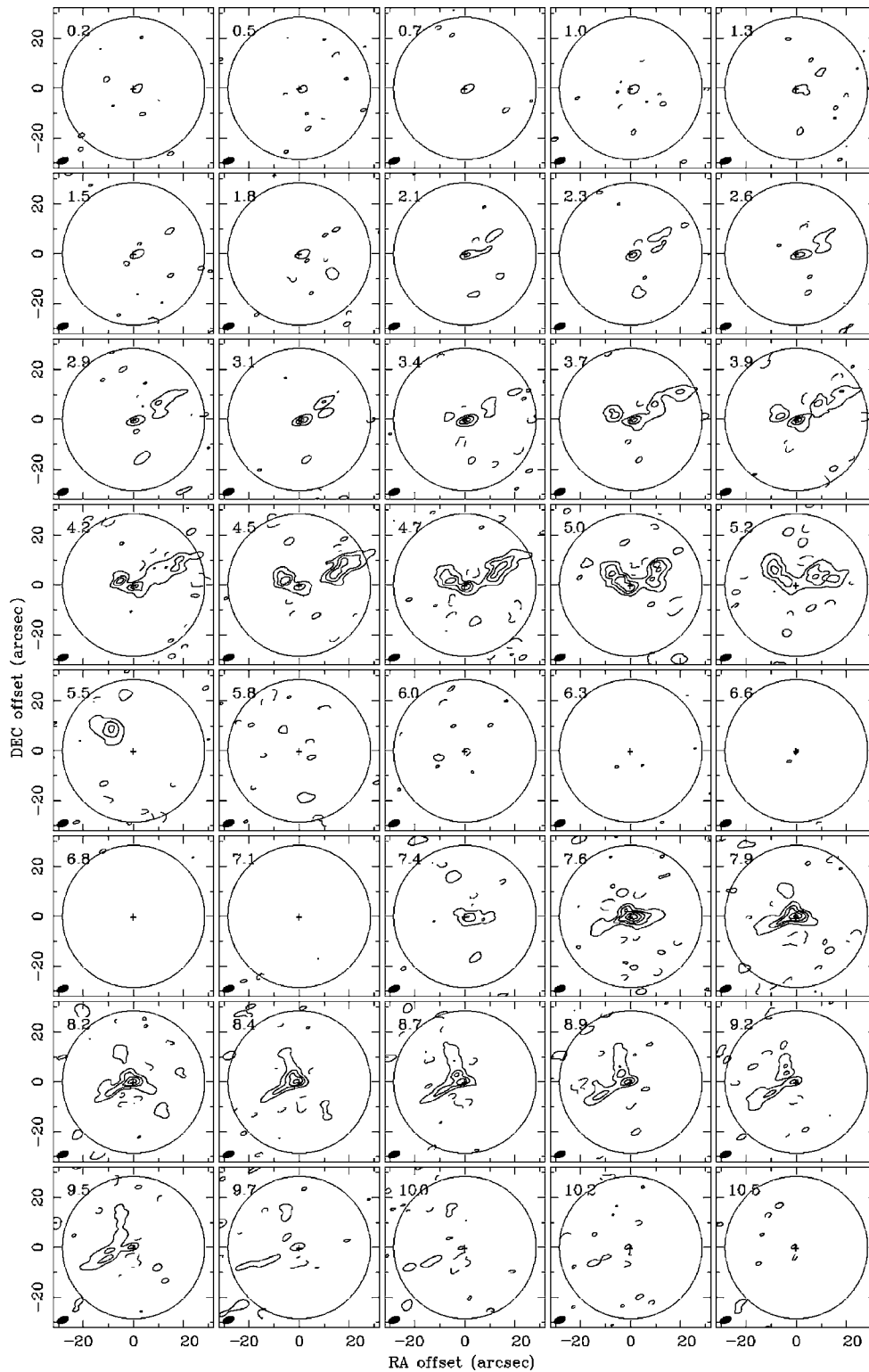


Figure 3. CO(2–1) channel maps of L1551 IRS5. Contours levels are plotted at $-3, 3, 6, 9, 15, 25, 35,$ and 45σ , where $\sigma = 0.35 \text{ Jy beam}^{-1}$. The central V_{LSR} of each channel is shown at the top left corner of each panel. Crosses indicate the positions to the two main protostellar components as in Figure 1. The field of view of the SMA at FWHM is shown by the large circle, and the synthesized beam by the filled ellipse at the bottom left corner.

extending to higher blueshifted and redshifted velocities than either the X- or S-shaped components. It is the only detectable or dominant component visible at blueshifted velocities spanning $0.2\text{--}3.4 \text{ km s}^{-1}$ and redshifted velocities spanning $9.2\text{--}10.5 \text{ km s}^{-1}$. In the integrated-intensity map of Figure 4, although difficult to visually separate from the base of the X- or

S-shaped structures, the compact central component comprises the closest redshifted and blueshifted intensity peaks straddling the L1551 IRS5 protostellar system.

To better extract the properties of the compact central component, we have fitted a two-dimensional Gaussian structure to this component at each velocity where it is detectable in the

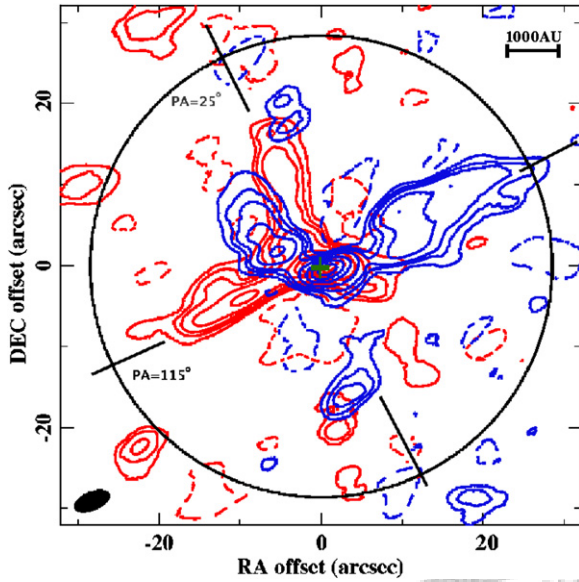


Figure 4. Integrated CO(2–1) intensity map with blue contours showing emission at blueshifted velocities spanning $V_{\text{LSR}} = 0.23\text{--}5.5 \text{ km s}^{-1}$, and red contours emission at redshifted velocities spanning $V_{\text{LSR}} = 7.4\text{--}10.5 \text{ km s}^{-1}$. For the blueshifted emission, contour levels are plotted at $-1.3, 1.3, 2.6, 3.9, 6.4, 10.7, 15.0,$ and $19.3 \text{ Jy km s}^{-1} \text{ beam}^{-1}$, while for the redshifted emission, contour levels are at $-1.0, 1.0, 2.0, 3.0, 5.1, 8.5, 11.9,$ and $15.3 \text{ Jy km s}^{-1} \text{ beam}^{-1}$. The cross indicates the location of L1551 IRS55 protostellar system. The field of view of the SMA at FWHM is shown by the large circle, and the synthesized beam by the filled ellipse at the lower left corner. Diagonal lines indicate the orientation of cuts in the position–velocity diagrams shown in Figure 5.

channel maps. Figure 6 shows the integrated CO(2–1) intensity map made from the derived fits with the blueshifted and redshifted emission plotted separately. The centroids of the redshifted and blueshifted emissions are displaced by $\sim 1''.4$ ($\sim 200 \text{ AU}$) NE and SW from center, respectively, at a position

angle of about 65° . The kinematic axis of this component is therefore closely aligned with the symmetry/major axis of, and has the same velocity pattern as, the X-shaped component and large-scale bipolar molecular outflows.

3.2.4. Base of X-Shaped and S-Shaped Components

To better study the structure of the X- and S-shaped components near their base, we have subtracted the compact central component from the channel maps using the abovementioned fits to this component (Section 3.2.3). Figure 7 shows the integrated CO(2–1) intensity maps made before (the upper row) and after (the lower row) the compact central component was subtracted, separated into two different velocity regimes. The higher velocity regime (Figure 7, the left column) spans $0.2\text{--}3.4 \text{ km s}^{-1}$ (i.e., $<V_{\text{LSR}} - 3.1 \text{ km s}^{-1}$) at blueshifted velocities (blue contours) and $8.9\text{--}10.5 \text{ km s}^{-1}$ ($>V_{\text{LSR}} + 2.4 \text{ km s}^{-1}$) at redshifted velocities (red contours). The lower velocity regime (Figure 7, the right column) spans $3.7\text{--}5.5 \text{ km s}^{-1}$ ($>V_{\text{LSR}} - 2.8 \text{ km s}^{-1}$) at blueshifted velocities (blue contours) and $7.4\text{--}8.7 \text{ km s}^{-1}$ ($<V_{\text{LSR}} + 2.2 \text{ km s}^{-1}$) at redshifted velocities (red contours). Like before, to make these maps we first applied Hanning smoothing (a triangular function of width five channels at zero intensity) to the channel maps, and then excluded all features in the channel maps where the intensity in the corresponding smoothed maps is less than 1.5σ .

The S-shaped component, which as mentioned above does not reach velocities as high as the X-shaped component, is barely detectable in the higher velocity regime. In this regime, the compact central component can be well separated from the X-shaped component as can be seen by comparing the map made before and after subtraction. In the lower velocity regime, all three components are detectable. The compact central component dominates the emission close to the protostellar system, as can be seen by comparing the map made before and after subtraction.

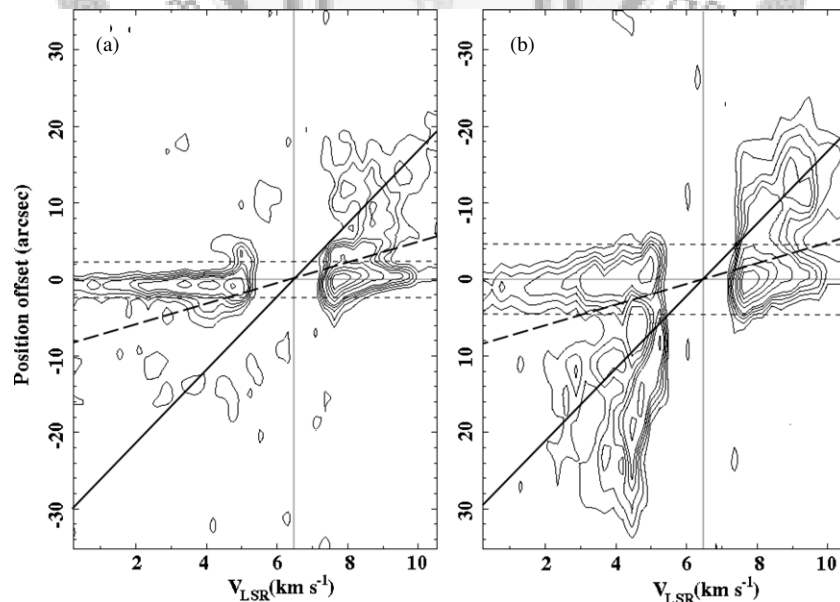


Figure 5. PV diagrams of the CO(2–1) emission along position angles (a) 25° and (b) 115° passing through the arms of the X-shaped component and central protostellar system (see Figure 4). Contour levels are plotted at $0.7, 1.4, 2.1, 2.8, 3.5, 5.5, 7.5, 9.5,$ and $11.5 \text{ Jy beam}^{-1}$. In each panel, the pair of horizontal short-dashed lines straddling the horizontal solid line (which indicates the position of the protostellar system) are separated by twice the FWHM of the synthesized beam at that particular position angle. Emission within this region is dominated by the compact central component (see text). The vertical line indicates the systemic velocity that we inferred for L1551 IRS55. The dark solid lines are the predictions of our model described in Section 4.1. The long-dashed lines are the predictions of a model described in Section 4.3.1. Note that panel (b) has been inverted vertically to show that three of the four arms (except the blueshifted NW arm) share the same velocity pattern (see text).

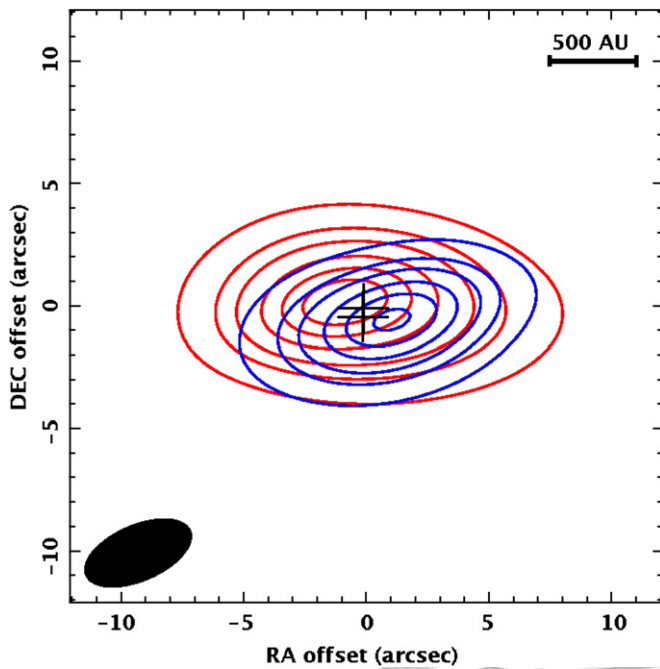


Figure 6. Integrated CO(2–1) intensity map constructed from Gaussian fits to the compact central component in the channel maps (see text). Blue contours show emission at blueshifted velocities spanning 0.23–5.5 km s^{−1}, and red contours show emission at redshifted velocities spanning 7.4–10.5 km s^{−1}. Contour levels are plotted at −3, 3, 9, 15, 25, 35, and 45σ, where σ = 0.43 Jy km s^{−1} beam^{−1} for the blueshifted and σ = 0.34 Jy km s^{−1} beam^{−1} for the redshifted emission. The synthesized beam is shown as a filled ellipse at the bottom left corner.

(A color version of this figure is available in the online journal.)

3.2.5. Physical Parameters

We have estimated physical parameters for all three components separately after correcting our maps for the primary beam response of the SMA antennas. For simplicity, we assume that the observed CO(2–1) emission is optically thin, in local thermal equilibrium (LTE), and has an excitation temperature of 10 K as derived by Stojimirović et al. (2006) based on the intensity ratio between CO(3–2) and CO(1–0). We also assumed an H₂-to-CO abundance ratio of 10⁴. We adopted an inclination of 30° with respect to the plane of the sky for all three components, such that their major axes are orthogonal to the equatorial plane of the circumstellar disks of the two main protostellar components and their surrounding flattened condensation (Lim & Takakuwa 2006). As discussed later (Section 4.3), the adopted inclination is probably appropriate for the X-shaped and compact central components, and close to median value in the allowed range from our model fit for the S-shaped component (but with the NE side the near side, opposite to the X-shaped and compact central components).

In Table 3, we tabulate for each component its estimated mass M , outflow momentum $P = \sum_v M(v) v$, kinetic energy $E = \frac{1}{2} \sum_v M(v) v^2$, mass-loss rate $\dot{M} = \sum_v M(v)/\tau(v)$, and dynamical age corresponding to the maximum derived dynamical time $\tau(v) = v/r$, where r is the distance from the driving source to the emission peak of the outflowing gas at a given velocity v . Note that all these values except for dynamical age are lower limits, in part because we have assumed that the CO(2–1) emission is optically thin, and in part because emission close to the systemic velocity was entirely resolved out. The X-shaped component, which is the most obvious component in our map, dominates in mass, momentum, and energy. It also

has the oldest dynamical age. The mass-loss rate is highest for the compact central component, which also has the youngest dynamical age.

4. DISCUSSION

Our CO(2–1) map at an angular resolution of 2".3 × 4".7 reveals, for the first time, three distinct bipolar molecular outflow components in the vicinity (≲ 4000 AU) of the L1551 IRS5 protostellar system. In the following, we shall discuss the likely nature of each of these components as well as their driving sources.

4.1. X-Shaped Component

The X-shaped component has a symmetry axis closely aligned with, and exhibits the same velocity pattern as, the large-scale bipolar molecular outflow. It has the largest mass, momentum, and energy of the three outflow components that we detected in the vicinity of the L1551 IRS5 protostellar system. This X-shaped component resembles similar structures seen around a number of other protostars such as IRS1 in Barnard 5 (Velusamy & Langer 1998), IRAS 20582+7724 in L1228 (Arce & Sargent 2004), and IRAS 5295+1247 in L1528B (Arce & Sargent 2005). In all these cases, the X-shaped structure observed is thought to comprise the limb-brightened walls of a cone-shaped cavity entrained and excavated by outflows from the central protostars. Indeed, scattered light from a cone-shaped cavity can be seen in the near-IR on the SW side of L1551 IRS5 (Hodapp 1994) with an opening angle comparable to that measured for the (blueshifted) arms of the X-shaped component. (The NE side of the cavity is presumably obscured in the near-IR by material in the condensation and extended envelope.)

Arce & Sargent (2006) have conducted a ¹²CO survey of molecular outflows within ≲ 10⁴ AU of nine protostellar (comprising a mixture of both single and multiple) systems at different evolutionary stages. They found a clear difference in the morphology of the molecular outflow lobes between Class 0 and more evolved Class I protostars. Class 0 protostars exhibit relatively collimated jet-like outflows or cone-shaped lobes with opening angles <55°, whereas Class I protostars have outflow lobes with wider opening angles of >75° (with ∼125° the largest opening angle seen). L1551 IRS5 is classified (based on its Infrared SED) as a Class I protostar (Keene & Masson 1990), and so the opening angle of its outflow cavity (∼90°) is comparable with that seen around other protostars at a similar evolutionary stage.

Near-IR observations in the [Fe II] line by Pyo et al. (2002, 2005) have revealed two velocity components in the ionized outflow from the main northern protostellar component in L1551 IRS5. One of these outflow components comprises a high-velocity (∼300 km s^{−1}) and narrowly collimated wind, and the other a low-velocity (∼100 km s^{−1}) and wide-angle wind. The latter has an opening angle of ∼100°, which is similar to the opening angle of the cavity seen through scattered light in the near-IR and as the X-shaped component. The X-shaped component may therefore have formed in two steps: first the high-velocity and narrowly collimated wind passes through and, in the process, entrains molecular gas (e.g., Stahler 1994), followed by a low-velocity and wide-angle wind that pushes forward and aside the molecular gas to excavate a cone-shaped cavity. Bachiller et al. (1994) have found that the large-scale bipolar molecular outflow associated with L1551 IRS5 exhibits several successive high-velocity features along its blueshifted

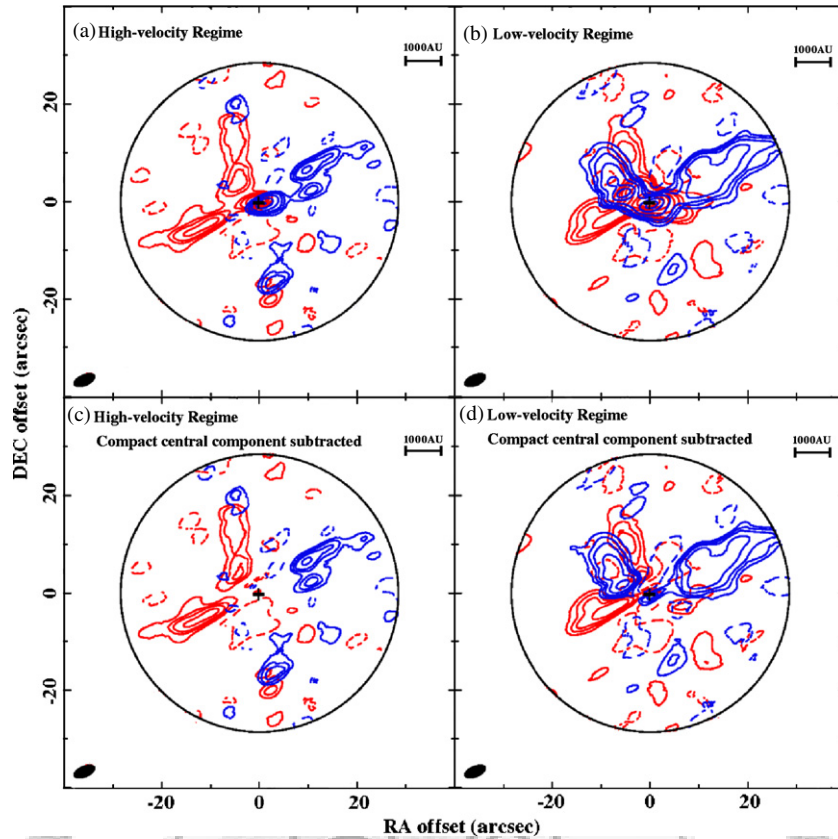


Figure 7. Integrated CO(2–1) map with the compact central component included (the upper row) and with it subtracted (the lower row) separated into two velocity regimes (left and right columns). In the higher velocity regime (the left column), the blue contours span velocities $0.23\text{--}0.34\text{ km s}^{-1}$ and the red contours $8.9\text{--}11\text{ km s}^{-1}$. In the lower velocity regime (the right column), the blue contours span velocities $3.7\text{--}5.5\text{ km s}^{-1}$ and the red contours $7.4\text{--}8.7\text{ km s}^{-1}$. In the left column, blue contour levels are plotted at $-1.0, 1.0, 2.0, 3.0, 5.1, 8.5, 11.9,$ and $15.3\text{ Jy km s}^{-1}\text{ beam}^{-1}$ and red contour levels are plotted at $-0.8, 0.8, 1.5, 2.3, 3.8, 6.3, 8.8,$ and $11.3\text{ Jy km s}^{-1}\text{ beam}^{-1}$. In the right column, blue contour levels are plotted at $-0.8, 0.8, 1.6, 2.4, 3.9, 6.5, 9.1,$ and $11.7\text{ Jy km s}^{-1}\text{ beam}^{-1}$ and red contour levels are plotted at $-0.7, 0.7, 1.4, 2.1, 3.5, 5.8, 8.1,$ and $10.4\text{ Jy km s}^{-1}\text{ beam}^{-1}$.

Table 3
Properties of the Three Outflow Components

		Mass (M) ($10^{-3} M_{\odot}$)	Momentum (P) ($10^{-3} M_{\odot}\text{ km s}^{-1}$)	Energy (E) (10^{40} erg)	Mass-loss rate (\dot{M}) ($10^{-7} M_{\odot}\text{ yr}^{-1}$)	Dynamical Age (yrs)
X-shaped	Red lobe	0.48	2.28	12.12	2.60	1.3×10^4
	Blue lobe	0.77	4.07	25.25	3.37	1.2×10^4
S-shaped	Red lobe	0.09	0.34	1.45	0.42	6.3×10^3
	Blue lobe	0.29	0.94	3.44	1.80	7.4×10^3
Central	Red lobe	0.29	0.95	3.56	10.98	2.7×10^2
	Blue lobe	0.22	1.33	9.66	11.00	2.0×10^2

lobe, suggestive of different ejection episodes. The X-shaped component may therefore comprise (primarily) the base of that portion of the larger-scale outflow created in the latest ejection episode.

We now investigate what properties a cone-shaped outflow cavity should have to reproduce both the observed structure and kinematics of the X-shaped component. Figure 8 shows a sketch of a cone with a half-opening angle θ and its symmetry axis inclined by an angle i to the plane of the sky. As suggested by the PV-diagrams of Figure 5, we assume that the cone exhibits a Hubble-like radial expansion such that its radial velocity is given by $v_r = Cr$, where C is the coefficient of the radial flow and r is the radial distance from the driving source. We assume $i = 30^\circ$ so that the symmetry axis is orthogonal to the circumstellar disks of the two main protostellar components (see Lim & Takakuwa 2006) and measure from the integrated-

intensity map of Figure 4 a half-opening angle of $\theta \approx 45^\circ$. The only free parameter is therefore C , which in the PV diagram of Figure 5 specifies the observed velocity gradient along the arms of the X-shaped component. We found that a satisfactory fit to all except the blueshifted NW arm can be obtained with $C = 0.18\text{ km s}^{-1}\text{ arcsec}^{-1}$, and plot the model fit as solid lines in the PV diagram of Figure 5. As mentioned in Section 3.2.1, the blueshifted NW arm exhibits two distinct velocity components in the PV diagram of Figure 5, neither of which have velocity gradients that matches the otherwise similar velocity gradients along the other three arms.

The acceleration constant of the Hubble-like radial expansion estimated for the X-shaped component of $C \approx 0.18\text{ km s}^{-1}\text{ arcsec}^{-1} \approx 250\text{ km s}^{-1}\text{ pc}^{-1}$ is much higher than that estimated from single-dish observations for the large-scale bipolar molecular outflow from L1551 IRS5 of

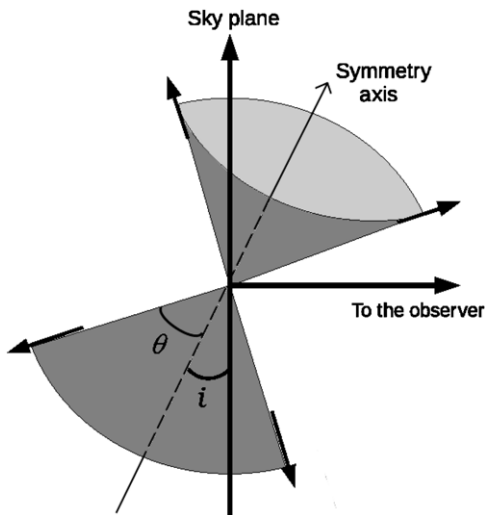


Figure 8. Schematic picture of a cone-shaped outflow cavity that constitutes our model for the X-shaped component. The cone has a half-opening angle of θ and is inclined by an angle i to the plane of the sky. The arrows indicate the direction of gas motion, which are along the cavity walls.

$\sim 70 \text{ km s}^{-1} \text{ pc}^{-1}$ (Fridlund et al. 1989). Interferometric observations of the bipolar molecular outflow from B335 reveal an even higher acceleration constant of $\sim 490 \text{ km s}^{-1} \text{ pc}^{-1}$ (H.-W. Yen 2009, in preparation). On the other hand, the acceleration constant of the Hubble-like radial expansion of large-scale ($>0.1 \text{ pc}$) molecular outflows in other low-mass protostars has measured values of $\sim 65 \text{ km s}^{-1} \text{ pc}^{-1}$ in L1157 (Bachiller et al. 2001), $\sim 97 \text{ km s}^{-1} \text{ pc}^{-1}$ in both L483 (Tafalla et al. 2000) and BHR 71 (Bourke et al. 1997), and $\sim 120 \text{ km s}^{-1} \text{ pc}^{-1}$ in IRAM 04191+1522 (André et al. 1999). All these values are lower than that measured in interferometric observations of either L1551 IRS5 or B335 that probe the base of their respective outflows, suggesting that the acceleration constant of the Hubble-like radial expansion decreases outward along a given outflow lobe.

4.2. Compact Central Component

The compact central component has its major axis aligned with the symmetry axis of the X-shaped component, as well as major axis of the large-scale bipolar molecular outflow. Furthermore, it exhibits the same velocity pattern as both these more spatially extended components. Together with the fact that it reaches much higher blueshifted and redshifted velocities than the X-shaped component, the compact central component most likely comprises material lying along the symmetry axis of the cone-shaped cavity that has been entrained relatively recently by the jet(s) from one (or both) of the two main protostellar components. High angular-resolution observations of the bipolar molecular outflows from other protostars also sometimes show a relatively collimated outflow lying along the symmetry axis of a cone-shaped outflow cavity (e.g., HH211; Gueth & Guilloteau 1999), with the more collimated component attributed to molecular gas entrained by a jet.

Fridlund & Liseau (1998) found that the two optical jets visible on the SW side of L1551 IRS5 have velocities of $\sim 300 \text{ km s}^{-1}$. As mentioned in Section 4.1, Pyo et al. (2002, 2005) found that the component at higher velocities of $\sim 300 \text{ km s}^{-1}$ in the northern optical jet is narrowly collimated. Fridlund & Liseau (1998) inferred, based on the observed H α and [S II] line intensities, a particle density of $\sim 10^4 \text{ cm}^{-3}$ in these jets, and therefore a momentum for each jet

of $\sim 7 \times 10^{-4} M_{\odot} \text{ km s}^{-1}$. The combined momentum of the optical jets is therefore comparable with the momentum we inferred for the compact central component of $\sim 1.33 \times 10^{-3} M_{\odot} \text{ km s}^{-1}$, demonstrating that the optical jets indeed have sufficient momentum to drive the compact central component. At their velocities of $\sim 300 \text{ km s}^{-1}$, the optical jets would travel the entire length of the compact central component in just $\sim 30 \text{ yr}$. The presence of newly entrained molecular gas in the outflow cavity may indicate that a significant quantity of molecular gas has recently been injected into this cavity from the surrounding infalling envelope, which tries to fill or is diverted into the cavity at or near its base. Alternatively, or in addition, a relatively recent enhancement in the activity (i.e., mass-loss rates) of one or both optical jets has led to an enhancement in the amount of entrained material in the cavity.

Using the *Chandra X-ray Observatory*, Bally et al. (2003) have detected a compact, but slightly resolved, X-ray source located about $0'.5\text{--}1''$ southwest of L1551 IRS5 at the base of the two optical jets. They proposed several models for how the observed X-ray emission may be produced, all of which involve radiating plasma downstream of a shock where either (1) a wide-angle flow, launched and accelerated within a few AU of one member of the IRS 5 protobinary, is redirected and collimated into a jet; (2) one or both jets collide with a circumbinary disk; and (3) the two jets collide. Here, we propose that shocks produced when one or both jets slam into molecular gas, diverted into the X-shaped cavity, provide a simpler if not more plausible explanation for the observed X-ray emission. The resulting entrained molecular gas would be expected to extend beyond the location of the X-ray source, as observed for the compact central component. To produce the observed X-ray luminosity and plasma temperature, Bally et al. (2003) find that a preshock gas density of $1\text{--}10 \times 10^3 \text{ cm}^{-3}$ and shock velocities larger than 350 km s^{-1} are required. Such molecular hydrogen gas densities are required to excite the observed CO(2–1) emission from the compact central concentration. The line-of-sight velocity of at least one of the two optical jets reaches $\sim 300 \text{ km s}^{-1}$, and if inclined by $\sim 30^\circ$ to the plane of the sky as inferred by Lim & Takakuwa (2006) would therefore reach true velocities of $\sim 600 \text{ km s}^{-1}$. Such high jet velocities can produce the required shock velocities.

Instead of tracing an outflow, could the compact central component constitute the inner region of the flattened molecular condensation around L1551 IRS5? In such a case, the observed NE-SW velocity gradient would then correspond to infalling motion seen in C 18 O(1–0) (Momose et al. 1998). The measured velocity gradient caused by the infalling motion at the same scale as the compact CO(2–1) central component ($\sim 300 \text{ AU}$) is at most $\sim 0.13 \text{ km s}^{-1} \text{ arcsec}^{-1}$ (see Figure 3 in Momose et al. 1998). For comparison, the measured velocity gradient of the compact central component is at least $\sim 0.60 \text{ km s}^{-1} \text{ arcsec}^{-1}$. Furthermore, as shown by Takakuwa et al. (2004), the inner region of the condensation is dominated by rotation and not infall, and exhibits a velocity gradient in the NW–SE direction (along the major axis of the condensation) and not NE–SW direction. Thus, the compact central component is unlikely to comprise the inner regions of the condensation around L1551 IRS5.

4.3. S-Shaped Component

The S-shaped component would not have been spatially resolved and hence recognized in previous single-dish CO observations. Given that it exhibits a velocity pattern opposite

to the compact central component, X-shaped component, and large-scale bipolar molecular outflow, at first sight it is unlikely to comprise material entrained by the collimated winds of the two main protostellar components. Furthermore, this component exhibits the lowest (projected) maximum detectable velocity of all three components. Below, we consider three possible explanations for this component: (1) the near and far sides of the outflow cavity walls; (2) a precessing outflow; and (3) an outflow that winds in space due to the orbital motion of its driving source.

4.3.1. Near and Far Sides of Outflow Cavity Walls

Here, we consider the possibility that the S-shaped component is part of the same outflow cavity traced by the X-shaped component. In the model described in Section 4.1, the outflow cavity has a half-opening angle ($\sim 45^\circ$) that is larger than its inclination to the plane of the sky ($\sim 30^\circ$). On the NE side of the outflow cavity, where the observed limb-brightened walls are redshifted, the walls on the near side of this cavity are therefore blueshifted. Conversely, on the SW side of the outflow cavity, where the observed limb-brightened walls are blueshifted, the walls on the far side of this cavity are redshifted. The S-shaped component may therefore comprise the near side of the outflow cavity on the NE side and the far side of the outflow cavity on the SW side.

In such a case, the model described in Section 4.1 that fits the observed morphology and kinematics of the X-shaped component should also fit the observed morphology and kinematics of the S-shaped component. Figure 9 shows the PV diagram along the symmetry axis (position angle of 70°) of the X-shaped component. Emission close to the center straddled by the horizontal short-dashed lines is dominated by the compact central component. The solid line shows what our model described in Section 4.1 (with $C = 0.18 \text{ km s}^{-1} \text{ arcsec}^{-1}$ and $i = 30^\circ$) predicts if the S-shaped component comprises the near side of the outflow cavity on the NE side and the far side of the outflow cavity on the SW side as described above. Clearly, the S-shaped component cannot be fit by such a model. The PV-diagram of the S-shaped component in Figure 9 is better fit by the long-dashed line, which corresponds to an acceleration constant for a Hubble-like radial expansion of $C = 0.75 \text{ km s}^{-1} \text{ arcsec}^{-1}$ for the same assumed inclination of $i = 30^\circ$. The long-dashed line in Figure 5 shows what this model predicts for the PV-diagram of the X-shaped component. Clearly, the X-shaped component cannot be fit by such a model.

To simultaneously fit the PV diagrams of both the X- and S-shaped components in a single model for the cone-shaped cavity, this cavity is required to have an inclination angle of $i = 16^\circ$ and acceleration constant for its Hubble-like radial expansion of $C = 0.36 \text{ km s}^{-1} \text{ arcsec}^{-1}$. With this set of parameters, the model fit to the X-shaped component is closely indicated by the solid line in Figure 5 and to the S-shaped component by the dashed line in Figure 9. The symmetry axis of such a cone-shaped cavity would then be tilted by $\sim 14^\circ$ from a direction orthogonal to the circumstellar disks of the main northern and southern protostellar components (Lim & Takakuwa 2006) as well as the surrounding envelope (Momose et al. 1998). This model does not provide an obvious explanation for why the far wall on the NE side and near wall on the SW side are not detected. More problematically, it does not provide a natural explanation for the S-shaped morphology of this component nor its oscillatory line-of-sight velocity as described next.

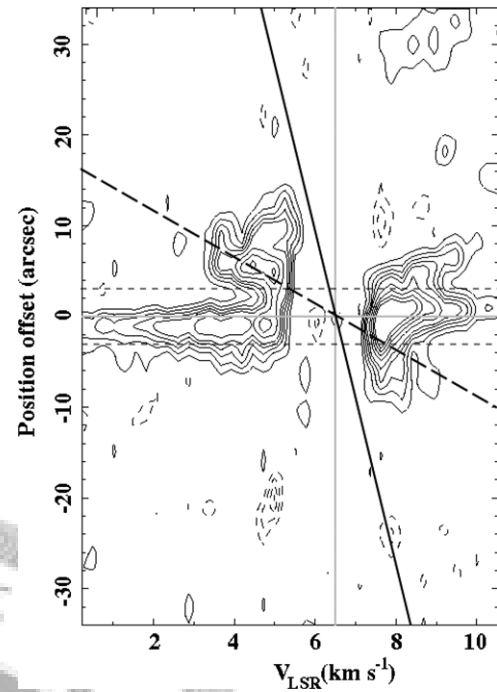


Figure 9. PV diagram of the CO(2-1) emission along the symmetry axis of the S-shaped component along a position angle of $= 70^\circ$. Contour levels and the different lines are the same as in Figure 5.

4.3.2. A Precessing Outflow

The morphology of the S-shaped component resembles a precessing outflow. To assess whether its kinematics also resemble a precessing outflow, we adopt the following simple model. We assume that the outflow is driven by a jet with a constant velocity v_{jet} that precesses at a constant angular frequency with a period T_p . Such a jet will describe a sinusoidal pattern in the sky with a deflection amplitude that increases with distance from the driving source in the form (adapted from Eisloffel et al. 1996):

$$\begin{pmatrix} x \\ y \end{pmatrix} = \begin{pmatrix} \cos\psi & -\sin\psi \\ \sin\psi & \cos\psi \end{pmatrix} \begin{pmatrix} \alpha \cdot l \cdot \sin(2\pi l/\lambda + \phi_0) \\ l \cdot \cos i \end{pmatrix}, \quad (2)$$

where x and y are the usual Cartesian coordinates, α is the precession amplitude, λ is the precession length scale, l is the distance from the source, ϕ_0 is the initial phase at the source, ψ is the position angle of the outflow symmetry (precession) axis in the plane of the sky, and i is the inclination angle of the outflow symmetry axis to the plane of the sky. The line-of-sight velocity, V_{LOS} , can be derived from

$$V_{\text{LOS}} = V_{\text{LSR}} \pm V_{\text{CO}} [\cos\theta \sin i + \sin\theta \cos i \cos(2\pi l/\lambda + \phi_0)], \quad (3)$$

where V_{CO} is the measured CO(2-1) velocity, and θ is the half-opening angle of the winding outflow. Figure 10 shows a schematic picture of this model in which the jet precesses clockwise about its symmetry (precession) axis. Note that smaller inclinations (i) require smaller precession amplitudes (α) to produce a given line-of-sight velocity (V_{LOS}) deflection in the sky.

We start by considering a straight jet. To fit the observed morphology and kinematics, we find that the inclination of the jet symmetry axis to the plane of the sky is restricted to

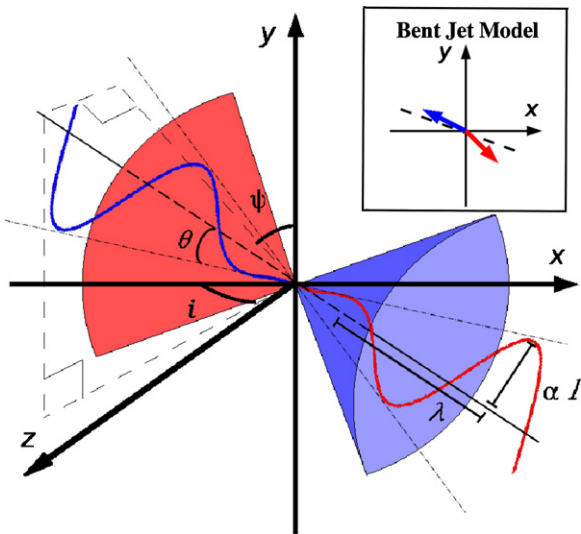


Figure 10. Schematic picture of a precessing jet, represented by the blue/red sinusoidal curve, that constitutes our model for the S-shaped component. The symmetry axis of the precessing jet is indicated by the thick dashed line, which forms an angle i to the plane of the sky and lies at a position angle ψ in the plane of the sky. The amplitude of the precessing jet, αl , increases with the distance l away from the driving source. The jet precesses on a cone with a half-opening angle of θ , which is represented by two dashed-dotted lines. The red and blue cones represent the outflow cavity traced by the X-shaped component (see Figure 8), which has the opposite velocity pattern to the S-shaped component. The blue/red arrows in the upper-right inset show the directions in which a bent jet emerges from its driving source in the model discussed in Section 4.3.2. The black dashed line is orthogonal to the circumstellar disk of the third protostellar component.

Table 4
Model Parameters for Precessing Jet

	ψ	α	θ	λ	ϕ_0 (red, blue)	i
Straight jet	57°	0.40	22°	40	$-90^\circ, -90^\circ$	30°
Bent jet	57°	0.18	10°	20	$110^\circ, -135^\circ$	30°

the range $15^\circ < i < 45^\circ$. For illustration, we take $i \simeq 30^\circ$, allowing us to directly compare the energetics of the S-shaped component with the X-shaped and compact central components (see Section 3.2.5). For this inclination, we find that the model parameters listed in Table 4 (the first row) provide the closest fit to both the observed morphology and kinematics of the S-shaped component. Within the allowed inclination range, other sets of model parameters can provide a more or less equally satisfactory fit to the observed morphology and kinematics.

Figure 11 compares the model predictions (the black line) in the case where $i \simeq 30^\circ$ with the observed morphology (upper panels) and line-of-sight velocity (the lower panel) of the S-shaped component. Here, the jet that drives the S-shaped component precesses at an angle of $\theta \approx 22^\circ$ to its symmetry (precession) axis. The morphology of the S-shaped component is well reproduced in this model where the driving jet lies outside the conical outflow cavity traced by the X-shaped component along most of its length, thus enabling it to entrain the surrounding material. The line-of-sight velocities plotted in Figure 11 (the lower panel) are derived by fitting the measured spectra at regularly spaced intervals along the predicted path of the precessing outflow with simple Gaussians. Two sets of error bars are plotted for each point, the smaller (the solid line) corresponding to the uncertainty in the measurement of the central velocity, and the larger (the dashed line) the FWHM

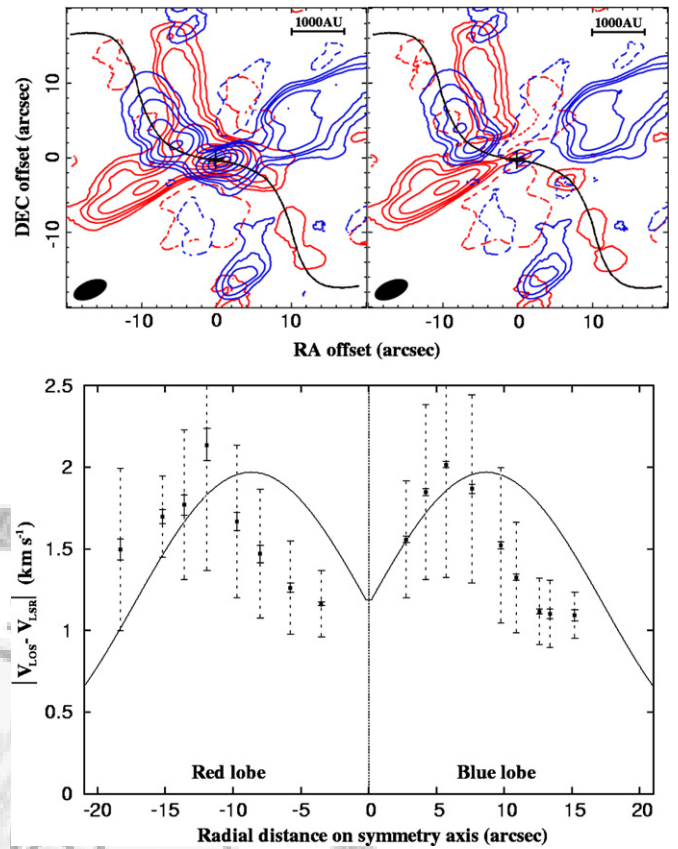


Figure 11. Predicted morphology (upper panels) and line-of-sight velocity along the path (the lower panel) of a precessing outflow, driven by a straight jet, with model parameters listed in the first row of Table 4. The black curves in the upper panels show the path of the jet superposed on the integrated CO(2–1) intensity map of Figure 4 with the central compact component included (the left panel) and with it subtracted out (the right panel). The black curves in the lower panels show the derived line-of-sight velocity of the outflow along the path of the jet superposed on the central CO(2–1) velocities derived from Gaussian fits to the spectra at regularly spaced intervals along this path (see text). The smaller solid error bars correspond to measurement uncertainties in the central velocities, while the large dashed error bars represent the FWHM of the fitted Gaussians.

of the fitted Gaussian. As can be seen, the line-of-sight velocity also changes more or less sinusoidally in reasonable—albeit not perfect—agreement with the model. Given that the entrained material may have had different initial velocities along the length of the outflow reflecting the rotation and contraction of the surrounding envelope, significant differences between the predicted and measured velocities may not be unexpected.

The precession period T_p can be determined from the wavelength λ and jet velocity v_{jet} such that

$$T_p \text{ (yr)} = 4.76 \times \frac{\lambda \times d(\text{pc})}{v_{\text{jet}}(\text{km s}^{-1})}, \quad (4)$$

where d is the distance to L1551 IRS5 (140 pc). Assuming a typical jet velocity of $\sim 50\text{--}150 \text{ km s}^{-1}$ (see below for reason why these values were adopted), the precession period is $\sim 130\text{--}400 \text{ yr}$.

To see if we can produce an even better fit to the observed morphology and, especially, kinematics, of the S-shaped component, we relax the requirement that the jet driving this component be straight. A bent jet (see inset in Figure 10)—in which the two opposing arms are not aligned—have been seen or invoked to explain the bipolar molecular outflows from a number of protostellar systems. The mechanisms that can lead to such

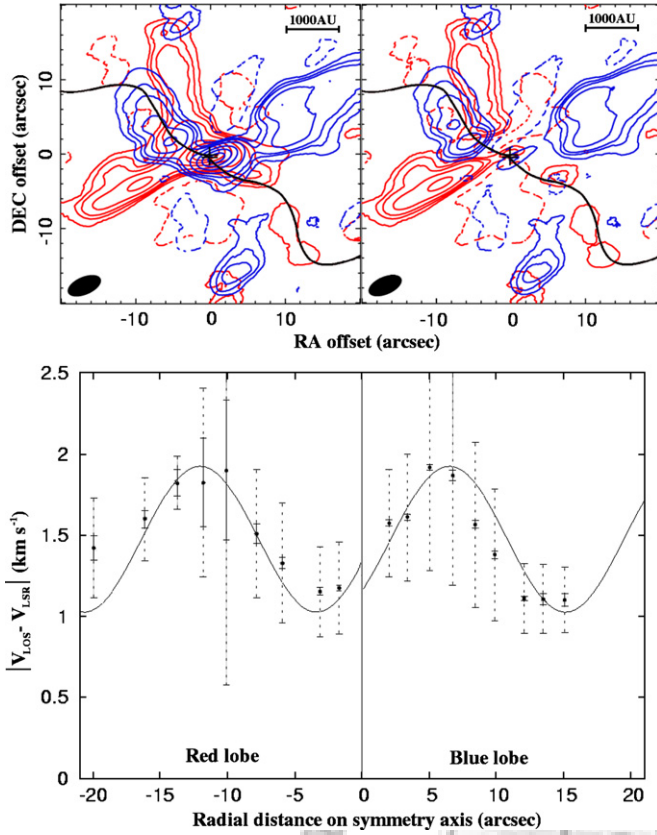


Figure 12. Same as for Figure 11, but in this case for a precessing outflow driven by a bent jet with the model parameters listed in the second row of Table 4. This model better reproduces the observed line-of-sight velocities as shown in the lower panel.

bending have been explored by Fendt & Zinnecker (1998); in the present situation, wide-angle winds at the base of the main northern and/or southern protostellar components pushing on the jet of the third protostellar component provide yet another possibility. Adopting once again $i \simeq 30^\circ$, we find that the model parameters listed in Table 4 (the second row) provide a better fit to the observed kinematics. Figure 12 plots the model predictions (the black line) for the observed morphology (upper panels) and line-of-sight velocity (the lower panel) of the S-shaped component, where the jet that drives this component precesses at an angle of $\sim 10^\circ$ to its symmetry axis. As can be seen, the measured line-of-sight velocities along the precessing outflow are in relatively good agreement with model predictions for a bent jet where one arm lies at an angle of 163° to the other (for a straight jet, the two arms lie at an angle of 180°). For a jet velocity of $\sim 100 \text{ km s}^{-1}$ as assumed above, the precession period corresponds to $\sim 135 \text{ yr}$.

Could the S-shaped component, which as we have shown can be well fitted by a precessing outflow, be driven by the candidate third protostellar component in L1551 IRS55 discovered by Lim & Takakuwa (2006)? The circumstellar disk of this third component is tilted with respect to the closely aligned circumstellar disks of the two main protostellar components as well as their surrounding pseudodisk. The outflow driven by a jet from the third protostellar component should therefore have a different inclination and/or position angle in the sky compared with the outflows driven by the northern and southern protostellar components. Indeed, the S-shaped outflow is tilted in the opposite sense of the sky

with respect to the compact central outflow, X-shaped outflow cavity, and large-scale bipolar molecular outflow, all of which are driven by the two main protostellar components. In the model incorporating a straight jet, the jet currently emerges at its origin at a position angle of 78° in the plane of the sky. By comparison, the major axis of the circumstellar disk of the third component is at a position angle of $118^\circ \pm 8^\circ$, and hence the jet is bent by $\sim 50^\circ$ from orthogonal to the disk. In the model incorporating a bent jet, at or close to its origin the eastern (blueshifted) arm of the jet emerges at a position angle of $\sim 65^\circ$ and the western (redshifted) arm of the jet at a position angle of $\sim 48^\circ$ as sketched in the inset of Figure 10, within $\sim 20^\circ$ and $\sim 37^\circ$ respectively from orthogonal to the disk.

Tidal interactions between the third protostellar component and its more massive neighbor(s) could cause the disk of this component to precess, resulting in the precessing outflow seen. Bate et al. (2000) have shown that such interactions between two protostellar components in a binary system should cause their circumstellar disks to precess at a frequency that is a small fraction (of order a few percent) of their orbital angular frequency. Taking a mass for the main northern protostellar component of $0.45 M_\odot$ and the third protostellar component of $0.1 M_\odot$, and a physical separation between the two components equal to their projected separation of $\sim 13 \text{ AU}$ (see Lim & Takakuwa 2006), the orbital period of the third protostellar component about the northern protostellar component is $\sim 63 \text{ yr}$. For a comparison, the estimated precession period of the S-shaped outflow is a few hundred years, assuming a jet velocity for the third protostellar component that is proportional to the square-root of its mass (i.e., proportional to the Keplerian velocity). The results are compatible with the idea that the circumstellar disk of the third protostellar component is precessing at an angular frequency much smaller than the orbital angular frequency of this component about the main northern protostellar component.

4.3.3. A Winding Outflow due to Orbital Motion

As mentioned by Fendt & Zinnecker (1998), the orbital motion of a protostar about its binary companion could also cause its originally straight jet to be deflected backward. Because such a bent jet possesses mirror rather than point symmetry (as in the case of a precessing jet), it should drive a winding outflow with reflection symmetry (e.g., Masciadri & Raga 2002). We have therefore examined whether the morphology and kinematics of the S-shaped component can be fit by a winding mirror-symmetric outflow.

For simplicity, we consider a circular orbit. To produce the observed morphology, the orbital velocity v_{orb} of the protostar that drives the jet is required to satisfy the relation

$$\frac{v_{\text{orb}} \cos j}{v_{\text{jet}} \cos i} = \tan \theta, \quad (5)$$

where as before v_{jet} is the jet velocity, i is the inclination to the plane of the sky at which the jet emerges from its driving source (i.e., tangent to the jet at its origin), θ is the half-opening angle of the winding outflow (also equal to the angle at which the jet is bent from its original trajectory), and j is the orbital inclination to the plane of the sky. The resulting line-of-sight velocity of such a jet will oscillate sinusoidally about the jet velocity, with the oscillation caused by the orbital motion of the protostar driving the jet. As can be seen from Figure 12, the molecular

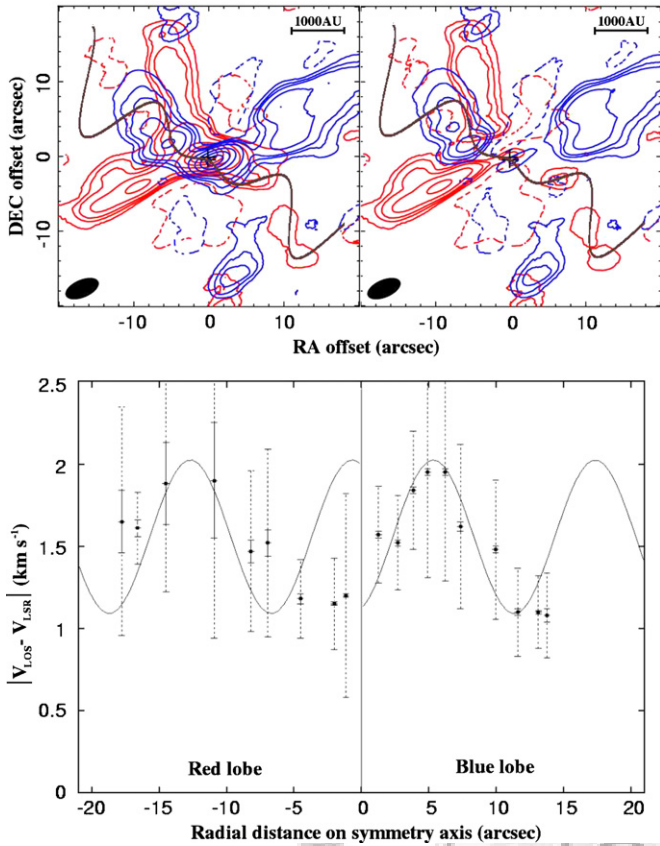


Figure 13. Same as for Figure 11, but in this case for an outflow driven by a mirror-symmetric jet with model parameters described in Section 4.3.3.

outflow oscillates with a half-amplitude of $\sim 0.5 \text{ km s}^{-1}$ about a line-of-sight velocity of $\sim 1.5 \text{ km s}^{-1}$; that is, ratio between these two values of ~ 0.3 . To produce the observed kinematics, the orbital velocity of the protostar is therefore also required to satisfy the relation

$$\frac{v_{\text{orb}} \sin j}{v_{\text{jet}} \sin i} \approx 0.3. \quad (6)$$

We assume throughout that the orbital diameter of the protostar is much smaller than the observable width of the winding outflow (i.e., the jet emerges from a stationary point), an assumption that we shall return to later.

We found that a mirror-symmetric outflow model can provide a reasonable fit to the observed morphology and kinematics of the S-shaped component over only a relatively narrow range in values of $14^\circ \lesssim \theta \lesssim 19^\circ$ and $40^\circ \lesssim i \lesssim 50^\circ$. For illustration, we take median values of $\theta \approx 17^\circ$ and $i \approx 45^\circ$, in which case Equations (5) and (6) can be solved to give $j \approx 45^\circ$. To fit the observed morphology and kinematics, we also require $\lambda = 17''$. The model fit for these values is shown in Figure 13. It is superior, especially in reproducing the observed kinematics, to the model fit for a straight precessing jet, but inferior to that for a bent precessing jet.

The orbital period of the protostar is equal to the period of the winding outflow, which has the same dependence on the model parameters as the precession period given by Equation (4). Substituting into this equation $v_{\text{jet}} \approx v_{\text{orb}}/0.3$ from Equation (6), given the model parameters used here, we find $T_{\text{orb}}(\text{yr}) = 0.3 \times 4.76 \times \lambda \times d(\text{pc})/v_{\text{orb}}$. The product $v_{\text{orb}} \times T_{\text{orb}}$ is simply the circumference of the orbit, from which we derive an orbital diameter of $\sim 236 \text{ AU}$ ($\sim 1''.7$). Thus, the orbital diameter

is indeed much smaller than the observable width of the winding outflow, satisfying an underlying assumption of our model. In this model, the minimum projected orbital radius is $\sim 83 \text{ AU}$ ($\sim 0''.6$), many times larger than the observed projected separation of the third component from the main northern protostellar component of $\sim 13 \text{ AU}$ ($\sim 0''.1$). Indeed, the minimum projected orbital radius is a factor of ~ 2 larger than the observed projected separation of the third component from the main southern protostellar component. Thus, to fit all the observational constraints, elliptical orbits with high eccentricities would have to be considered (or a fourth yet unseen protostellar component invoked).

For the model parameters used here, the orbital period can also be expressed as

$$T_{\text{orb}}(\text{yr}) \approx \frac{1290(\text{yr})}{[M_N + M_{3rd}(M_\odot)]^{1/2}}, \quad (7)$$

where M_N and M_{3rd} are the masses of the main northern and third protostellar components, respectively. Taking $M_N \approx 0.45 M_\odot$ and $M_{3rd} \approx 0.1 M_\odot$ (Lim & Takakuwa 2006), we find $T_{\text{orb}} \approx 1700 \text{ yr}$ and hence $v_{\text{orb}} \approx 2.1 \text{ km s}^{-1}$ and $v_{\text{jet}} \approx 7 \text{ km s}^{-1}$. The jet velocity in this model is unreasonably small, a serious flaw in the picture where the winding outflow is due to the orbital motion of the driving source.

5. SUMMARY

L1551 IRS5 exhibits the first recognized bipolar molecular outflow from a protostellar system. Single-dish maps show that this outflow can be traced in both CO(1–0) and CO(2–1) to 1.4 pc on the sky along the NE (redshifted lobe) and SW (blueshifted lobe) sides of the system along a position angle of $\sim 50^\circ$. This outflow is presumably driven by the two main protostellar components in L1551 IRS5, each of which exhibits an ionized jet that is closely aligned with the major axis of the larger scale molecular outflow.

Here, we imaged the molecular outflow within $\sim 4000 \text{ AU}$ of L1551 IRS in CO(2–1) with the Submillimeter Array (SMA) at an angular resolution of $\sim 4''$ (linear resolution of $\sim 560 \text{ AU}$). Our observations revealed three distinct spatial-kinematic components:

1. An X-shaped structure centered on L1551 IRS with arms that can be traced to $\sim 20''\text{--}30''$ ($\sim 2800\text{--}4200 \text{ AU}$) from the system. It has a symmetry axis along the NE (redshifted side) to SW (blueshifted side) direction at a position angle of $\sim 70^\circ$. This component is therefore closely aligned with, and exhibits the same velocity pattern as, the large-scale bipolar molecular outflow.
2. A previously unknown S-shaped structure centered on L1551 IRS5 that can be traced to $\sim 15''$ ($\sim 2100 \text{ AU}$) from the system. It has a symmetry axis along the NE (blueshifted side) to SW (redshifted side) direction at a position angle of $\sim 55^\circ$. Although closely aligned with the major axis of the large-scale bipolar molecular outflow, this component also exhibits a velocity pattern in the opposite sense. There is no known counterpart to this outflow on large ($\gtrsim 0.1 \text{ pc}$) scales. This component has the smallest line width of all three components.
3. A previously unknown compact component centered on L1551 IRS5 that can be traced to $\sim 1''.4$ ($\sim 200 \text{ AU}$) from the system. It has a major axis along the NE (redshifted side) to SW (blueshifted side) direction at a position angle

of $\sim 65^\circ$. This component is therefore closely aligned with, and exhibits the same velocity pattern as, the large-scale bipolar molecular outflow. It has the largest line width of all three components.

We interpreted our results in the following manner:

1. The X-shaped component comprises the limb-brightened walls of a cone-shaped outflow cavity. The molecular gas originally in this cavity was likely entrained by the high-velocity collimated winds of the two main protostellar components, and subsequently excavated by the low-velocity wide-angle winds of the same components. The opening angle of this cavity is $\sim 90^\circ$, comparable to that seen in other Class I protostellar systems.
2. The S-shaped component is unlikely to be the front and back walls of the same outflow cavity whose limb-brightened walls are seen as the X-shaped component. Instead, the S-shaped component is most likely a precessing outflow whose symmetry axis is inclined in the opposite sense to the plane of the sky compared with the X-shaped and compact central components, as well as the large-scale bipolar molecular outflow. This precessing outflow may be driven by the candidate third protostellar component in L1551 IRS5 discovered by Lim & Takakuwa (2006), who found that the circumstellar disk of this component is misaligned relative to the two main protostellar components. Gravitational interactions between the third protostellar component and its likely more massive northern (and perhaps also southern) neighbor(s) may be causing the circumstellar disk and hence jet of this component to precess.
3. The compact central component likely comprises material newly entrained by one or both jets from the two main protostellar components. The relatively short dynamical age for this component of ~ 200 yr may suggest a recent enhancement in the strength of one or both ionized jets responsible for driving this outflow.

Previous single-dish observations suggest multiple ejection episodes in the large-scale bipolar molecular outflow of L1551 IRS5 (Bachiller et al. 1994). Our study reveals multiple bipolar molecular outflow components near the base of this large-scale outflow. It adds additional evidence for a third protostellar component in L1551 IRS5 that may be related to that discovered by Lim & Takakuwa (2006).

We thank Chin-Fei Lee for his advice in constructing the model for the X-shaped cavity, and N. Ohashi and M. Saito for fruitful discussions. We thank the anonymous referee for suggesting we consider whether an outflow that winds due to orbital motion can explain the S-shaped component, and the editor (E. Fiegelsen) for bringing to our attention the possibility that the X-ray source, seen at the base of the optical jets, could be related to the compact central concentration. J.L. and S.T. acknowledge grants from the National Science Council of Taiwan (NSC 96-2112-M-001-020-MY2 and NSC 97-2112-M-001-003-MY2 respectively) in support of this work. The grant to J.L. also provides a Masters student stipend for P.-F.W.

Facilities: SMA.

REFERENCES

- André, P., Motte, F., & Bacmann, A. 1999, *ApJ*, **513**, 57
- Arce, H. G., & Sargent, A. I. 2004, *ApJ*, **612**, 342
- Arce, H. G., & Sargent, A. I. 2005, *ApJ*, **624**, 232
- Arce, H. G., & Sargent, A. I. 2006, *ApJ*, **646**, 1070
- Bachillar, R., Pérez Gutiérrez, M., Kumar, M. S., & Tafalla, M. 2001, *A&A*, **372**, 899
- Bachillar, R., Tafalla, M., & Cernicharo, J. 1994, *ApJ*, **425**, 93
- Bally, J., Feigelson, E., & Reipurth, B. 2003, *ApJ*, **584**, 843
- Barsony, M., Scoville, N. Z., & Chandler, C. J. 1993, *ApJ*, **409**, 275
- Bate, M. R., bonnell, I. A., Clarke, C. J., Lubow, S. H., Ogilvie, G. I., Pringle, J. E., & Tout, C. A. 2000, *MNRAS*, **317**, 733
- Beckwith, S. V. W., & Sargent, A. I. 1991, *ApJ*, **381**, 250
- Bieging, J. H., & Cohen, M. 1985, *ApJ*, **292**, 249
- Bourke, T. L., et al. 1997, *ApJ*, **476**, 781
- Duquennoy, A., & Mayor, M. 1991, *A&A*, **248**, 485
- Eisloffel, J., Smith, M. D., Davis, C. J., & Ray, T. P. 1996, *AJ*, **112**, 2086
- Fendt, C., & Zinnecker, H. 1998, *A&A*, **334**, 750
- Fridlund, C. V. M., Bergman, P., White, G. J., Pilbratt, G. L., & Tauber, J. A. 2002, *A&A*, **382**, 573
- Fridlund, C. V. M., & Liseau, R. 1998, *ApJ*, **499**, 75
- Fridlund, C. V. M., Sandqvist, A., Nordh, H. L., & Olofsson, G. 1989, *A&A*, **213**, 310
- Gueth, F., & Guilloteau, S. 1999, *A&A*, **343**, 571
- Ho, P. T. P., Moran, J. M., & Lo, K. Y. 2004, *ApJ*, **616**, 1
- Hodapp, K. 1994, *ApJS*, **94**, 615
- Keene, J., & Masson, C. R. 1990, *ApJ*, **355**, 635
- Lim, J., & Takakuwa, S. 2006, *ApJ*, **653**, 425
- Looney, L. W., Mundy, L. G., & Welch, W. J. 1997, *ApJ*, **484**, 157
- Masciadri, E., & Raga, A. C. 2002, *ApJ*, **568**, 733
- Mathieu, R. D. 1994, *ARA&A*, **32**, 465
- Momose, M., Ohashi, N., Kawabe, R., Nakano, T., & Hayashi, M. 1998, *ApJ*, **504**, 314
- Moriarty-Schieven, G. H., Johnstone, D., Bally, J., & Jenness, T. 2006, *ApJ*, **645**, 357
- Moriarty-Schieven, G. H., & Snell, R. L. 1988, *ApJ*, **332**, 364
- Moriarty-Schieven, G. H., Snell, R. L., Strom, S. E., Schloerb, F. P., Strom, K. M., & Grasdalen, G. L. 1987, *ApJ*, **371**, 95
- Moriarty-Schieven, G. H., Wannier, P. G., Keene, J., & Tamura, M. 1994, *ApJ*, **436**, 800
- Ohashi, N., Hayashi, M., Ho, P. T. P., Momose, M., & Hirano, N. 1996, *ApJ*, **466**, 957
- Ohashi, N., Kawabe, R., Ishiguro, M., & Hayashi, M. 1991, *AJ*, **102**, 2054
- Pyo, T., Hayashi, M., Kobayashi, N., Terada, H., Goto, M., & Yamashita, T. 2002, *ApJ*, **570**, 724
- Pyo, T., et al. 2005, *ApJ*, **618**, 817
- Rodríguez, L. F., et al. 1998, *Nature*, **395**, 355
- Rodríguez, L. F., Curiel, S., Cantó, J., Loinard, L., Raga, A. C., & Torrelles, J. M. 2003a, *ApJ*, **421**, 330
- Rodríguez, L. F., Porras, A., Claussen, M. J., Curiel, S., Wilner, D. J., & Ho, P. T. P. 2003b, *ApJ*, **586**, L137
- Saito, M., Kawabe, R., Kitamura, Y., & Sunada, K. 1996, *ApJ*, **473**, 464
- Sault, R. J., Teuben, P. J., & Wright, M. C. H. 1995, *ASPC*, **77**, 433
- Scoville, N. Z., Carlstrom, J. E., Chandler, C. J., Phillips, J. A., Scott, S. L., Tilanus, R. P. J., & Wang, Z. 1993, *PASP*, **105**, 1482
- Snell, R. L., Loren, R. B., & Plambeck, R. L. 1980, *ApJ*, **239**, 844
- Stahler, S. W. 1994, *ApJ*, **422**, 616
- Stojimirović, I., Narayanan, G., Snell, R. L., & Bally, J. 2006, *ApJ*, **649**, 280
- Strom, K. M., Strom, S. E., & Vrba, F. J. 1976, *AJ*, **81**, 320
- Tafalla, M., Myers, P. C., Mardones, D., & Bachiller, R. 2000, *A&A*, **359**, 967
- Takakuwa, S., et al. 2004, *ApJ*, **616**, 15
- Tohline, J. E. 2002, *ARA&A*, **40**, 349
- Uchida, Y., Kaifu, N., Shibata, K., Hayashi, S. S., Hasegawa, T., & Hmataka, H. 1987, *PASJ*, **39**, 907
- Velusamy, T., & Langer, W. D. 1998, *Nature*, **392**, 685
- Wilner, D. J., & Welch, W. J. 1994, *ApJ*, **427**, 898

3.3 Mechanism of Jet Bending

As mentioned in Wu et al. (2009), in order to better reproduce the observed line-of-sight velocity of the S-shaped component, we relaxed the requirement that the jet should be straight, that is, the two arms lie at an angle of 180° . A bent jet has been seen in bipolar molecular outflows from several protostellar systems. Possible bending mechanisms have been explored by Fendt & Zinnecker (1998). In L1551 IRS5 system, the likely mechanism is the dynamical pressure of the wide angle wind from the northern component. A schematic figure of a bending jet is presented in Figure 3.1. The high speed winds could exert enough force that push the jet to bend. Here we consider the wind velocity v_{wind} and wind density n_{wind} , then the pressure exerted by the wind $P_w = n_{wind}v_{wind}^2$. A particle moving outwards gains the momentum in the wind direction, that is, it has a velocity component in the wind direction. The bending angle then is $\tan\alpha = v_{\perp}/v_{jet}$, where v_{\perp} is the velocity component in the wind direction. Assuming the wind blows perpendicular to the jet with a diameter D_{jet} , the force exerting on a small volume is $n_{wind}v_{wind}^2/D_{jet}$. Considering a portion of the jet, which is away by a distance d from the disk plane. It takes a time $t = d/v_{jet}$ to travel through the distance. During the time, it acquires momentum $\Delta P_{\perp} = \frac{n_{wind}v_{wind}^2}{D_{jet}}t = \left(\frac{n_{wind}v_{wind}^2}{D_{jet}}\right)\left(\frac{d}{v_{jet}}\right)$, thus the velocity $v_{\perp} = \Delta P_{\perp}/n_{jet}$, where n_{jet} is the density of the jet. Here we obtained

$$\tan(\alpha) = \frac{d}{D_{jet}} \frac{n_{wind}}{n_{jet}} \left(\frac{v_{wind}}{v_{jet}}\right)^2 = \left(\frac{d/D_{jet}}{10}\right) \left(\frac{n_{wind}/n_{jet}}{0.1}\right) \left(\frac{v_{wind}/v_{jet}}{1}\right)^2. \quad (3.1)$$

We assumed $n_{wind}/n_{jet} \simeq 0.1$, and a same jet velocity of 100 km s^{-1} as we used in precession outflow model, a wind velocity of 100 km s^{-1} as reported by Pyo et al. (2005), then the bending angle depends only on the distance d :

$$\tan(\alpha) = 0.1\left(\frac{d}{D_{jet}}\right) \quad (3.2)$$

In our precession outflow scenario, the best-fit bent jet model requires a bending angle of 5° near the outflow launching point. This bending angle can be achieved at a distance $d \sim D_{jet}$.



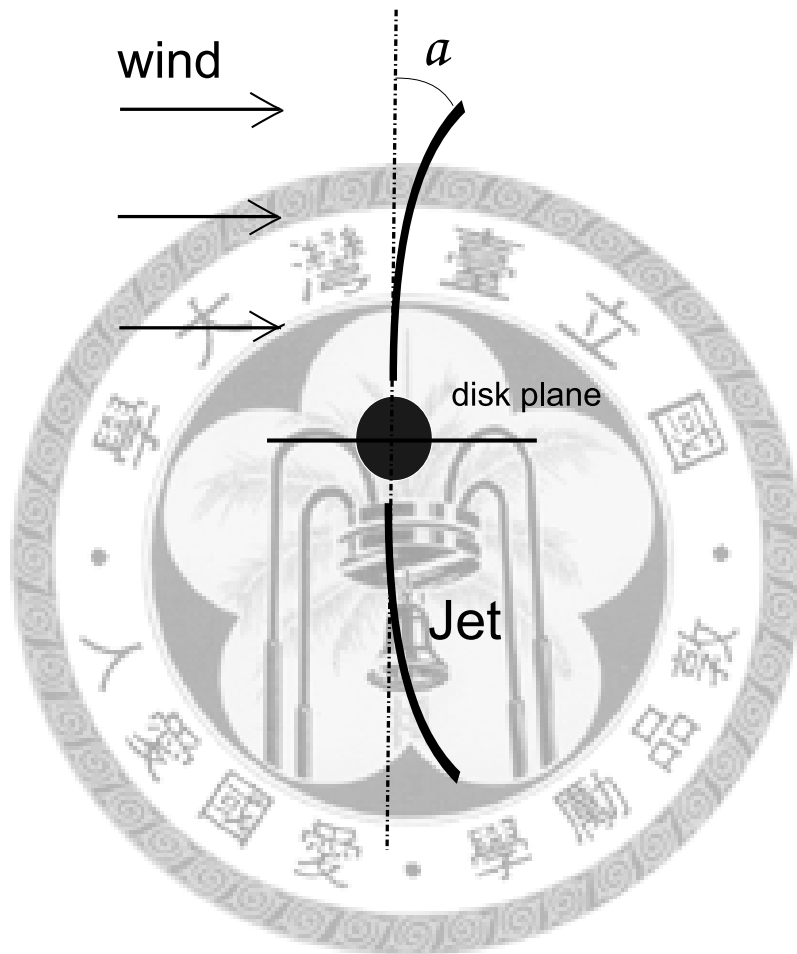


Figure 3.1: A schematic figure for a jet bend by the wind. The bent jet is represented by solid curves. The protostar and disk are plotted as the black circle and horizontal solid line.

Chapter 4

Bipolar Molecular Outflow from the L1551 NE Protostellar System

4.1 Introduction

Bipolar outflow or jet is regarded as an essential phenomenon to carry away the excess angular momentum of the inner region of the circumstellar disk in the star-forming process. Molecular outflows, often seen in CO, consist of molecular gas entrained or pushed away by the jet. In the case of the L1551 NE protostellar system, it is difficult to probe its molecular outflow, because the outflow from L1551 IRS5 passed through the L1551 NE region and affected its physical properties (Yokogawa et al., 2003). Moriarty-Schieven et al. (1995) reported their JCMT CO(3–2) line observation toward the L1551 NE protostellar system. The image shows the blueshifted emission westward to L1551 NE and they claim it may correspond to the infrared reflection nebula, thus that is the molecular outflow from L1551 NE. But the

emission at redshifted velocities extends to both eastward and westward of L1551 NE (see Figure 2.8). Therefore, the bipolarity of the molecular outflow was not clear.

So far, no interferometric observation of study on the molecular outflow of the multiple system has been carried out. As already shown by Moriarty-Schieven et al. (1995), single-dish observation suffers from contamination by the L1551 IRS5 outflow. Higher angular resolution observations are required to separate the L1551 NE outflow from L1551 IRS5 outflow.

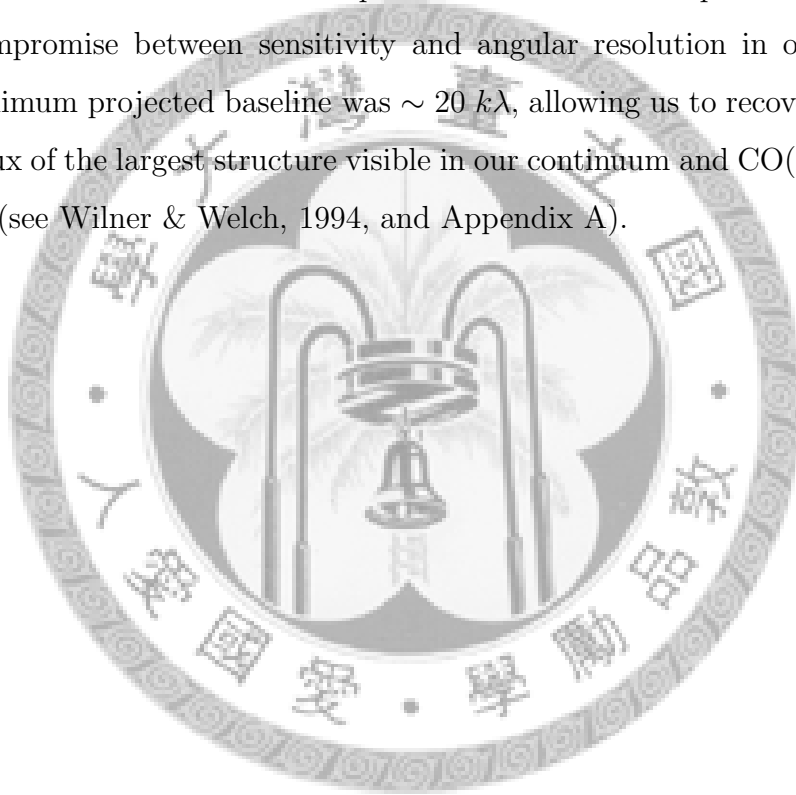
Here we report our 0.8 continuum and CO(3–2) observations. The CO(3–2) molecular line traces denser and warmer gas towards the vicinity of L1551 NE. With higher angular resolution, we show the bipolarity of the outflow lobes, which is the first unambiguous detection of a bipolar molecular outflow from L1551 NE.

4.2 Observations and Data Reduction

Observations of L1551 NE were carried out using the SMA on 2002 December 29 and 2005 January 8. On 2002 December 29, three SMA antennas worked at 345 GHz band in its compact configuration, provided three shorter baselines ranging from $18 k\lambda$ to $29 k\lambda$. The date of observation was before the official scientific commission of SMA, when only three antennas were available. On 2005 January 8, all eight antennas worked at the same 345 GHz band in the extended configuration, with the longest baseline of $\sim 250k\lambda$.

The calibration was done by Dr. Shigehisa Takakuwa. To make the CO(3–2) channel maps, we first subtracted the continuum emission from the visibility data as derived from a fit to the line-free channels. Because the emission is not very strong to be picked out automatically and properly

from dirty maps by the task CLEAN in MIRIAD, we applied clean boxes enclosing features that we believe to be real, as what we did for L1551 IRS5 data reduction. To ensure that there are no significant artificial features, we first checked the emission structures should change smoothly channel by channel. After that, we examined the residual map, and found no systemic pattern. Based on these two criterions, we believe we have properly extracted out the real features. A ROBUST parameter of 0.5 was adopted to have the best compromise between sensitivity and angular resolution in our maps. The minimum projected baseline was $\sim 20 k\lambda$, allowing us to recover $\sim 30\%$ of the flux of the largest structure visible in our continuum and CO(3–2) map of $\sim 5''$ (see Wilner & Welch, 1994, and Appendix A).






Table 4.1: Observational Parameters

PARAMETER	VALUE
Right Ascension (J2000)	04 ^h 31 ^m 44 ^s .47
Declination (J2000)	18° 08' 32".20
Primary beam (FWHM)	~36"
Synthesized beam (FWHM)	0".84 × 0".65 (P.A. = -47.9°)
Frequency (velocity) resolution	203 kHz (~ 0.175 km s ⁻¹)

4.3 0.8 mm Continuum Emission

Figure 4.1 shows our 0.8 mm continuum map of L1551 NE at an angular resolution of $0.''84 \times 0.''65$. The continuum emission peaks between the two VLA sources and is extended in the NW-SE direction. The NW-SE extended structure is similar to the 1.3 mm continuum image taken by Moriarty-Schieven et al. (2000), using OVRO millimeter-wave array, with an angular resolution of $1.''29 \times 1.''07$ (Figure 2.7b). But their image has an offset to the north relative to our image by $0.''5$, by comparing the peak position. Meanwhile, our peak position is in good agreement with the VLA sources.

We first modeled the continuum emission by an elliptical disk plus an elliptical Gaussian, the same as what Moriarty-Schieven et al. (2000) modeled for the 1.3 mm continuum image. They interpreted the elliptical disk represents a circumbinary disk and the elliptical gaussian is from the protostar.

Figure 4.2 shows the model image and the residual map (after subtracting the model image for our continuum map). A strong point-like source, coincident with the position of the southeastern protostar, remains in the residual map. Therefore, we fitted the continuum emission by two elliptical Gaussians at the location of the two mm-wave sources plus an elliptical disk and show the result in Figure 4.3. We came up with two point-like sources, whose positions correspond to the 3.6 cm VLA sources, NE-A and NE-B (Reipurth et al., 2002), with flux density of 0.36 Jy and 0.33 Jy, plus an elongated disk with flux density of 0.63 Jy and a size of $4.''3 \times 2.''6$ at a position angle of 150° , almost perpendicular to the [Fe II] jet (P. A. = 243° Reipurth et al., 2000) and the axis of HH 454 bipolar flow (P. A. = 242° Devine et al., 1999). We estimated the mass of each component using $M = F_\nu d^2 / B_\nu(T_d) \kappa_\nu$, assuming a distance of 140 pc, dust temperature of 42 K (Moriarty-Schieven et al., 1994) and the dust emissivities $\kappa_\nu = 0.1(\nu/10^{12})^\beta \text{cm}^2 \text{g}^{-1}$ (Beckwith &

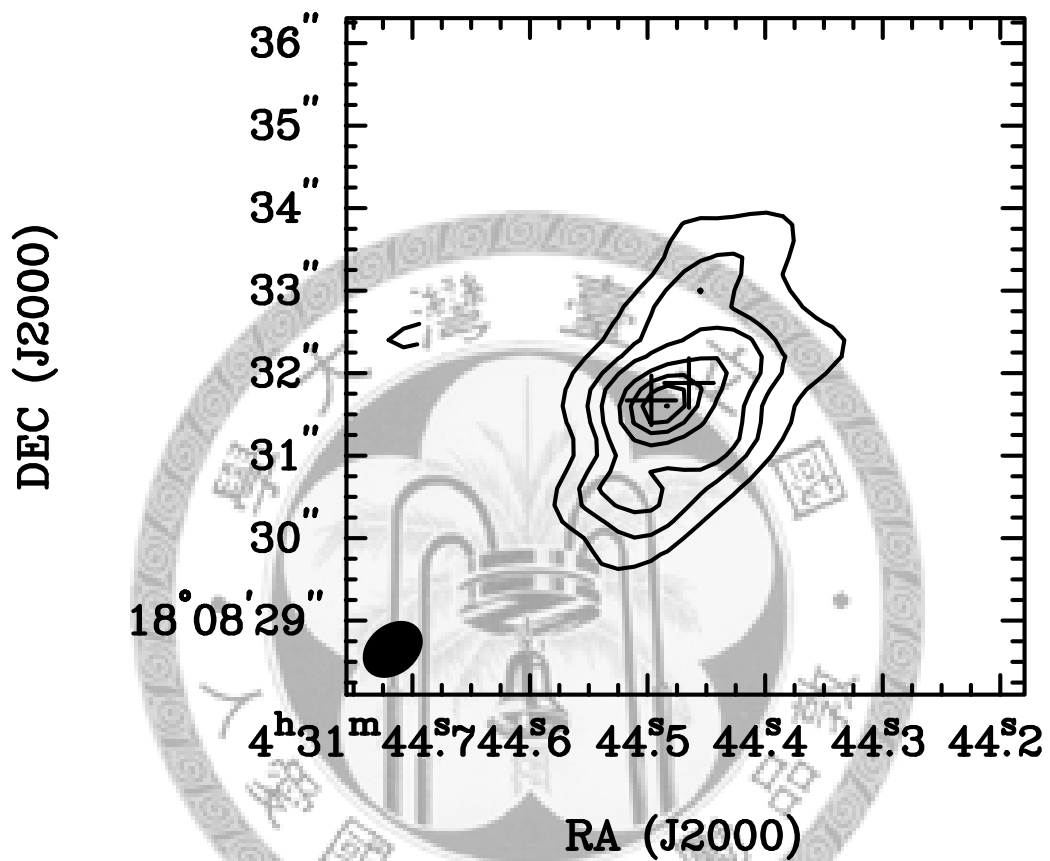


Figure 4.1: Continuum map of L1551 NE at 0.8 mm. Contour levels are plotted at $-2, 2, 6, 10, 20, 30, 40, 50\sigma$, where the rms uncertainty $\sigma = 0.0083 \text{ Jy beam}^1$. Crosses indicate the position of the 3.6 cm continuum emission peaks measured by Reipurth et al. (2002). The synthesized beam is shown as a filled ellipse at the bottom left corner.

Sargent, 1991), where β is derived as 1.3 from multi-wavelength measurements (Barsony & Chandler, 1993). The derived masses are 0.010 , $0.011 M_{\odot}$ for the two Gaussian sources, and $0.018 M_{\odot}$ for the disk. The total mass is $0.039 M_{\odot}$.



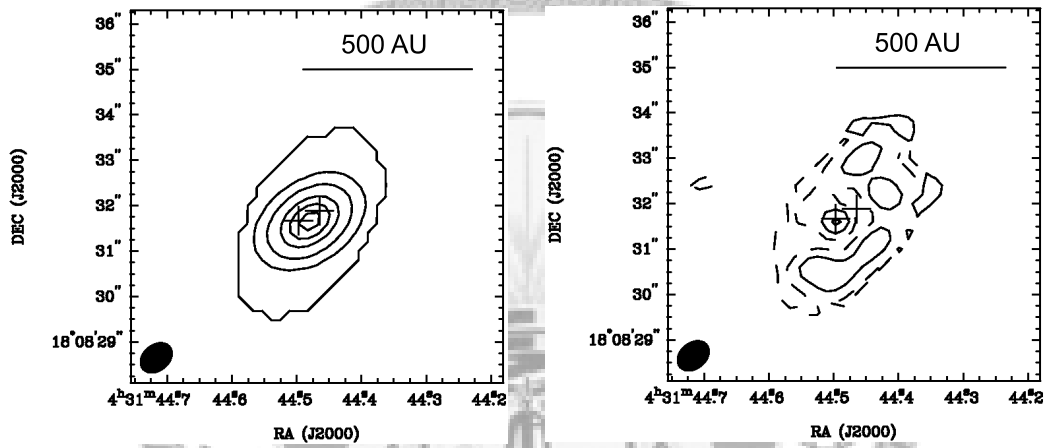


Figure 4.2: Model fitting to the 0.8 continuum image, using an elliptical disk plus an elliptical gaussian. We plotted the model in the left panel and the residual map in the right panel. Contour levels are the same as Figure 4.1. In the residual map, a point-like emission with a peak value of 6σ exists.

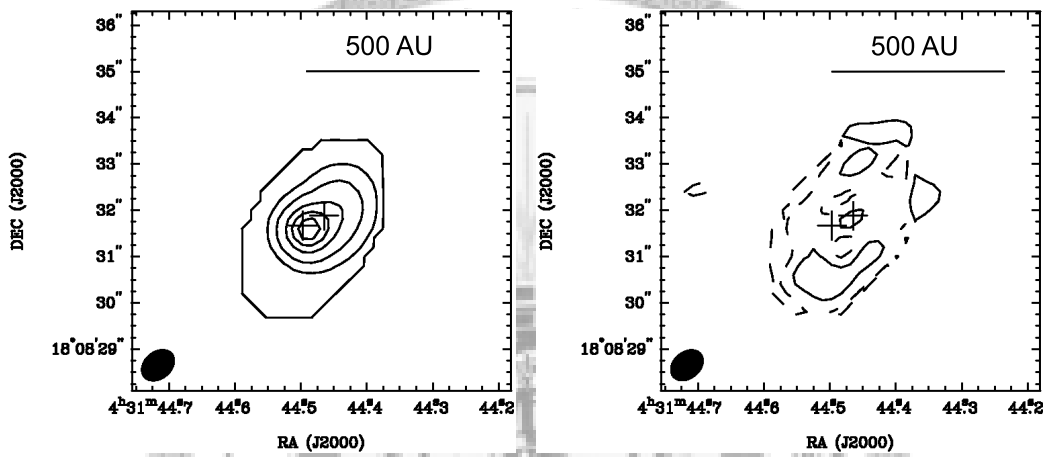


Figure 4.3: Model fitting to the 0.8 continuum image, using an elliptical disk plus two elliptical gaussians. We plotted the model in the left panel and the residual map in the right panel. Contour levels are the same as Figure 4.1.

4.4 CO(3–2) Line emission

Figure 4.4 shows our CO(3–2) channel maps of L1551 NE. Emission is detected over the velocity range 0.8–12.8 km s⁻¹ measured with respect to the local standard of rest. The absence of emission in channels with velocity 6.6–7.2 km s⁻¹ is likely due to the resolving out by interferometer of diffuse emission surrounding the protostar. Therefore we estimated a systemic velocity of ~ 6.9 km s⁻¹ for the L1551 NE protostellar system, comparable to previous estimate of 6.7 km s⁻¹, from the optically thin H¹³CO⁺ line emission (Saito et al., 2001).

Figure 4.5 shows the integrated CO(3–2) intensity map of blueshifted and redshifted emission, overlaid on the infrared image. The velocities spans 0.8–6.4 km s⁻¹ at blueshifted velocities (blue contours), 7.4–12.8 km s⁻¹ at redshifted velocities (red contours). The blue lobe is located to the southwest of L1551 NE, and has a spatial correspondence and a similar opening angle to the infrared reflection nebular. The red lobe is weaker and is located to the northeast of L1551 NE. This is the first unambiguous detection of a bipolar molecular outflow from L1551 NE.

Figure 4.6 shows the CO(3–2) spectrum summed over a region of diameter 14'' centered on L1551 NE. This permits us compare the spectrum directly with that taken by the JCMT. The SMA spectrum exhibits significant weaker emission at redshifted velocities than that at blueshifted velocities. On the other hand, the JCMT spectrum is stronger at redshifted velocities than blueshifted velocities. The two opposite asymmetry features in single-dish and interferometer spectra may indicate that there is more gas at redshifted velocities and much of it is in a smooth structure. The single-dish telescope detects all the emission from the redshifted materials, but the interferometric observation resolves a large portion of this emission. L1551 NE is

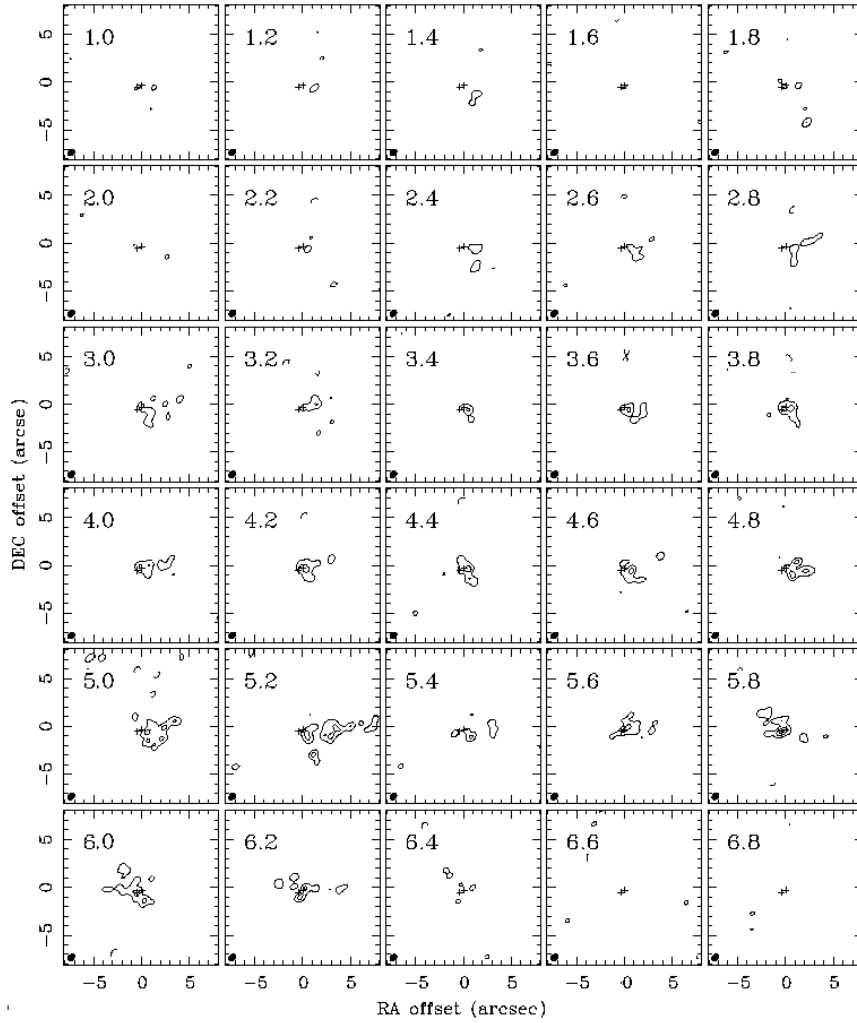


Figure 4.4: CO(3-2) channel maps of L1551 NE. Contours levels are plotted at $-2, 2, 4, 6, 8, 10$ and 12σ , where $\sigma = 0.058 \text{ Jy beam}^{-1}$. The central V_{LSR} of each channel is shown at the top left corner of each panel. Crosses indicate the positions to the two 3.6 cm source peaks as in Figure 4.1. The synthesized beam is shown by the filled ellipse at the bottom left corner.

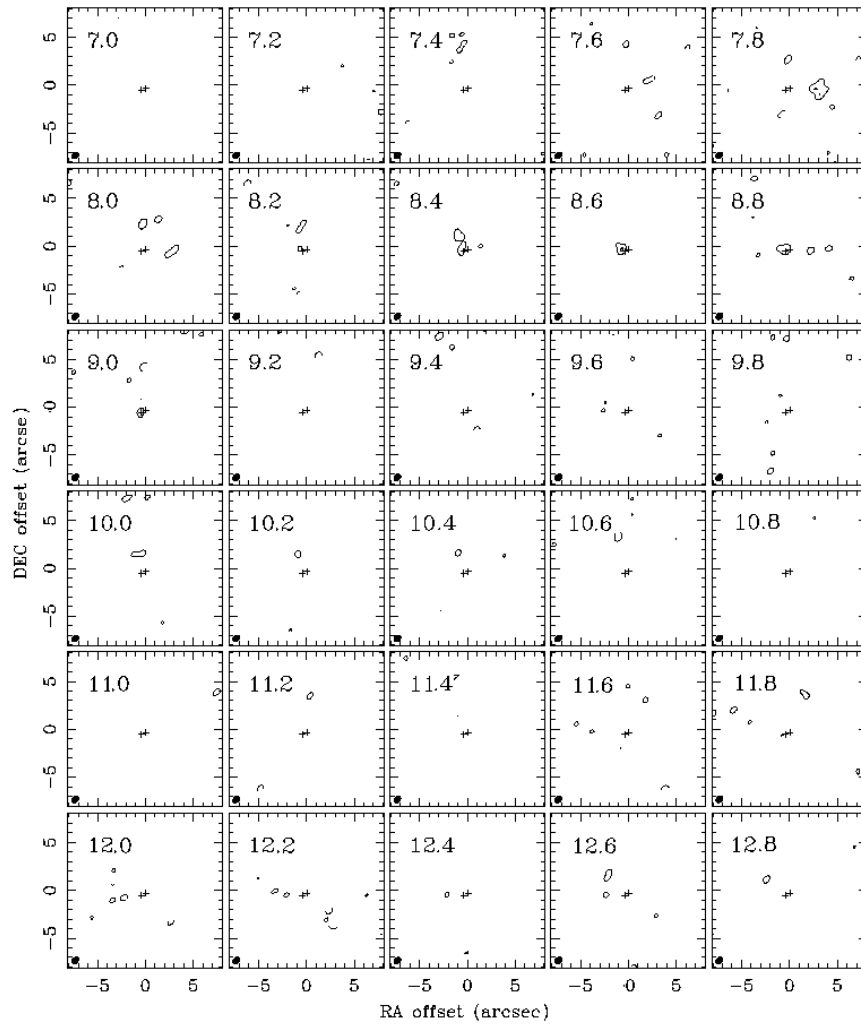


Figure 4.4: Continue.

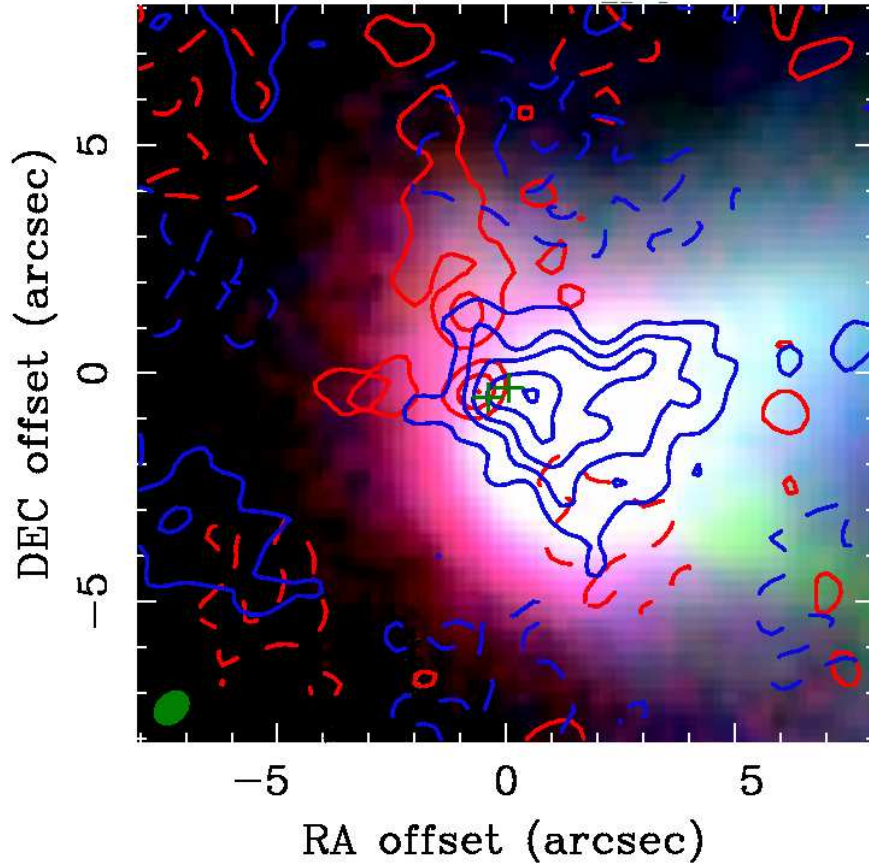


Figure 4.5: Integrated intensity map of CO(3-2) over $V_{\text{LSR}} = 0.8\text{--}6.4 \text{ km s}^{-1}$ (blue contours) and $V_{\text{LSR}} = 7.4\text{--}12.8 \text{ km s}^{-1}$ (red contours), stack on the Subaru 3-color image. Contour levels start at $\pm 2.0\sigma$ levels with intervals of 2.0σ . The negative levels are plotted as dashed contours. The rms uncertainty $\sigma = 0.6 \text{ Jy km s}^{-1} \text{ beam}^{-1}$. The synthesized beam is shown by the filled ellipse at the lower left corner. The colors are the same as Figure 2.6.

located 2.5 northeast from L1551 IRS5 and is immersed in the red lobe of L1551 IRS5 outflow, in particular with velocity at 8–12 km s⁻¹ (Stojimirović et al., 2006), where the SMA resolves out most of the extended structure.

We have estimated the physical parameters for the L1551 NE outflow after correcting our maps for the primary beam response of the SMA antennas and integrating over all signals detected higher than 2σ . For simplicity, we assume that the observed CO(3–2) emission is optically thin, in local thermal equilibrium (LTE), and assume an excitation temperature of 25K (Plambeck & Snell, 1995). Uncertainty in mass estimates is within a factor of 1.5 in the range of $T_{ex}=15\text{--}50$ K. In Tabel 4.2, we tabulate for the blue and red lobe its estimated mass M , outflow momentum $P = \sum_{\nu} M(\nu)\nu$, kinetic energy $E = \frac{1}{2}\sum_{\nu} M(\nu)\nu^2$, mass loss rate $\dot{M} = \sum_{\nu} M(\nu)/\tau(\nu)$. The dynamical age is the maximum dynamical time $\tau(\nu) = r/v$, where r is the longest distance from the driving source of outflowing gas at a given velocity v . We have corrected for the inclination angle, 60° to the line-of-sight, as suggested by Hayashi & Pyo (2008). The inclination angle is adopted base on the radial velocity measured from the [S II] line (Devine et al., 1999) and the tangential velocity measured from the proper motion of HH objects seen in [S II], [Fe II] and H-band peaks (Hayashi & Pyo, 2008).

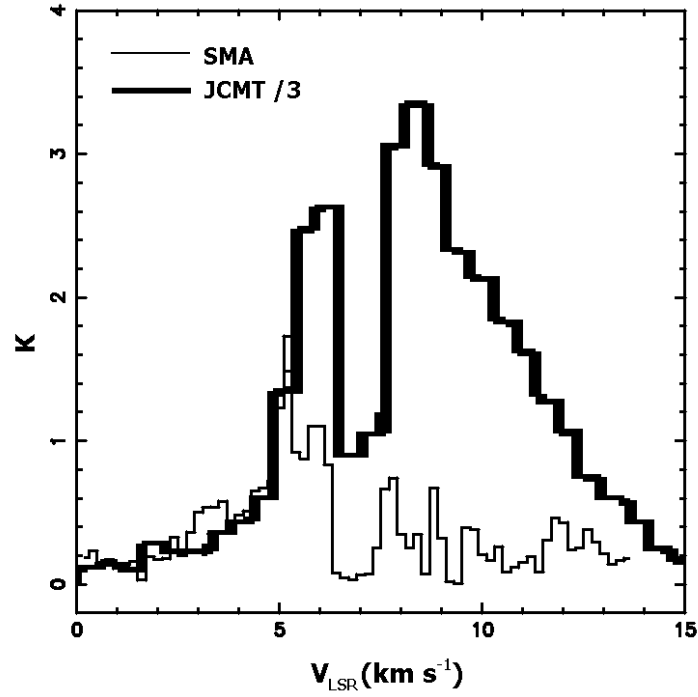


Figure 4.6: Spectra of the CO(3-2) line emission of L1551 NE, taken by JCMT (Moriarty-Schieven et al., 1995) and SMA (our observation). We divided the JCMT brightness temperature (thick line) by 3 for presentation purpose. We convolved the SMA spectrum (thin line) with a Gaussian with a FWHM of $14''$. The $14''$ FWHM is the angular resolution of JCMT at 345 GHz and allows us collect most of emission higher than 2σ level. The asymmetric JCMT spectrum suggested that the redshifted emission is likely contaminated by the IRS5 outflow. For the blueshifted emission with $V_{LSR} < 5 \text{ km s}^{-1}$, which is supposed to be free from IRS5 outflow contamination and comprises the outflowing gas, our SMA observation recovered about one third of the total flux.

Table 4.2: Properties of Outflow

Parameter	Red Lobe	Blue Lobe
Mass(M_{\odot})	3.68×10^{-5}	1.16×10^{-4}
Momentum($M_{\odot} \text{ km s}^{-1}$)	1.77×10^{-4}	5.59×10^{-4}
Kinetic energy(ergs)	1.25×10^{-40}	3.51×10^{-40}
Mass loss rate($M_{\odot} \text{ year}^{-1}$)	5.51×10^{-8}	2.55×10^{-7}
Dynamical age(years)	1600	1800

4.5 Discussion

4.5.1 Impact from IRS5 outflow

We imaged the bipolar molecular outflow of L1551 NE and derived its mass of $\sim 1.5 \times 10^{-4} M_{\odot}$. As mentioned in section 4.1, our SMA observation is sensitive to the small-scale ($< 5''$) outflow structures but recover only small fraction of smooth large-scale structures. To estimate how much flux is resolved out by the SMA, we compare the published CO(3–2) spectrum from JCMT (Moriarty-Schieven et al., 1995) with our data. We convolve our image with a $14''$ JCMT beam and took the spectrum centered on L1551 NE. In the blueshifted high-velocity regime, where most of the flux is supposed to be contributed by outflow and is not contaminated by the L1551 IRS5 outflow, we recovered $\sim 35\%$ of flux of blueshifted emission. After correcting for the missing flux, the outflow mass is $\sim 4.5 \times 10^{-4} M_{\odot}$. Comparing this number to the outflow mass of other Class 0 protostars obtained by interferometric CO observations (Arce & Sargent, 2006, OVRO millimeter array observation), we found that the L1551 NE outflow is about 2 orders of magnitude less massive than other protostars in the similar evolutionary stage. Even if we assume that the red lobe is equally massive as the blue lobe, the corrected outflow mass of L1551 NE becomes $\sim 7.0 \times 10^{-4} M_{\odot}$, and is still much smaller.

Yokogawa et al. (2003) demonstrated that the L1551 IRS5 outflow has collided with the L1551 NE envelope. Therefore, the reason for such a small mass is probably because the ambient gas around L1551 NE has been swept up by the L1551 IRS5 outflow. L1551 IRS5 is classified as a Class I protostellar system, older than L1551 NE, which is a Class 0 protostellar system. The projected distance of the two protostellar system is only $2.5'$ corresponds to a projected physical distance of 2×10^4 AU. If we take the projection effect

into account, assuming the L1551 NE is 45 degree to the line-of-sight as measured from L1551 IRS5, the physical distance is 3.4×10^4 AU. Considering a jet from L1551 IRS5 travels at a velocity of 100 km s^{-1} , it takes only 1.4×10^3 years to reach L1551 NE. It is likely that before the L1551 NE launched its outflow, the energetic outflow from L1551 IRS5 had passed through the L1551 NE region and pushed away much of ambient gas.

Figure 4.7 shows the dusty envelope mass versus bolometric luminosity of 45 protostellar systems (adopted from Bontemps et al., 1996). The dusty envelope mass is derived from single-dish 1.3 mm continuum observations, integrated over a region with $1'$ diameter. Open and filled circles are Class 0 and Class I sources, respectively. L1551 NE is classified as a class 0 protostar, based on its circumstellar envelope density profile, is plotted as a star. The dusty envelopes of Class 0 protostars are on average one order of magnitude more massive than those of Class I protostars. Comparing to other Class 0 protostars, the envelope mass is about one order of magnitude smaller than the average value of Class 0 protostars and more like Class I protostars. The smaller envelope mass also supports the idea that the ambient gas of L1551 NE has been swept up.

4.5.2 Different Age of the Binary Protostars

L1551 NE was detected at 3.6 cm by Rodríguez et al. (1995) and Reipurth et al. (2002), and it is a binary with a separation of $0''.5$ at a P.A. of 297° . Near-infrared images of L1551 NE show a bright reflection nebula toward southwest and an [Fe II] jet emanating from L1551 NE (Hodapp & Ladd, 1995; Reipurth et al., 2000; Hayashi & Pyo, 2008, see Figure 2.6). The jet axis does not pass through the center of the reflection nebula but is offset by $\sim 0.2''$. This feature has been proposed due to the binarity. The jet

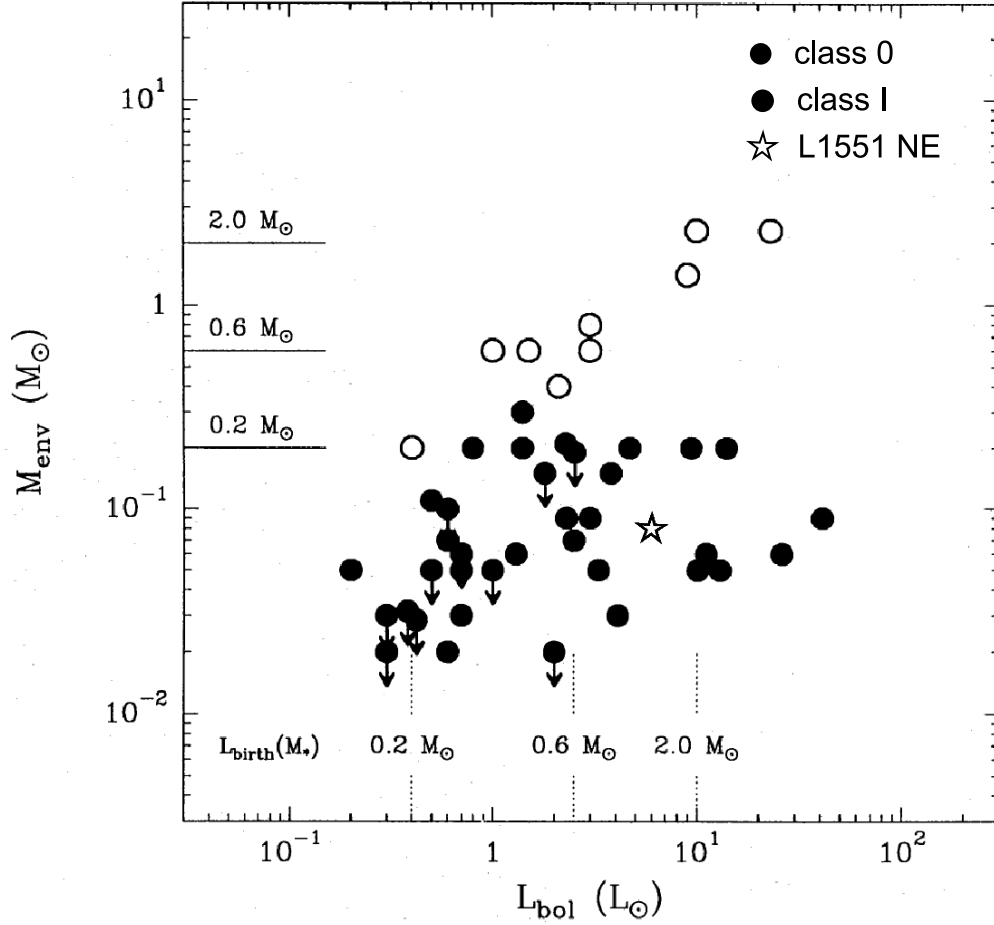


Figure 4.7: The difference between envelope masses of Class 0 and Class I sources. The Class 0 and Class I sources are represented by open and filled circles, respectively. L1551 NE is plotted as the star. In the original figure, Bontemps et al. (1996) derived envelope mass from the 1.3 continuum flux density integrated over a $1'$ diameter region. For L1551 NE, we took the data reported by Motte & André (2001), which also obtained 1.3 continuum flux density integrated over the region of the same angular size.

axis passes through southeastern component A, suggesting that component emanates the [Fe II] jet. And the brightest point of reflection nebula is likely resulted from northwestern component B (Reipurth et al., 2002). In Figure 4.4, a cavity-like structure can be seen at velocity $2.6\text{-}5.4 \text{ km s}^{-1}$, and its apex is closer to source B rather than to source A, suggesting this cavity-like structure is more close related to source B rather than source A. Thus we consider this structure is the counterpart of the near-infrared reflection nebulae and it provides a direct evidence that source B is the driving source and it also represents the evacuated cavity wall. On the other hand, no clear CO counterpart of the [Fe II] jet is found in our maps. The absence of the CO counterpart may suggest that the density of the gas entrained by the jet emanated from source A is too low to be detected. Meanwhile, we see the cavity-like structure, which is likely the counterpart of the reflection nebula launched by source B. It may due to the two protostars launched their outflows in different time. The outflow of source B launched first and evacuated a cavity around the protobinary. Then source A emanated a jet into a less denser region, smaller amount of gas was entrained by the younger jet and the density is below the detection limit.

Chapter 5

Future Work

5.1 L1551 IRS5

We have shown that there are three different outflow components in the vicinity of L1551 IRS5 protostellar system: (1) an X-shaped component comprises the limb-brightened walls of a cone-shaped cavity excavated by jets and/or wide-angle winds from the two main protostars. (2) a compact central component with $\sim 1''.4$ angular size located at the position of L1551 IRS5, likely comprising the newly entrained material. (3) an S-shaped component which is likely a precessing outflow driven by the candidate third protostar in L1551 IRS5 system.

Together with new discoveries, a number of questions were also raised in this observation:

1. The NW arm of the X-shaped component exhibits a more complex structure than the other three arms. The kinematics of the other three arms show a single Hubble-like flow, and all with a similar acceleration constant. As to the NW arm, it is composed of two spatially different components, as well as two Hubble-like flows with different

acceleration constants, neither corresponds to that of the other three arms. We proposed the complex spatial and kinematic structure is due to successive ejection episodes, as suggested by Bachillar et al. (1994). One thing remains unclear is that the signature of successive ejection episodes can be only seen in the NW arm but not in the other three arms.

2. We found the S-shaped component and showed that both morphology and kinematics are better fitted by a precessing outflow model rather than causing by the orbital motion of a binary system. However, our observation does not have an enough angular resolution to separate all three different outflow components in the central region of L1551 IRS5, thus the observation is not able to provide a tight constrain to the fitting in the central region.
3. As mentioned in the previous point, all the three outflow components mix together in the central region of L1551 IRS5. Our method to extract the compact central component (fitting Gaussians in each velocity channel) is unavoidable to extract also part of the X-shaped and S-shaped component, preventing us determining the physical parameters of the compact central component.

Our strategies and goals are described as follow:

1. For the X-shaped component, we would like to find the footprints of successive ejection episodes on all the arms of the X-shaped component. The NW arm is not only more complex but much brighter than the other three arms. It is possible that the higher flux density is not because the NW contains more CO molecules, but the structures are

smoother in other three arms and are resolved out by our interferometric observation. In this case, we need to image the CO molecular with shorter baselines, in order to recover more extended structure and its kinematics.

2. Our observation brings in ambiguity in determining the spatial distribution and the line-of-sight velocity of the S-shaped component close to the protostellar system, due to its insufficient angular resolution. Improving the measurement accuracy in the region close to the protostellar system helps us to determine whether this component exhibits a point symmetry as could be expected for precessing outflow, or a mirror symmetry as could be expected for the motion causing by orbital motion in a binary system. For this purpose, an observation with higher angular resolution is needed.
3. For the compact central component, we would like to determine the linear extend as well as the velocity structure, to see if this component also exhibits a Hubble-flow structure like the X-shaped component. To achieve this goal, we need higher angular resolution to resolve the compact central component, to obtain its kinematics. In addition, the compact central component is presumably a young outflow with smaller linear extend, a higher CO transition line may be a better tracer to probe it. The higher CO transition line may allow us collect mainly the denser and warmer gas and lower the contamination from the X-shaped component, which is supposed to be more diffused.

5.2 L1551 NE

We imaged the CO(3–2) line emission in the vicinity of L1551 NE, showed the bipolarity of the CO emission, confirmed that L1551 NE drives a CO molecular outflow. In our interferometric observation, the CO molecular outflow spans *sim* 5'' on both the NE (redshifted) and SW (blueshifted) sides of the system.

We found that the mass of outflowing gas of L1551 NE is much smaller than that of other Class 0 protostellar systems. We also checked the dust envelope mass in its surrounding 1' region and showed that the dust envelope mass of L1551 NE is also smaller than other Class 0 protostellar system. Yokogawa et al. (2003) suggested the outflow from L1551 IRS5 has a strong impact on the L1551 NE ambient region. We inferred from above observational results that the surrounding material in L1551 NE system has been swept up by the outflow from L1551 IRS5.

Our channel maps exhibit a cavity-like structure, whose apex is closer to the 3.6 cm VLA source B. The cavity-like structure is likely the counterpart of the infrared nebulae. For the collimated [Fe II] jet seen at infrared wavelength, we do not see its CO counterpart in our channel maps. The infrared nebulae and the collimated jet are suggested to be launched by VLA source B and A, respectively. Thus we inferred that the source B launched its outflow first and swept up the ambient gas. The jet from source A came out later, the density of ambient entrained material is too low to be detected.

To have deeper investigation of this system, the following considerations and observations should be taken:

1. As mentioned in section 4.2, we recovered only 30% of total flux of the largest structure (a Gaussian with FWHM of 5'') in the maps.

The single-dish CO(3–2) observation showed the blueshifted emission extends $\sim 20''$ to the southwest (Moriarty-Schieven et al., 1995) and our observation is not able to detect it. A set of interferometric observation with shorter baseline will help us to recover the larger-scale structure and have more complete picture of the kinematics of the molecular outflow.

2. We asserted that the evolutionary stages of the binary may be different, based on the molecular outflow. One way to test it directly is measuring the spectral index of the continuum spectra of each source at submillimeter wavelength, where is supposed to be dominated by synchrotron radiation from dust and reflects the property of dust grains. The grain size in more evolved system should be larger, result in a smaller spectral index. But this method requires a high-angular resolution to resolve the compact binary ($\sim 0''.5$ separation), which is cannot be easily achieved by current instruments.
3. Relative to the well-studied L1551 IRS5, only a few studies discussed about the envelope of L1551 NE. Yokogawa et al. (2003) reported CS and H^{13}CO^+ molecular line observations and revealed that both molecules are highly affected by the shock from L1551 IRS5 outflow. Thus those molecules do not reflect the spatial structure and kinematics of the envelope. L1551 NE and L1551 IRS5 are two multiple protostellar systems in different evolutionary stage, located in the same molecular cloud and separate only ~ 0.1 pc. The initial condition of these two protostellar system is likely similar. Extracting the physical properties of L1551 NE envelope, together with the well-studied L1551 IRS5 envelope would give us a picture of how the envelope evolves from the

observational point of view. For example, N_2H^+ is less affected by the shock and traces high density region could be a good tracer for studying the kinematics of the envelope of L1551 NE.



Bibliography

- Adams, F. C., Lada, C. J., Shu, F. H., 1987, *ApJ*, 312, 788
- André, P. 1995, *Ap&SS*, 224, 29
- André, P., Montmerle, T. 1994, *ApJ*, 420, 837
- André, P., Motte, F., Bacmann, A. 1999, *ApJ*, 513, 57
- André, P., Ward-Thompson, D., Barsony, B. 1993, *ApJ*, 406, 122
- Arce, H. G. & Sargent, A. I. 2004, *ApJ*, 612, 342
- Arce, H. G. & Sargent, A. I. 2005, *ApJ*, 624, 232
- Arce, H. G., Shepherd, D., Gueth, F., Lee, C.-F., Bachiller, R., Rosen, A., Beuther, H. 2005, *Protostars and Planets V*
- Arce, H. G., Sargent, A. I. 2006, *ApJ*, 646, 1070
- Bachillar, R., Pérez Gutiérrez, M., Kumar, M. S., Tafalla, M. 2001, *A&A*, 372, 899
- Bachiller, R., & Tafalla, M., In *The Origin of Stars and Planetary System* (C. J. Lada and N. D. Kylafis, eds.), pp. 227, Kluwer, Dordrecht.
- Bachillar, R., Tafalla, M., Cenicharto, J. 1994, *ApJ*, 425, 93

- Bally, J., Feigelson, E., Reipurth, B. 2003, ApJ, 584, 843
- Barsony, M. & Chandler, C. J. 1993, ApJ, 406, L71
- Bate, M. R., bonnell, I. A., Clarke, C. J., Lubow, S. H., Ogilvie, G. I., Pringle, J. E., Tout, C. A. 2000, MNRAS, 317 733
- Backwith, S. V. W. & Sargen, A. I. 1991, ApJ, 409, 275
- Beichman, C. A., Myers, P. C., Emerson, J. P., Harris, S., Mathieu, R., Benson, P. J., Jennings, R. E. 1986, ApJ, 307, 337
- Biegging, J. H., Cohen, M. 1985, ApJ, 292, 249
- Bontemps, S., André, P., Terebey, S., Cabrit, S. 1996, A&A, 311, 858
- Bourke, T. L., Garay, G., Lehtinen, K. K., Koehnkamp, I., Launhardt, R., Nyman, L., May, J., Robinson, G., Hyland, A. R. 1997, ApJ, 476, 781
- Briceño, C., Hartmann, L., Stauffer, J., Martín, E. 1998, AJ, 115, 2074
- Cohen, M., Harvey, P. M., Schwartz, R. D., Wilking, B. A. 1984, ApJ, 278, 671
- Cudworth, K. M., Herbig, G. H. 1979, AJ, 84, 548
- Devine, D., Reipurth, B., John, B. 1999, ApJ, 118, 972
- Draper, P. W., Warren-Smith, R. F., Scarrott, S. M. 1985, MNRAS, 216, 7P
- Eislfel, J., Smith, M. D., Christopher, J., Ray, T. P. 1996, AJ, 112, 2086
- Emerson, J. P., Harris, S., Jennings, R. E., Beichman, C. A., Baud, B., Beintema, D. A., Marsden, P. L., Wesselius, P. R. 1984, ApJ, 278, 49
- Fendt, C. & Zinnecker, H. 1998, A&A, 334, 750

- Fridlund, C. V. M., Liseau, R. 1998, ApJ, 499, 75
- Fridlund, C. V. M., Bergman, P., White, G. J., Pilbratt, G. L., Tauber, J. A. 2002, A&A, 382, 573
- Fridlund, C. V. M., Sandqvist, A., Nordh, H. L., Olofsson, G. 1989, A&A, 213, 310
- Gålfalk, M., Olofsson, G., Kaas, A. A., Olofsson, S., Bontemps, S., Nordh, L., Abergel, A., André, P., Boulanger, F., Burgdorf, M., Casali, M. M., Cesarsky, C. J., Davies, J., Falgarone, e., Montemerle, T., Perault, M., Persi, P., Prusti, T., Puget, J. L., Sibille, F. 2004, A&A, 420, 945
- Garnavich, P. M., Noriega-Crespo, A., Grenn, P. J. 1992, Rev. Mex. Astron. Astrofis., 24, 99
- Gueth, F. & Guilloteau, S. 1999, A&A, 343, 571
- Gueth, F., Guilloteau, S., Bachillar, R. 1996, A&A, 307, 891
- Gueth, F., Schilke, P., McCaughrean M. J. 2001, A&A, 375, 1018
- Hayashi, M., Pyo, T.-S. 2008, private communication
- Hodapp, K. 1994, ApJS, 94, 615
- Hodapp, K.-W. & Ladd, E. F. 1995, ApJ, 453, 715
- Kenyon, S. J., Dobrzycka, D., Hartmann, L. 1992, AJ, 104, 762
- Lee, C.-F., Mundy, L. G., Reipurth, B., Ostriker, E. C., Stone, J. M. ApJ, 542, 925
- Lee, C.-F., Mundy, L. G., Stone, J. M., Ostriker, E. C. 2002, ApJ, 576, 294

- Lim, J. & Takakuwa, S. 2006, ApJ, 653, 425
- Looney, L. W., Mundy, L. G., Welch, W. J. 1997, ApJ, 484, 157
- Lynds, B. T. 1962, ApJS, 7, 1
- Momose, M., Ohashi, N., Kawabe, R., Nakano, T., Hayashi, M. 1998, ApJ, 504, 314
- Moriarty-Schieven, G. H., Butner, H. M., Wannier, P. G. 1995, ApJ, 445, 55
- Moriarty-Schieven, G. H., Johnstone, D., Bally, J., Jenness, T. 2006, ApJ, 645, 357
- Moriarty-Schieven, G. H., Powers, J. A., Butner, H. M., Wannier, P. G., Keene, J. 2000, ApJ, 533, L143
- Moriarty-Schieven, G. H., Wannier, P. G., Keene, J., & Tamura, M. 1994, ApJ, 436, 800
- Moriarty-Schieven, G. H., Wannier, P. G. 1991, ApJ, 373, L23
- Motte, F. & André, P. 2001, A&A, 365, 440
- Mundt, R., Fried, J. W. 1983, ApJ, 274, 83
- Ohashi, N., Hayashi, M., Ho, P. T. P., Momose, M., Hirano, N. 1996, ApJ, 466, 957
- Plambeck, P. L. & Snell, R. L. 1995, ApJ, 446, 234
- Pound, M. W., & Bally, J. 1991, ApJ, 383, 705
- Pudritz, R. E., Norman, C. A. 1983, ApJ, 274, 677
- Pudritz, R. E., Norman, C. A. 1983, ApJ, 301, 571

- Pyo, T., Hayashi, M., Kobayashi, N., Terada, H., Goto, M., Yamashita, T. 2002, *ApJ*, 570, 724
- Pyo, T., Hayashi, M., Kobayashi, N., Tokunage, A. T., Terada, H., Tsujimoto, M., Hayashi, S. S., Usuda, T., Yamashita, T., Takami, H., Takato, N., Kendachi, K. 2005, *ApJ*, 618, 817
- Raga, A. & Cabrit, S. 1993, *A&A*, 278, 267
- Reipurth, B., Rodríguez, L. F., Anglada, G., Bally, J. 2002, *ApJ*, 124, 1045
- Reipurth, B., Yu, K. C., Heathcote, S., Bally, J., Rodríguez, L. F. 2000, *ApJ*, 120, 1449
- Rodríguez, L. F., Anglada, G., Rage, A. 1995, *ApJ*, 454, L149
- Rodríguez, L. F., D'Alessio, P., Wilner, D. J., Ho, P. T. P., Torrelles, J. M., Curiel, S., Gómez, Y., Lizano, S., Pedlar, A., Cantó, J., Raga, A. C. 1998, *Nature*, 395, 355
- Rodríguez, L. F., Curiel, S., Cantó, J., Loinard, L., Raga, A. C., Torrelles, J. M. 2003a, *ApJ*, 421, 330
- Rodríguez, L. F., Porras, A., Claussen, M. J., Curiel, S., Wilner, D. J., Ho, P. T. P. 2003b, *ApJ*, 586, L137
- Saito, M., Kawabe, R., Kitamura, Y., Sunada, K. 1996, *ApJ*, 473, 464
- Saito, M., Kawabe, R., Kitamura, Y., Sunada, K. 2001, *ApJ*, 547, 840
- Sault, R. J., Teuben, P. J., Wright, M. C. H. 1995, *ASPC*, 77, 433
- Schwartz, R. D. 1975, *ApJ*, 195, 631

- Scoville, N. Z., Carlstrom, J. E., Chandler, C. J., Phillips, J. A., Scott, S. L.,
Tilanus, R. P. J., Wang, Z. 1993, *PASP*, 105, 1482
- Shu, F. H., Adams, F. C., Lizano, S. 1987, *ARA&A*, 25, 23
- Shu, F. H., Lizano, S., Ruden, S., Najita, J. 1988, *ApJ*, 328, L19
- Shu, F. H., Najita, J., Ostriker, E. C., Shang, H. 1995, *ApJ*, 455, L155
- Shu, F. H., Najita, J., Ostriker, E. C., Wilkin, F., Ruden, S., Lizano, S. 1994,
ApJ, 429, 781
- Shu, F. H., Ruden, S. P., Lada, C. J., Lizano, S. 1991, *ApJ*, 370, L31
- Snell, R. L., Loren, R. B., Plambeck, R. L. 1980, *ApJ*, 239, 844
- Stojimirović, I., Narayanan, G., Snell, R. L., Bally, J. 2006, *ApJ*, 649, 280
- Strom, K. M., Storm, S. E., Vrba, F. J. 1976, 81, 320
- Tafalla, M., Myers, P. C., Mardones, D., Bachiller, R. 2000, *A&A*, 359, 967
- Takakuwa, S., Ohashi, N., Ho, P. T. P., Qi, C., Wilner, D. J., Zhang, Q.,
Bourke, T., Naomi, H., Choi, M., Yang, J. 2004, *ApJ*, 616, 15
- Velusamy, T. & Langer, W. D. 1998, *Nature*, 392, 685
- Wilner, D. J., Welch, W. J. 1994, *ApJ*, 427, 898
- Wu, P.-F., Takakuwa, S., Lim, J. 2009, *ApJ*, 698, 184
- Yokogawa, S., Kitamura, Y., Momose, M., Kawabe, R. 2003, *ApJ*, 595, 266
- Yen, H-W., Takakuwa, S., in prep

Appendix A

Missing Flux Resulted form the Visibility Coverage

The sampling theorem states that, if the intensity distribution is nonzero only within an interval of width l_w , it is fully specified by sampling the visibility function at points spaced $\Delta u = l_w^{-1}$ in u . In interferomic observations, the shortest baseline is always limited by the physical size of antennas. Therefore, on the uv -plane, a certain size of region around the center is unsampled, resulting a information loss of large scale structures, the total source flux is not measured.

We consider a source, with its amplitude described by a Gaussian, a peak amplitude T_0 at (x_1, y_1) , a FWHM θ ,

$$T(x, y) = T_0 \exp\left\{-\left(\frac{4 \ln 2}{\theta^2}\right)\left[(x - x_1)^2 + (y - y_1)^2\right]\right\}. \quad (\text{A.1})$$

The corresponding visibility function

$$V(u, v) = T_0 \left(\frac{\pi \theta^2}{4 \ln 2}\right)^{(1/2)} \exp\left[-\left(\frac{\pi^2 \theta^2}{4 \ln 2}\right)(u^2 + v^2)\right] \exp[-2\pi i(ux_1 + vy_1)]. \quad (\text{A.2})$$

Furthermore, we assume the uv plane is fully sampled from an inner radius $\beta_0 = S_{min}/\lambda$ to an outer radius $\beta_1 = S_{max}/\lambda$. The observed visibility function

becomes

$$\hat{V}(u, v) = V(u, v)B(u, v),$$

where

$$B(u, v) = \begin{cases} 0, & \beta < \beta_0, \\ 1, & \beta_0 < \beta < \beta_1, \\ 0, & \beta > \beta_1, \end{cases}$$

and

$$\beta = (u^2 + v^2)^{1/2}.$$

Here we assume the peak is located at $(0,0)$ for simplicity without loss of generality. Then the observed brightness distribution is given by

$$\hat{T}(x, y) = T(x, y) * b(x, y),$$

where $b(x, y)$ is the Fourier transform of $B(u, v)$ and the asterisk denotes the convolution. To quantify the missing flux due to the inner hole on the uv -plane, we defined R to be the ratio of the observed peak brightness to the peak brightness if there is no inner hole

$$R = \frac{\hat{T}(0, 0)}{\hat{T}(0, 0)|_{\beta_0=0}} = \frac{\int_{\beta_0}^{\beta_1} V(\beta)\beta d\beta}{\int_0^{\beta_1} V(\beta)\beta d\beta} = 1 - \frac{\int_0^{\beta_0} V(\beta)\beta d\beta}{\int_0^{\beta_1} V(\beta)\beta d\beta} \quad (\text{A.3})$$

Substituting for $V(\beta)$ and evaluating the integrals gives

$$R = 1 - \frac{1 - \exp[-(\pi^2\theta^2/4 \ln 2)\beta_0^2]}{1 - \exp[-(\pi^2\theta^2/4 \ln 2)\beta_1^2]} \quad (\text{A.4})$$

If β_1 is sufficiently large, that is, the longest baselines are long enough, the denominator $1 - \exp[-(\pi^2\theta^2/4 \ln 2)\beta_1^2] \simeq 1$, R reduces to a simple exponential form

$$R = \exp\left(-\frac{\pi^2\theta^2}{4 \ln 2}\beta_0^2\right). \quad (\text{A.5})$$

or

$$R = \exp\left[-1.88\left(\frac{\theta}{30''}\right)^2\left(\frac{S_{min}}{15 \text{ m}}\right)^2\left(\frac{\nu}{100 \text{ GHz}}\right)^2\right]. \quad (\text{A.6})$$

For our L1551 IRS5 observations in SMA compact configuration working at 230 GHz, the longest projected baseline is $\sim 65k\lambda = 85\text{m}$. The angular size of largest observed feature in channel maps $\sim 15''$. Given all these parameters, the denominator $1 - \exp[-(\pi^2\theta^2/4 \ln 2)\beta_1^2] = 1 - e^{-82} \simeq 1$, satisfying the approximation. As to the L1551 NE observations in combined SMA compact and extended configuration working at 345 GHz, the longest projected baseline is $\sim 250k\lambda = 220\text{m}$ and the largest observed angular size of features in channel maps is $\sim 5''$, therefore the denominator is $1 - e^{134} \simeq 1$. The approximation is valid in both observations.

